Università Degli Studi di Pisa

School of graduate studies "Galileo Galilei"

PhD Thesis

Modelistic approach to structure and dynamics of soft matter

Candidate
Antonella CIMOLI

Supervisor
Prof. Ivo CACELLI

Supervisor
Prof. Alessandro TANI

External advisor
Prof. Dr. Kurt KREMER

SSD CHIM/02

XXIII Cycle: Years 2008 - 2010

CONTENTS

INTRODUCTION

"Soft matter" includes a variety of materials ranging from liquid crystals to colloids, from polymers to foams, gels, granular materials, and to a number of biological materials, such as cell membranes, proteins, virus and DNA molecules [1, 2]. Soft matter systems are often referred to as "complex fluids" [3], and both terms give an idea of the most striking features of these classes of materials. Firstly, the constituting molecules are "soft" as they are easily deformed by thermal stresses or thermal fluctuations. Small changes in energies lead to great changes in structure: citing de Gennes, it can be said that soft matter has "large response functions" [3]. Its physical behavior, in fact, occurs at an energy scale comparable with the room temperature thermal energy (k_BT) [4], subsequently its dynamical and mechanical properties can undergo drastic changes because of relatively mild external fields. Secondly, weak van der Waals, hydrogen bonding or electrostatic intermolecular interactions are often sufficient to cause the constituent molecules to organize themselves into "complex", well-defined structures at the nanoscale [5].

Thermotropic liquid crystals are a typical example of molecules with this striking property to self-organization. The anisotropic steric repulsion and attractive forces, in fact, lead the molecules to align their principal symmetry axis along a common direction, in nematics, and, in smectics, to further organize themselves into layers. Furthermore, these phases can be reoriented by the application of modest electric and/or magnetic fields, which couple to the anisotropy in electrical permittivity or magnetic susceptibility arising from the oriented

molecules. Other examples of self-organizing materials are amphiphilic molecules forming micelles, polymers that give rise to a variety of microstructures depending on the composition and temperature, and phospholipid membranes making up bilayer structures.

A deep knowledge of these microscopic behaviors can lead to the comprehension and interpretation of experimental results, to an accurate description of structural and dynamical material properties, up to a prediction of some of the possible engineering, electro-optical, mechanical or biomedical applications. In fact, the design of materials possessing the desired physical, chemical and biological requirements can be aided significantly by the detailed investigation of structure and interactions at molecular scale [6].

Computer simulations represent, in this context, a fundamental resource to access atomistic insights into phase structure and processes [5]. Simulations can be used to address specific questions about the properties of a model system, often more easily than experiments on the actual system. Of course, experiments remain essential in validating the simulation methodology as a comparison of simulation and experimental data serve to test the accuracy of the calculated results and to provide criteria for improving the methodology. Thanks to the massive increase of computational resources, hardware and software [7, 8, 9, 10, 11], during the past three decades, this microscopic chemical approach has been useful in understanding the properties of many different materials, such as polymers [12, 13], liquid crystals [14, 15] and many biological systems [16, 17, 18, 19]. However, a full comprehension of the relationship between the molecular structure and the resulting macroscopic material properties is far from being reached. In particular, in liquid crystals field, the extreme sensitivity of the mesophases to the chemical background [20] makes the understanding of this link a challenge for the scientific community.

Furthermore, computational techniques allow us to access a full range of time and length scales, according to the process investigated in the molecular material and, consequently, to the requested level of molecular detail. In the case of a macromolecule, for example, different methods are used to study local vibrational motion of atoms and the diffusion of the center of mass, as these phenomena span more than ten orders of magnitude in time and space.
Quantum mechanical simulations allow electronic structure to be taken into account and are therefore essential for looking at processes involving reactions and/or electron transfer. This level of description, however, severely limits both length and time scales (a few hundreds of atoms for a few ps). Classical force fields, instead, allow for the study of much larger systems for longer timescales (thousand of atoms for tens of ns at atomistic detail). This

time window can be sufficient for the study of some phenomena, such as the diffusion of small molecules or the alignment of molecules in nematic liquid crystals. Micellisation and folding in macromolecules (as peptides), however, involve scales far beyond the atomistic ones and it would be unfeasible to run computer simulations of these systems with atomistically detailed models. More simplified models are employed, namely mesoscale or coarse-grained models which lump together groups of atoms into larger particles [21, 22, 4, 23, 24]. These models, even if with significantly simplified interactions, remain close to the chemical structure thus allowing for the step back and the reintroduction of chemical details (multiscale models).

In this context, the aim of this work is the study of the reliability of novel approaches for the modeling of soft matter systems, in particular of liquid crystals. After a brief introduction to these systems in Chapter 1, the validation of a protocol for force field parameterization is presented in Chapter 2. This protocol was developed by the Pisa group of Liquid Crystals in 2002 [25] and consists of the derivation of both inter and intramolecular contributions to the potential from quantum mechanical data. First, the energies of various dimer configurations and of some monomer conformations are computed at suitable levels of theory. Then, parametric model functions representing intra and intermolecular energies are fitted on these databases and parameters are derived. Finally, the force field is tested in molecular simulation runs and simulated and experimental properties are compared to assess the quality of the obtained force field. In Chapter 2 this approach is tested on a mesogenic molecule, namely 4,4'-diheptylazoxybenzene, making use of an united atom model, while in Chapter 3 the same validation is performed at a higher resolution with a fully atomistic approach. This investigation has allowed a deeper insight into the strong and weak points of the approach and has led to an improved strategy where the force field is derived from quantum mechanical energies of dimer configurations selected with the help of molecular simulations. The latest development of this improved strategy is presented in Chapter 4: a Fortran code, named PICKY, is being developed and its beta version has been tested on a simple molecule as a test case. Finally, Chapter 5 presents a further tool for investigations at atomistic level of details. It is a Fortran code, named POLDO, for exploring the energy minima of the potential energy surface of large and flexible van der Waals dimers.

CHAPTER

1

INTRODUCTION TO LIQUID CRYSTALS

Liquid crystals (LCs) are intermediate states between solid and liquid phases which exhibit a preferential alignment of molecules along a direction called director. This alignment makes some physical properties of such phases direction-dependent: this feature, together with the subsequent possibility of inducing orientational order through external stimuli, has made them focus of many investigations over the last century. Beside experimental studies, many computational models have also been developed, with different degrees of chemical details and, therefore, general validity. In this Chapter a brief introduction on liquid crystal phases, their properties and computational studies is given, with major attention on the liquid crystal called 4,4'-diheptylazoxybenzene (HAB). This LC exhibits both a smectic and a nematic phase and belongs to the azoxybenzene family, one of the first to have been studied: since its first synthesis in 1972, HAB has been widely characterized, thanks to its various technological appealing properties. The wealth of experimental data available and the lack of any computational investigations made him an intriguing and ideal candidate for *in silico* studies. This is the reason why HAB was chosen as benchmark for the validation and development of a force-field parameterization route (Chapter 2 and 3).

1.1 Liquid crystal phases

Liquid crystals (LCs) are state of matter with properties between those of liquids and solids and are therefore said to be *mesophases*. They may be seen as having liquid-like order in at least one direction and possessing a degree of anisotropy which is characteristic of some sort

of order [26, 27]. The latter requirement is typically met if the molecules are anisotropic, for example rod-like (prolate) or disk-like (oblate).

The presence of orientational order in a system of rod-like molecules results in a nematic phase, that is a phase in which the constituting molecules have their principal symmetry axes aligned, on average, parallel to a well defined spatial direction **n**, said director. This degree of order is denoted by the orientational order parameter S (also called P_2):

$$S = \left\langle \frac{3}{2} cos^2\theta - \frac{1}{2} \right\rangle \tag{1.1}$$

where the mean value $\langle \cdots \rangle$ is obtained averaging on all molecules composing the system and θ is the angle between the molecular long axes and the director. If the molecules are on average parallel to **n**, the value of S is positive and ranges from 0 (absence of orientational order) to 1 (crystalline order). This preferential alignment makes some physical properties of nematic LCs such direction-dependent that they are usually described by second rank tensors.

The presence of positional order in one direction in a nematic phase leads to a smectic phase. Here, the molecules are arranged in layers so that a one-dimensional periodicity results in the density profile along the **n** direction. The smectic order parameter representing the positional order can be written as:

$$\tau = \left\langle \left| exp\left(\frac{2\pi i \mathbf{r} \cdot \mathbf{e}}{d} \right) \right| \right\rangle \tag{1.2}$$

where the mean value $\langle \cdots \rangle$ is obtained as above, averaging on all molecules of the system, **r** is the position of the molecular center of mass, **e** is the unit vector normal to the smectic layers and d is the layer separation. Transitions between the isotropic liquid and the smectic (Sm) or nematic (N) phase are first order while transitions between N and Sm phases may be either first or second order, depending upon the coupling between the orientational and the positional order and therefore on the range of existence of the N phase [28].

Organic molecules that can be seen as rods of length to diameter ratio roughly 3 - 8 exhibit various mesophases at different temperatures and hence are generically referred to as thermotropic LCs. A common feature of all molecules of this type is that they have a rigid central core connected to a flexible alkyl chain at one or both ends. Thermotropic LC phases are various and different. Some of them are free from both chirality and molecular tilt, which means that **n** and the layer normal are collinear (as in nematics or SmA). In others the director is not perpendicular to the layer normal, but makes a relatively large angle (as in smectic-C). In third ones chirality is present, as in cholesteric phases or in smectic-C*, where

the director maintains a constant angle with respect to the layer normal while describing a helical path as the sample is traversed along the direction normal to the smectic planes.

1.1.1 Physical properties

The preferential alignment of molecules in LC materials makes the physical properties of these phases direction-dependent. This anisotropy can be seen, for example, in the dielectric susceptibility. This is a scalar quantity in isotropic phases and **P**, the induced polarization, is parallel to the direction of the applied electric field, **E**. On the contrary, in nematic phases **P** is not necessarily parallel to **E** and χ^e, the dielectric susceptibility, is a a tensor of rank two, which physically reflects the fact that the induced polarization depends on the direction of the applied field relative to the symmetry axes of the nematic. However, for uniaxial nematic liquid phases, the number of independent components is reduced to two: parallel and perpendicular to the director. This means that in such phases the capacitance measurements will yield a value of $\epsilon_{\parallel}$ or $\epsilon_{\perp}$. The difference of these two values

$$\Delta\epsilon = \epsilon_{\parallel} - \epsilon_{\perp} \tag{1.3}$$

is the dielectric anisotropy, which vanishes in the isotropic phase.

A similar situation is seen for diamagnetic properties. The molecules in a LC material are anisotropic, so the magnitude of an induced magnetic moment depends on the relative orientation of the applied field with respect to the molecular axes. The diamagnetic susceptibility is defined as:

$$\Delta\chi = \chi_{\parallel} - \chi_{\perp} \tag{1.4}$$

where $\chi_{\parallel}$ is the magnetic susceptibility parallel to the director and $\chi_{\perp}$ is the magnetic susceptibility perpendicular to it.

Anisotropy is reflected in optical properties as well, such as birefringence. LCs, in fact, demonstrate *double refraction*: light parallel-polarized to the director has a different index of refraction (extraordinary refractive index, $n_{\parallel}$) than light polarized perpendicular to the director (ordinary refractive index, $n_{\perp}$).

Finally, much of the interest in LCs is associated with the fact that the orientation of the director can locally be influenced by external stimuli. Elastic constants and viscosity appear intimately involved in the description of these phenomena and they are consequently the focus of extensive studies.

1.1.2 Characterization

A variety of techniques can be used in the characterization of LC phases, but the initial determination of mesomorphic properties for a new compound is usually made with thermal techniques, such as differential thermal analysis (DTA) or differential scanning calorimetry (DSC), and polarizing microscopy [28]. In fact, different LC phases will appear to have distinct textures when viewed under a microscope using a polarized light source. These textures depend on the alignment of the molecules in relationship to the slide: parallel (homogeneous), perpendicular (homeotropic), or a mixture of these two. This orientation depends on the structure of the molecule itself and on the surfaces of the slide and cover slip. Colors can be seen only under polarized light and only in colorless mesogens: they are dependent on the thickness of the sample, thus they will be more intense where the sample is thinner, such as along the sample edges, or near the clearing temperature.

X-ray diffraction provides one of the most definitive ways to determine the structure of LC phases. Here, external fields are used to compete with the surface anchoring potential imposed by cell boundaries in order to orient the sample. Most LCs can be aligned by heating them to their isotropic phase and then slowly cooling them into a LC phase in the presence of an external magnetic field. The molecules in the nematic phase are thus free to reorient under the torque produced by the magnetic field, due to the diamagnetic anisotropy $\Delta\chi$. The effectiveness of the field in aligning a specific sample depends on the magnitude and sign of $\Delta\chi$.

The study of LC orientational order by NMR may also help at the phase identification. It can give important information on molecular conformations, as well as on dynamic processes involving the whole molecules, fragments or aggregates of them.

As previously said, calamitic LCs are usually made up of a rigid central core and of flexible chains at one or both ends. It is the rigid core (where connecting groups can also be found, such as azo or azoxy spacers) to establish the primary shape of the molecule and its rigidity. Consequently it also defines the approximate temperature range where mesophases will occur and what types of mesophases are possible. However, a rod-like rigid core rarely produces mesophases: terminal substituents are needed to balance this rigidity with flexibility. Extensive studies have been done to relate the effect of alkylic/alkoxy chains, along with their length, on mesomorphic properties (see Ref. [28] and references therein). This has been accomplished by determining the mesomorphic properties for a wide variety of homologue series of mesogens. Typical features of nearly all homologous series of rod-like molecules are, for ex-

ample, an odd-even alternating, clearing temperature and a gradual evolution of mesophases of N, SmA, SmB, SmC with increasing chain length. Nematic phases generally occur at short to mid-chain length, first increasing in phase length with increasing chain length and then decreasing at longer chain length. As the range of existence of the nematic phase decreases, the smectic one appears increasing, at first, with the chain length and decreasing later on with a further increase of the chain length.

1.2 4,4'-diheptylazoxybenzene (HAB): a liquid crystal

4,4'-diheptylazoxybenzene (HAB) is a mesogenic molecule belonging to the azoxybenzene category, one of the earliest known group of liquid crystalline compounds (see Ref. [29] and references therein). It was first synthesized by Van der Veen and coworkers in 1972 [30], through oxidation of *p*-n-heptylaniline with H_2O_2 (this synthesis was later improved in 1990 by Neubert and Sabol-Keast [31]). Since then HAB has been extensively studied. At first, it was considered as being useful in display devices, but it was subsequently found unsuitable, as well as the other *p*-n-alkylazoxybenzenes, because of their colored nature [29] and new applications were sought.

HAB shows both a smectic-A and a nematic phase. Transition temperatures are 34° (307 K), 53° (326 K) and 71.5° C (344.5 K), respectively for the crystal → smectic-A, smectic-A → nematic and nematic → isotropic phase transitions. Lower homologues of the azoxybenzene series, 4,4'-propyl, butyl and pentylazoxybenzenes, do not exhibit smectic behavior and only show nematic phases which increase their stability range with n, the number of methylene units in the alkylic side tails (see Table 1.1). A further increase in the chain length results in the appearance of the smectic phase (monotropic for n = 6): the n = 8 member of the series has the same mesomorphic behavior as HAB, but the smectic and nematic phases are $\sim 10°$ wider and narrower, respectively. Finally, chain lengths with n > 8 cause the disappearance of nematic phases and the shortening of the smectic interval. Table 1.1 lists the transition temperatures for all homologues with $3 \leq n \leq 10$: the general structure-mesogenic properties relationship for calamitic molecules described in Section 1.1 is here confirmed.

The very first investigations on HAB were based on calorimetry: the enthalpy change at the smectic-A → nematic transition was measured via DTA for all the above homologues in 1973 [32]. For n = 6 the transition is practically second order, with almost no heat of transition being detectable and for n = 8 it is clearly first order: ΔH of HAB stands in the

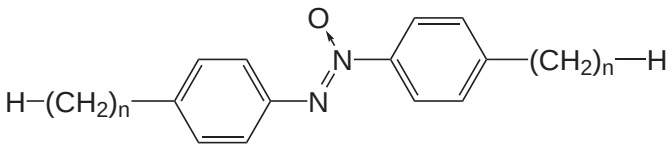

n	C		S		N		I
3	*	66.0 - 66.5	-		*	(61.5)	*
4	*	13.5 - 14.5	-		*	27.5	*
5	*	22.0	-		*	65.0	*
6	*	21.5 - 22.0	-	(17.0)	*	50.5	*
7	*	34.0 - 34.5	*	53.5	*	71.5	*
8	*	40.5 - 41.0	*	67.5	*	69.5	*
9	*	45.0 - 45.5	*		-	77.5	*
10	*	50.5 - 51.0	*		-	77.0	*

Table 1.1: 4,4'-di-*n*-alkylazoxybenzene homologues. Transition temperatures are in °C. Temperature in bracketts (T_m) means a monotropic transition at T_m, only attainable by cooling. A star indicates the presence of the phase (C = crystal, S = smectic, N = nematic, I = isotropic liquid) while a dash means the absence of the corresponding phase. All data are taken from Ref. [30].

middle and the transition can be defined as weakly first order.

This smectic → nematic transformation is an example of a simple transition at which a system freezes (or melts) in one dimension and it has been deeply investigated (see, for example, [33]). Notwithstanding that, its detailed nature still remains poorly understood as investigations are made even more complicated by the fact that near T_{SmAN} there is a strong coupling between smectic and nematic order parameters. More the nematic range is narrow, more the nematic order parameters do not saturate before the NA transition occurs [28]. In fact, as the smectic order parameter grows, it forces the nematic order parameters to do the same. HAB behavior near the NA transition has been studied in pure bulk ([34]), in mixtures ([35], [36]) and in free-standing films ([37]). These films have a well-controlled size and a high degree of uniformity, with thicknesses varying from two to over hundreds of layers. They thin layer by layer and they are ideal model systems for the investigation of the crossover from three-dimensional to two-dimensional behavior, as well as of the influence of the surfaces on some physical properties.

During 1970s and 1980s many properties of HAB were studied: optical, electrical, magnetic and viscoelastic properties were investigated in bulk, in mixtures and in films. Much

of the interest in the liquid crystalline behavior of HAB, in fact, was associated with its possible application in LC devices. Consequently, all properties connected to *orientation* were explored, first of all the possibility to locally influence the director by external stimuli.
The response to electric and magnetic fields were the first to be investigated. HAB dielectric anisotropy ($\Delta\epsilon = \epsilon_{\parallel} - \epsilon_{\perp}$) was studied both in the smectic and nematic range in 1973 [38, 39], and in 1981 [40, 41], while the anisotropy of the diamagnetic susceptibility ($\Delta\chi = \chi_{\parallel} - \chi_{\perp}$) of the smectic phase was measured using polarizability data in 1981 [42] and ^{1}H NMR [43] in 1982. In the same years elastic constants too were explored [44]: in 1977 de Jeu and Claassen studied the K_1, K_2 and K_3 elastic constants observing the deformation of the director pattern of a thin nematic slab due to the torque of a variable magnetic field orthogonal to the director (Frederiks transitions). In 1983 it was viscosity's turn: γ_1, the viscosity coefficient important for switching times in LCs displays, was measured in the nematic phase [45].
Dynamics processes were also investigated: in 2004 Urban and co-workers [46] (and before in 1994 Forte *et al.* [47]) studied HAB relaxation processes using broad band dielectric spectroscopy and NMR. The low frequency relaxation time was connected with molecular reorientation around the short axes while the high frequency one was connected with the rotation around the long axes. Suitable theoretical models were used to derive the diffusional coefficients of spinning ($D_{\parallel}$) and tumbling ($D_{\perp}$). Understanding the rotational dynamics in LC phases is of fundamental importance for the development of new, improved LC displays: the anisotropy of LC systems creates a specific environment for the rotations of whole molecules. Rodlike molecules such as HAB in the nematic phase can rotate around their principal axes of inertia and with respect to the director. The complexity of these motions is increased, on one hand, by the fact that they occur on very different time scales, ranging from seconds to picoseconds, and, on the other hand, by possible dynamical coupling with intramolecular vibrations. While some relaxation processes are well separated in the frequency domain, other processes overlap, which makes it difficult to separate them in the measured spectra. In 2006 Zajac and co-workers [48] studied the molecular rotational dynamics of HAB using quasi-elastic neutron scattering and ^{13}C cross-polarization magic-angle-spinning NMR. For HAB, other available data refer to density and thermal expansion coefficients [49], to the characterization of the smectic phase [50, 51, 52], to the flow alignment angle in nematic phase [53], and, obviously, to birefringence [54, 33].

But the interest in HAB was not due only to its possible applications in LC devices. On the contrary, it can be found in many different fields over the years. Searching for new

materials with interesting properties by a technological point of view, HAB has been used to produce both cholesteric phases, by dissolving a chiral nitroxide probe in its nematic phase (1982, [55]), and ferronematic phases, by adding spherical shaped nanoparticle into the thermotropic LC phase (2008, [56]). Ferronematics are magnetic colloids, based on a liquid crystal matrix, possessing higher magnetic susceptibility with respect to that of the pure LC: they promise to provide an optical device technology based on magnetic switching.

Moreover, HAB has also been used onto substrate into contact with self-assembled block copolymers films in order to explore novel LC director patterns [57].

LCs have also demonstrated unusual lubrificant properties: HAB, in particular, was studied as a lubrificant additive to oils in 1997 [58], when it was found to significantly reduce friction coefficients and wear rates, even at room temperature.

Its surface tension (γ) was measured in 1998 [59] on free standing films in the smectic phase: this study was important for the comprehension of the mechanisms underlying the phenomena of surface tension itself and thus as a starting point for the understanding of basic processes such as wetting, adhesion, friction, spreading and detergency.

HAB photoalignment properties were studied, as well, in 2006 [60]. Applications of LCs imply a good homogeneous orientation of the director in a working cell. The orienting element of the LC cell is its surface, whose orienting ability is associated with the anisotropic surface tension called *anchoring*. Nazarenko *et al.* studied bare solid surfaces, sufficiently transparent to UV light, with different adsorbed molecules (among them HAB) whose only common property was the anisotropy of light adsorption. They found that these surfaces can be made-photooriented by the UV light thanks to a selective desorption.

Various works have also been devoted to the investigation of the effects of HAB's LC phases on different solutes [61, 62], as well as to its orienting properties as a solvent in NMR studies [61, 63].

Finally, a new interest has arisen in the last years around azo and azoxybenzene compounds for cyclometallation reactions: these compounds have shown a strong tendency to form, with palladium precursors, cyclopalladated five-membered rings containing square-planar palladium (II) centers. The stability of the resulting metal-containing ring is the reason of the growing interest, since it can be regarded as possible intermediate in metal-catalyzed C-H bond activations [64].

1.3 *In silico* liquid crystal: computational models

In the theoretical approach to LC field, as well as to material science, computer simulations methods such as Monte Carlo (MC) and molecular dynamics (MD) are by far the most employed and many reviews have appeared on the subject [65, 66, 20, 67, 14, 15].
The structural and dynamic macroscopic properties, obtained through simulations, are derived from the adoption of a model potential, which contains the description of the molecular framework and interactions. The molecular models, adopted to translate a real physical molecule in a simulation object can be grouped into four different categories with increasing order of complexity: the lattice model, the hard nonspherical models, the soft nonspherical models and atom-atom potential models. Some of the major pioneering works are presented in the following Sections.

1.3.1 Lattice models

The lattice model is the simplest generic model for LC systems. Here, the system under study is a set of classical spin vectors located on the sites of a cubic lattice. The simplest realization of this model is a pair potential with nearest neighbor interactions of the form:

$$U_{ij} = -\frac{\epsilon}{2}\left(3cos^2\theta_{ij} - 1\right) \tag{1.5}$$

where Θ_{ij} is the angle between the two vectors, and ϵ is an energy parameter. In this model each site does not represent an individual molecule, but a small region of the liquid and the spin symbolize the locally-arranged nematic ordering within that region. The spins are free to rotate about their centers of mass, subject to interactions, but not to translate. This lattice model was proposed by Lebwohl and Lasher [68] in the 1970s as the first simulation model for a nematic. Introducing additional terms in the simple potential above, the model can account for other effects, such as local head-tail asymmetry (See for example Ref. [67] and references therein).

1.3.2 Molecular models

This category is the next step in the complexity ladder for LC molecular models. It groups together all the models in which freely-translating particles are used to represent individual molecules. The earliest works in this area concentrated on molecular shape alone and employed models of rigid, anisotropic particles. This approach was justified by Onsager's

proof that orientational ordering could be seen in a purely steric system of spherocylinders (cylinders of length L, diameter D, with hemispherical caps at the ends) when the density was increased above a threshold [69] (1949).

This category includes both hard and soft non-spherical models.

The hard non-spherical models consider that the liquid structure is dominated by the sharply repulsive interactions occurring between the atoms as they approach each other at short distances, and model these interactions using an infinitely steep hard sphere potential. The effects of attractive interactions are omitted. The earliest simulation work on hard particle of LCs was Viellard-Baron's investigation of the behavior of hard ellipsoids in the early 1970s, using Monte Carlo simulations [70]. Unfortunately, the simulation themselves were restricted to short runs, thus definite conclusions could not be drawn on the question of three-dimensional orientationally ordered phases. More than a decade elapsed before LC phases were definitely observed: for hard ellipsoids, the region of stability of nematic LC phases was established by Frenkel and co-workers with Monte Carlo simulations [71, 72]. Studies by Allen (1990) [73] and Camp and Allen (1997) [74] of a biaxial version of the hard ellipsoid model then showed the formation of isotropic, nematic and biaxial phases.

Another frequently used steric model for calamitic LC behavior is the hard spherocylinder. This model can be seen as a sphere which has been uniformly elongated, or compressed, in one direction. The spherocylinder, the model used by Onsager for his proof of density-driven N-I transition, is characterized by the axial ratio $e = a/b$, where a is the length of the major symmetry axis and b the length of the two equivalent minor, perpendicular axes. Values of $e > 1$ correspond to prolate, cigar-shaped ellipsoids and $e < 1$ to oblate disk-shaped ones ($e = 1$ means the familiar hard-sphere case). The first computer simulation on such a system was again performed by Vieillard-Baron in 1974 [75]. A decade later Stroobants *et al* [76] found that a system of perfectly parallel spherocylinders forms a smectic-A phase between the nematic and crystalline ones. Later on, Veerman and Frenkel revisited Vieillard-Baron's hard spherocylinder systems with full orientational freedom [77]. A more complete phase diagram was later proposed by McGrother *et al* [78] and refined and extended up to the Onsager limit by Bolhuis and Frenkel [79].

The next degree of sophistication beyond hard particles is the soft body model. Here the molecular shape is still represented in a simple way, but as the particle is soft long-range attractions between molecules are also included. Such potentials are essentially anisotropic versions of the Lennard-Jones potential used in atomistic simulations. Temperature can play

now a role in determining thermodynamic equilibrium, a feature which is absent in hard-particle models. Applications of such models are dominated by variants of the Gay-Berne (GB) model [80], a single-site model for uniaxial ellipsoid of revolution in which the particle shape and interaction well depth can both be made anisotropic. The interaction potential features a steep repulsive part, modeling the overlap between the electron clouds, and an attractive tail at larger intermolecular separations. It has the following form:

$$U(\hat{u}_i, \hat{u}_j, \hat{r_{ij}}) = 4\epsilon(\hat{u}_i, \hat{u}_j, \hat{r}_{ij}) \left\{ \left[\frac{\sigma_0}{r_{ij} - \sigma(\hat{u}_i, \hat{u}_j, \hat{r}_{ij}) + \sigma_0} \right]^{12} - \left[\frac{\sigma_0}{r_{ij} - \sigma(\hat{u}_i, \hat{u}_j, \hat{r}_{ij}) + \sigma_0} \right]^{6} \right\} \quad (1.6)$$

where $\hat{u}_i$ and $\hat{u}_j$ are the unit vectors defining the orientation of sites i and j respectively. $\hat{r}_{ij}$ is the unit vector of the distance between the two interacting GB sites. ϵ and σ are two parameters having the physical dimensions of energy and distance, respectively. The anisotropy of the interactions is contained in the expressions for $\epsilon(\hat{u}_i, \hat{u}_j, \hat{r}_{ij})$ and $\sigma(\hat{u}_i, \hat{u}_j, \hat{r}_{ij})$, both depending on the orientations of the two molecules and on the intermolecular vector. Some extensions of the Gay-Berne model have been proposed to generalize the model to biaxial particles as well as to mixtures (i.e. [81, 82]).

1.3.3 Atomistic models

LC materials are characterized by an exquisitely sensitive dependence of macroscopic properties on molecular structure that tracks back to a complex interplay of a variety of subtle energetic and entropic effects. Electrostatic, dispersion, induction, excluded volume effects, as well as positional, orientational and conformational entropy all concur to the interaction landscape and they all are modulated by the functional groups present in the LC molecules. This articulate interplay leads to a situation in which different thermodynamic states are quite close in free energy. Consequently, minor changes in the chemical structure can shift the free energy balance between competing phases, dramatically changing the phase behavior of the material and correspondingly its properties (mechanical, electrical, optical and transport properties, for example)[66].

Due to this delicate balance of entropic and enthalpic effects, idealized models may not always be suitable for LC simulations. In order to understand fine effects (or, for example, the role of molecular flexibility) more detailed aspects of the molecular structure have to be included in the simulation model. In other words, a higher degree of *realism* is needed. This involves representing the molecular structure with something approaching atomic detail, that is why such models are referred to as *atomistic* or *atomic-detail* models. In particular,

according to an explicit or implicit description of the alkylic hydrogens, full-atomistic (FA) and united-atom (UA) models can also be distinguished.

Atomistic models use molecular mechanics potential of the general form:

$$E = \sum_{bonds} E_{bonds} + \sum_{angles} E_{angles} + \sum_{dihedrals} E_{torsions} + \sum_{i} \sum_{j>i} E_{nonbonded} \tag{1.7}$$

where the first three terms constitute the intramolecular energy (made up of the stretching, bending and torsional contributions) and the fourth one is the intermolecular interaction. The latter is usually modeled via a Coloumb potential part, for the electrostatic contribution, and via a Lennard-Jones 12-6, for the steric/van der Waals ones. Looking at Eq. 1.7 two major drawbacks of this atomistic degree of *realism* are immediately apparent. First, the computational effort is well higher than that of previous models and it heavily depends on the number of the non-bonded pair interactions in the system. Second, a looking-like picture of the real molecule can be obtained only using highly accurate force-fields. The first reported atomistic simulation of LCs dates back to 1989 [83]. This work was an attempt to examine the specific effects of the charge distribution around the molecular framework on the stability of the nematic phase of 4-n-pentyl-4'-cyanobiphenyl (5CB). A system of 64 molecules was simulated for a total time of 60 ps, clearly far too short a time to equilibrate even such a small sample.

A decade later, the simulation time had already grown up of one order of magnitude. In 1998, in fact, McBride *et al.* [84] carried on an MD simulation of another LC, namely 4,4'-di-n-pentyl-bicyclo[2.2.2]octane. Two systems of respectively 64 and 125 nonpolar (without charges) UA-molecules were followed up to 12 ns: the growth of orientational order from the isotropic phase was observed. However, the simulation found a nematic phase, instead of the real smectic, with a temperature transition $\sim 100^\circ$ C lower than the experimental one.

One year later, in 1999, atomistic simulations were employed to show how the positional ordering of a photoactive solute (p,p'-diheptylazobenzene, 7AB) in a smectic host (4-octyl-4'-cyanobiphenyl, 8CB) depended sensitively on its photochemical state [85]. This system was made up of a hundred of molecules, modeled full-atomistic except for the alkylic chains which were treated with an UA approach, and run lengths were of ~ 6 ns.

The first thousand-molecule atomistic simulation of a mesogenic system is the one of Wilson and co-workers, in 2001 [86]. They followed an isotropic phase of an all-atom model of 4-(*trans*-4-n-pentylcyclohexyl) benzonitrile (PCH5) for ~ 7 ns, obtaining density and diffusion coefficients in good agreement with experimental results.

Only three years later, the state-of-the-art simulated time increased again of one order, reaching 60 ns on a full-atomistic system of 98 molecules of phenyl aminocinnamates, succeeding in reproducing the experimental T_{NI} [87].

The above computational evidences show that two features are fundamental to the success of an atomistic simulation on LCs, beside the use of an appropriate force-field: long time-scales, which are required to establish nematic stability, and non-trivial system-size, necessary to reduce the order of magnitude of fluctuations. A proof of the reliability of the employed model may be searched for in the prediction of the phase density and of the T_{NI}, which is crucial in designing viable LC display materials that have to exist and operate in a certain range of temperature.

Among the first reproductions of the experimental T_{NI} with atomistic simulation is that of Peláez and Wilson in 2006 [88]. In particular, they were able to grow a nematic phase from an isotropic liquid in its correct experimental range of existence. 50 ns were necessary to obtain orientational order in a system of 256 bent-core LC molecules, modeled full-atomistic. This is quite a long time, compared to the one needed by nonpolar systems of united atom (10, 15 ns) as shown in the work of McBride *et al.* [84] and Hanna *et al.* [89].

Nowaday the trend in atomistic simulation is still going in the direction of longer simulated time window and of larger system [90, 91, 92, 93]. Cacelli *et al.* found a 192 molecule stable nematic phase within 10 K from the experimental one: the ergodicity of this phase of 5CB was assessed observing how three differently ordered phases reached the same P_2 value at the same temperature (in one of these run a spontaneous reordering was observed) in ~ 40 ns [91]. The same accuracy was achieved for other homologues of the same series. Prampolini *et al* in 2008 [92] carried on lengthy runs of more than 70 ns on systems of more than 800 molecules to determine the T_{NI} of the 4-n-pentyloxy-4'-cyanobiphenyl (5OCB) LC. They succeeded in observing a spontaneous onset of orientational order in the system, upon cooling. Finally, a spontaneous ordered nematic upon cooling was observed by Tiberio *et al.*, as well, two years later, in samples of 250 molecules of n-cyanobiphenyls [93].

It is clear that the history and the success of the atomistic simulations are intimately coupled to the technological progresses in CPU speed, to the development of parallel computing techniques as well as of speeding-up algorithms which scale with something smaller than N^2, where N is the number of interacting sites (see for example the Ewald summation scheme for long-range electrostatic interactions [94]). These are the factors which still determine the feasibility of the simulation and decide for how long a system of a certain size can reasonably

be observed.

Finally, in order to explore longer time windows or bigger systems, other approaches can be used, such as coarse-grained ones. These are simplified models in which groups of atoms are treated together as a single interaction site. Notwithstanding a certain loss of *realism*, they can still be capable of capturing the main physics of the problem while reducing computational expense [95, 96].

CHAPTER

2

HAB, UNITED ATOM APPROACH

HAB (4,4'-diheptylazoxybenzene), a mesogenic molecule, is here employed to test an *ab initio* parameterization route to tailored force fields (FF). The computational approach is united-atom, aimed at the construction of a force field suitable for molecular dynamics simulations. In this Chapter the whole route is presented and organized in its three main steps: first, QM calculations are performed to access inter and intra molecular potentials, then the computed energies are parameterized with analytical model potentials and finally MD simulations are run. Comparison of the resulting macroscopic properties with the relevant experimental data are also addressed. These results have been published in the article "Chemical Detail Force Fields for Mesogenic Molecules", J. Chem. Theory Comput., **5**, 1865, (2009) [97].

2.1 Force field parameterization

In Chapter 1 it has been said how CPU speeds determine the combination of system size - time window that can be handled in simulation. Here, it has to be stressed that the other fundamental requisite to the success of an atomistic simulation is a good force field (FF). More the simulation model resembles the real sample, more MD observables will be in good agreement with experimental data (provided a system with a sufficient number of molecules and a sufficient observation time window). Traditionally, there have been two main routes towards *realistic* potentials for computer simulations.

The most widely employed scheme is based on an *a posteriori* strategy. In this approach, for a given class of molecules (for example hydrocarbons or aromatic compounds), the set of parameters specifying the FF are initially obtained from experimental and theoretical data

and they are eventually adjusted in order to reproduce some target macroscopic properties, such as crystal cell parameters, experimental density or vaporization enthalpy. The result is a two-body effective potential where many-body effects are incorporated in the fitted parameters, because they are inherent in the experimental data. This approach dates back to the 1970s, when the first empirical FFs for biomolecular simulation were developed (see, for example Ref. [98] and references therein). Biomolecular simulation has come a long way since then and a number of empirical FFs has been developed for simulations of proteins, nucleic acids, lipids and other biological molecules. Well-known parameter sets belong to this category, for example OPLS [99, 100, 101, 102], AMBER [103, 104, 9] and CHARMM [105], which have been refined various times over the years. Many reviews have been published on the subject discussing the status and the progresses of these empirical force fields [98, 106]. Although capable of excellent results, this kind of scheme suffers from some disadvantages. First it relies heavily on empirical input, that often is unavailable. Second, FF parameters are tuned for a well defined thermodynamic state so it is unlikely that their quality stays the same in different thermodynamic conditions: good results are guaranteed only in the limited range of pressure and temperature where the parameterization occurred. Third, they are general FFs, derived for classes of molecules: parameter transferability has always to be invoked for and often that is not sufficient. It is habit, at least as far as LC simulations are concerned, to tailor these sets using them just as a starting point for a further tuning on the target molecule. For example, intermolecular interaction σ and ϵ parameters may be adjusted so to reproduce the density or the clearing temperature of the specific LC under study [93]. This further tuning means that three-body effects become accounted for in an average way, but it does not guarantee accurate results.

The other possible approach to accurate FF construction consists in deriving the model potential from first principle calculations [107, 108, 109, 110, 111]. A number of Quantum Mechanical (QM) calculations is carried out to model a simplified potential to be used in simulation. This route presents several advantages. First, the ab initio derived interaction potentials are not driven by experimental data. This allows for the construction of FFs even for molecules whose properties are difficult to measure and, in principle, it gives the approach predictive capabilities. Second, the FF is suited for the chosen molecule: it takes into account for the specific chemical background and no degree of transferability must be invoked. On the other hand, the QM route may be more involved and computationally expensive. For example, tailoring an intermolecular FF requires the creation of a large energy

vs geometry database computed at a suitable post Hartree-Fock in order to properly account for the dispersion energy: this becomes quickly unfeasible with the increasing of molecular dimensions. Moreover, since these potentials are derived from dimer calculations, they do not account for three-body interactions. Whether three-body interactions should be taken into account for in FF parameterization and simulation is a thorny problem. They were found necessary in early simulations on liquid Argon [112] and Argon-Krypton mixtures [113], but in 2004 a work on benzene [114] showed that an accurate *ab initio* derived two-body potential was capable to account for several bulk properties with an overall performance comparable to that of an OPLS effective potential [115].
Here, for HAB, an *ab initio* derived route to tailored intra and intermolecular parameters was chosen.

2.1.1 The simulation model

The HAB molecule (namely 4,4-diheptylazoxybenzene, see Section 1.2) was described with a full atomistic model, except for the aliphatic hydrogens which are grouped with the chain carbon they are bonded to, in an united atom description, for a total of 37 interaction sites per molecule (see Figure 2.1).

2.1.2 Intramolecular force field

The intramolecular parameterization consisted on fitting stretching, bending and torsional parameters on QM derived quantities. This was achieved through a least square minimization of a functional involving differences between the parameterized model energy, gradients and Hessian, and the corresponding QM data.
The model intramolecular contribution to the FF, E^{intra}, was parameterized on HAB smaller homologue 4,4'-dibutylazoxybenzene (BAB, see Figure 2.1), which differs from the target molecule for six methylene units (three at each side chain). This seemed a reasonable choice as it reduced computational time and the UA parameters describing the flexibility of the longer chains (HAB) were not expected to be much different from those obtained for the smaller homologue (BAB).
E^{intra} was chosen in the following diagonal form:

$$E^{intra} = E^{stretch} + E^{bend} + E^{Rtors} + E^{Ftors} + E^{LJintra} \tag{2.1}$$

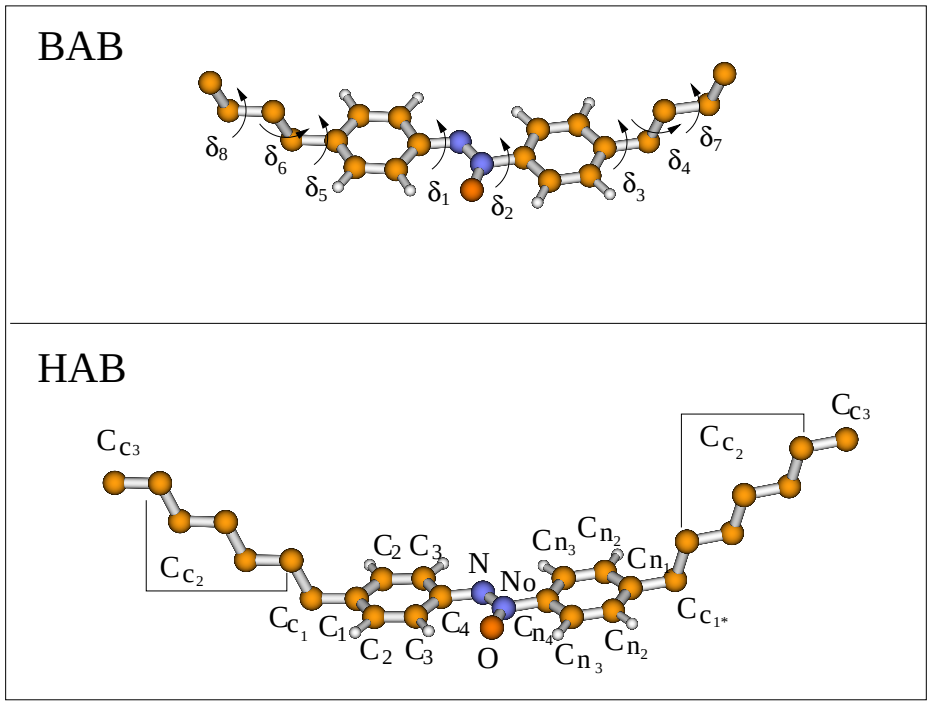

Figure 2.1: Model adopted for HAB molecule (bottom panel) and flexible dihedral definition in BAB (4,4'-dibutylazoxybenzene) homologue, employed for the intramolecular parameterization (top panel). All aromatic hydrogens are labeled after the carbon atom they belong to, *i.e.* H_{n3} is the hydrogen bonded to the C_{n3} atom.

where the terms are the stretching, bending, torsional (rigid and flexible) and intramolecular Lennard-Jones 12-6 contributions, respectively. These terms were modeled with different analytical expressions according on the internal coordinate involved. In HAB, bond lengths, bond angles and those dihedral angles determining the aromatic ring planarity were considered as "rigid" coordinates, because they do not sensibly alter their value from the equilibrium one, near room temperature. For them it was employed an harmonic description of the potential:

$$E^{stretch} = \frac{1}{2}\sum_{\mu}^{N_s} k_\mu^s (r_\mu - r_\mu^0)^2 \tag{2.2}$$

$$E^{bend} = \frac{1}{2}\sum_{\mu}^{N_b} k_\mu^b (\theta_\mu - \theta_\mu^0)^2 \tag{2.3}$$

$$E^{Rtors} = \frac{1}{2}\sum_{\mu}^{N_{Rt}} k_\mu^t (\phi_\mu - \phi_\mu^0)^2 \tag{2.4}$$

where $k_\mu^s, k_\mu^b, k_\mu^t$ and $r_\mu^0, \theta_\mu^0, \phi_\mu^0$ are the force constants and equilibrium values for stretching, bending and rigid torsional internal coordinates (μ), respectively. Conversely, dihedrals δ_1 -

δ_8 reported in Figure 2.1 were treated as flexible coordinates: the harmonic approximation fails in describing their potential, since their energy profile allows them to assume several values between 0° and 360° at room temperature. Therefore, they were described through a cosine expansion:

$$E^{Ftors} = \sum_{\mu}^{N_{Fdihedrals}} \sum_{j=1}^{N_\mu} k^d_{j\mu}[1 + cos(n^j_\mu \delta_\mu - \gamma^j_\mu)] \tag{2.5}$$

where $k^d_{j\mu}$ is the force constant, δ_μ the flexible dihedral, n^j_μ and γ^j_μ the multiplicity and a phase factor for the j^{th} cosine. N_μ is the number of cosine functions employed for dihedral μ.

Among these dihedrals, δ_1 is the angle between the aromatic ring bonded to the site labeled N and the azoxy bridge plane; δ_2 is the analogue of δ_1 referred to the other ring; δ_3 and δ_5 are the angles formed by the aromatic ring plane and the plane containing the first two atoms of the aliphatic chain. Finally, δ_4 and δ_6 - δ_8 are the dihedral angles driving the flexibility of the aliphatic chains.

The fitting was performed with the JOYCE program [116] and the functional to be minimized, I^{intra}, was the following:

$$\begin{aligned} I^{intra} \quad = \quad & \sum_{g=0}^{N_{geom}} \left(W_g[U_g - E^{intra}_g]^2 + \sum_{K=1}^{3N-6} \frac{W'_{Kg}}{3N-6} \left[G_K - \left(\frac{\partial E^{intra}}{\partial Q_K} \right) \right]^2_g + \right. \\ & \left. \sum_{L}^{3N-6} \sum_{K \geq L}^{3N-6} \frac{2W''_{KLg}}{(3N-6)(3N-5)} \left[H_{KL} - \left(\frac{\partial^2 E^{intra}}{\partial Q_K \partial Q_L} \right) \right]^2_g \right) \end{aligned} \tag{2.6}$$

where N_{geom} is the number of sampled conformations, Q_K is the K^{th} normal coordinate, W, W'_K and W''_{KL} are weights and U, G_K and H_{KL} are the QM energy, gradient and Hessian, respectively. Choosing W'_K and W''_{KL} equal to zero for all geometries except for the equilibrium one, 2.6 simplifies to:

$$I^{intra} = \sum_{g=0}^{N_{geom}} W_g \left[U_g - E^{intra}_g \right]^2 + \sum_{K \leq L}^{3N-6} \frac{2W''_{KL}}{(3N-6)(3N-5)} \left[H_{KL} - \left(\frac{\partial^2 E^{intra}}{\partial Q_K \partial Q_L} \right) \right]^2_{g=0} \tag{2.7}$$

where it is clear as the QM Hessian matrix H_{KL} and the FF Hessian are evaluated only at the absolute minimum $g = 0$.

N_{geom} is a set of 42 geometries: the optimized BAB geometry and different conformations obtained with torsional scans of the flexible dihedrals. The absolute energy minimum was obtained by a complete geometry optimization at DFT level, using the B3LYP functional [117] with the correlation consistent basis set cc-pVDZ. Energy profiles for flexible dihedrals

δ_1 to δ_6 were obtained by performing geometry optimizations (B3LYP/cc-pVDZ) without any restriction but the investigated torsional angle, which was sampled with steps of 30° in the [0° - 180°] range. No sampling was performed for δ_7 and δ_8, and their description was made through the parameters reported for *n*-butane [118], assuming the transferability of this torsional potential. All calculations were performed with the GAUSSIAN 03 package [119].

A few details of the fitting procedure have still to be said. First, the torsional energy fitting was performed within the Frozen Internal Rotation Approximation [116]. Second, two different weights W_g were chosen: 0.0076 for the conformations with a low internal energy and 0.0019 for all the others, in order to obtain a more accurate description of the lowest energy geometries. Third, the diagonal and off diagonal elements of the weight matrix W'' were set to 0.05 Å^4 and 0.025 Å^4, respectively.

With these specifications, the JOYCE fitting procedure yielded an overall standard deviation of 0.044 kJ/mol, with maximum error on energies of 1.7 kJ/mol. The resulting optimized parameters are reported in Tables 2.1 - 2.4.

The torsional profiles for δ_1 - δ_8 are reported in Figure 2.2 which shows the very good agreement between the DFT computed energies and the *ab initio* derived torsional curves. The lowest energy of δ_1 and δ_2 is at 0°, with a torsional barrier of $\sim$ 25 kJ/mol at 90°, meaning that at the equilibrium geometry the azoxy group and the aromatic rings are coplanar. On the contrary, δ_3 and δ_5 prefer a 90° conformation, as found at the aliphatic-aromatic linkage in more simple compounds such as ethylbenzene [120]. The energy profile *vs* both chain dihedrals, δ_4 and δ_6, has an absolute minimum at 180°(*trans* conformation) and a relative one at ±60°(*gauche* conformations) separated by rather high barriers. As expected, the torsional potential curves of the chain dihedrals δ_4 and δ_6 are in excellent accord with those of *n*-butane (see Figure 2.2), confirming that this potential can be confidently transferred to all aliphatic chain dihedrals.

Extending the fitted intramolecular potential to the HAB molecule was straightforward: by looking at the bottom panels of Figure 2.2 it is clear that all the inner chain dihedrals behave in similar manner, as the fitted torsional profile for δ_4 and δ_6 exactly traces out the δ_7, δ_8 shape, which is transferred from *n*-butane.

A fortiori, the force constants of the more rigid internal coordinates, such as methylene-methylene bond stretching and angle bending, are also expected to be transferable from those computed for the BAB smaller chains.

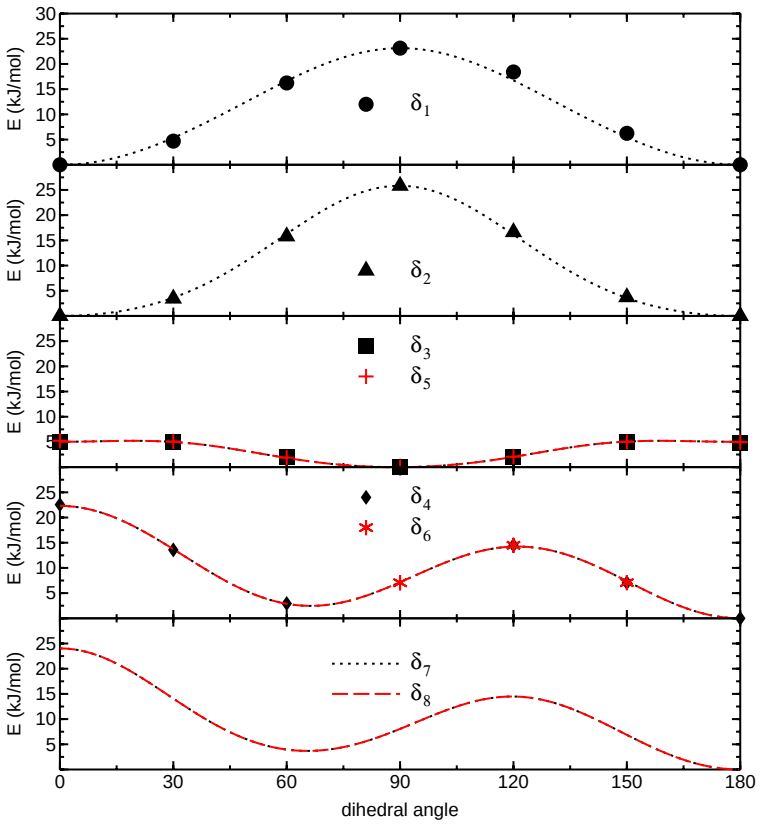

Figure 2.2: BAB (4,4'-dibutylazoxybenzene): proper torsions. Symbols represent the sampled points while dashed lines are curves obtained with the model parameterized potential E^{intra}. Only the region 0° - 180° is shown because of symmetry reasons.

However, following the experience on the liquid crystal 5CB [121], some intramolecular LJ terms were added to the FF to both prevent an unphysical curling of the aliphatic chain on the core and on itself and to correctly take into account intramolecular interaction between the aromatic rings and the methyl group [122]. Pair interaction parameters were added between aromatic carbons and chain UA sites at least 5 bonds apart and between methylic and methylenic chain groups 6 bonds apart. Finally, pair interaction parameters were also added to describe the interaction between the $H_{2(n2)}$ and the methylenic group bonded to $C_{c1(*)}$ (see Table 2.5).

Stretching parameters

Bond	r_0 (Å)	k^s (kJ/(mol Å^2))	Bond	r_0 (Å)	k^s (kJ/(mol Å^2))
C_{c1}-C_1	1.511	2699	C_{c1*}-C_{n1}	1.512	2699
C_1-C_2	1.403	2766	C_{n2}-C_{n1}	1.405	2766
C_2-C_3	1.392	3377	C_{n3}-C_{n2}	1.394	3377
C_3-C_4	1.415	3083	C_{n3}-C_{n4}	1.397	3083
C_2-H_2	1.093	3368	C_{n2}-H_{n2}	1.093	3368
C_3-H_3	1.087	3368	C_{n3}-H_{n3}	1.088	3368
C_4-N	1.400	2841	C_{c3}-C_{c2}	1.530	2644
N-N_O	1.281	4124	C_{c1}-C_{c2}	1.541	2308
N_O-O	1.254	3960	C_{c1*}-C_{c2}	1.541	2308
N_O-C_{n4}	1.467	1925	C_{c2}-C_{c2}	1.532	2308

Table 2.1: BAB: Optimized stretching parameters.

Bending parameters

Angle	θ_0 (°)	k^b (kJ/(mol·rad^2))	Angle	θ_0 (°)	k^b (kJ/(mol·rad^2))
$C_{c1}\widehat{C_1}C_2$	121.2	896.7	$C_{c1*}\widehat{C_{n1}}C_{n2}$	120.9	896.7
$C_1\widehat{C_{c1}}C_{c2}$	113.2	760.6	$C_{n1}\widehat{C_{c1*}}C_{c2}$	113.1	760.6
$C_2\widehat{C_1}C_2$	117.7	449.5	$C_{n2}\widehat{C_{n1}}C_{n2}$	118.0	434.1
$C_1\widehat{C_2}C_3$	122.3	434.1	$C_{n1}\widehat{C_{n2}}C_{n3}$	121.5	434.2
$C_2\widehat{C_3}C_4$	119.6	968.7	$C_{n2}\widehat{C_{n3}}C_{n4}$	118.9	968.8
$C_3\widehat{C_4}C_3$	118.1	245.2	$C_{n3}\widehat{C_{n4}}C_{n3}$	121.0	245.2
$C_1\widehat{C_2}H_2$ $C_3\widehat{C_2}H_2$ $C_2\widehat{C_3}H_3$ $C_4\widehat{C_3}H_3$	120.0	317.5	$C_{n1}\widehat{C_{n2}}H_{n2}$ $C_{n3}\widehat{C_{n2}}H_{n2}$ $C_{n2}\widehat{C_{n3}}H_{n3}$ $C_{n4}\widehat{C_{n3}}H_{n3}$	120.0	317.5
$C_3\widehat{C_4}N$	120.0	431.0	$N_O\widehat{C_{n4}}C_{n3}$	120.0	666.5
$C_4\widehat{N}N_O$	121.2	785.2	$N\widehat{N_O}C_{n4}$	115.1	103.6
$N\widehat{N_O}O$	128.0	705.2	$C_{n4}\widehat{N_O}O$	116.9	757.0
$C_{c3}\widehat{C_{c2}}C_{c2}$	113.2	836.9	$C_{c2}\widehat{C_{c2}}C_{c3}$	113.1	836.9
$C_{c1*}\widehat{C_{c2}}C_{c2}$	113.2	836.9	$C_{c1}\widehat{C_{c2}}C_{c2}$	113.3	836.9

Table 2.2: BAB: Optimized bending parameters.

Rigid torsion parameters

Dihedral Angle	ϕ_0 (°)	k^t (kJ/(mol·rad^2))	Dihedral Angle	ϕ_0 (°)	k^t (kJ/(mol·rad^2))
$C_{c1}\widehat{C_1C_2}C_3$	180.0	100.4	$C_{c1*}\widehat{C_{n1}C_{n2}}C_{n3}$	180.0	100.4
$C_{c1}\widehat{C_1C_2}H_2$	0.0	59.05	$C_{c1*}\widehat{C_{n1}C_{n2}}H_{n2}$	0.0	59.05
$C_2\widehat{C_1C_2}C_3$	0.0	87.54	$C_{n2}\widehat{C_{n1}C_{n2}}C_{n3}$	0.0	87.54
$C_1\widehat{C_2C_3}C_4$			$C_{n1}\widehat{C_{n2}C_{n3}}C_{n4}$		
$C_2\widehat{C_3C_4}C_3$			$C_{n2}\widehat{C_{n3}C_{n4}}C_{n3}$		
$C_2\widehat{C_1C_2}H_2$	180	65.37	$C_{n2}\widehat{C_{n1}C_{n2}}H_{n2}$	180	65.37
$C_1\widehat{C_2C_3}H_3$			$C_{n1}\widehat{C_{n2}C_{n3}}H_{n3}$		
$C_4\widehat{C_3C_2}H_2$			$C_{n4}\widehat{C_{n3}C_{n2}}H_{n2}$		
$C_3\widehat{C_4C_3}H_3$			$C_{n3}\widehat{C_{n4}C_{n3}}H_{n3}$		
$H_2\widehat{C_2C_3}H_3$	0.0	36.16	$H_{n2}\widehat{C_{n2}C_{n3}}H_{n3}$	0.0	36.16
$C_2\widehat{C_3C_4}N$	180.0	30.18	$C_{n2}\widehat{C_{n3}C_{n4}}N_O$	180.0	189.1
$H_3\widehat{C_3C_4}N$	0.0	59.22	$H_{n3}\widehat{C_{n3}C_{n4}}N_O$	0.0	59.22
$C_4\widehat{NN_O}O$	0.0	222.5	$C_4\widehat{NN_O}C_{n4}$	180.0	248.7

Table 2.3: BAB: Optimized rigid torsion parameters.

Flexible torsion parameters

Dihedral Angle	n	k^d (kJ/mol)	Dihedral Angle	n	k^d (kJ/mol)
$C_3\widehat{C_4N}N_O$ (δ_1)	0	0.998	$(O)N\widehat{N_O}C_{n4}C_{n3}$ (δ_2)	0	1.997
	2	-5.739		2	-3.205
	4	0.174		4	0.502
	6	-0.047		6	-0.025
$C_{n2}C_{n1}\widehat{C_{c1*}}C_{c2}(\delta_3)$	0	1.997	$C_2C_1\widehat{C_{c1}}C_{c2}$ (δ_5)	0	1.997
	2	1.358		2	1.358
	4	-0.325		4	-0.325
	6	-0.099		6	-0.099
$C_1C_{c1}\widehat{C_{c2}}C_{c2}$ (δ_6)	0	0.998	$C_{n1}C_{c1*}\widehat{C_{c2}}C_{c2}$ (δ_4)	0	0.998
	1	3.657		1	3.657
	2	1.995		2	1.995
	3	7.504		3	7.504
	4	-0.263		4	-0.263
$C_{c3}C_{c2}\widehat{C_{c2}}C_{c1*}$ (δ_7)	0	-2.106	$C_{c3}C_{c2}\widehat{C_{c2}}C_{c1}$ (δ_8)	0	-2.106
	1	4.330		1	4.330
	2	1.738		2	1.738
	3	7.520		3	7.520
	4	0.126		4	0.126
	5	0.172		5	0.172
	6	0.241		6	0.241

Table 2.4: BAB: Optimized flexible torsion parameters.

Intramolecular LJ parameters

Site $\cdots$ Site	σ (Å)	ϵ (kJ/mol)
$C_{c2}^{***} \cdots C_a$	3.30	0.69
$C_{c2}^{**} \cdots C_a$	3.56	0.69
$C_{c2}^{*} \cdots C_a$	3.56	0.69
$C_{c3} \cdots C_a$	3.56	0.69
$C_{c3} \cdots C_{c2}^{c1(*)}$	4.34	0.021
$C_{c2}^{c1(*)} \cdots H_{2(n2)}$	4.80	0.004

Table 2.5: HAB: intramolecular LJ parameters. C_a indicates an aromatic carbon site; C_{c2}^{*} is the C_{c2} site bonded to the C_{c3} one; C_{c2}^{**} and C_{c2}^{***} are the sites that follow along the aliphatic chain. Finally $C_{c2}^{c1(*)}$ represents the C_{c2} bonded to $C_{c1(*)}$.

2.1.3 Intermolecular force field

Intermolecular interactions were modeled through a pair potential and the intermolecular parameters were obtained fitting a model function onto a database of QM dimer energies. Due to the HAB molecular size, to the consistent number of geometries to be sampled, and to the necessary high level of theory, QM energies could not be computed directly on the whole dimer, but they were recovered via Fragmentation Reconstruction Method (FRM) [25, 123].

FRM fragmentation scheme

A correct reproduction of Van der Waals interactions is fundamental for an accurate computation of intermolecular energies for all neutral molecules and in particular for those containing aromatic rings. The nature of these interactions is purely quantum mechanical and strongly relies on a correct representation of the dynamical electron correlation. For this reason, within the *ab initio* methods, it is necessary to employ suitable post-Hartree–Fock (HF) techniques, whose computational cost dramatically increases along with molecular dimensions. Several strategies based on fragmentation have been proposed over the years to overcome this problem [25, 123, 124, 125, 126, 127, 128, 129, 130], which rely on the possibility of dividing the whole system into small sub-systems and performing the calculations of interaction energies for each sub-system.

FRM was proposed by the Pisa group of Liquid Crystals in 2002 [25, 123]. The idea is that the interaction energy of a dimer can be approximated to a good accuracy as a sum of energy contributions between the pairs of fragments which concur to form both molecules. As an example a simple AB molecule can be considered, where A and B are two moieties connected by a single bond. Formally, the whole molecule can be written as

$$\mathrm{AB} \rightarrow \mathrm{AI_a} + \mathrm{I_bB} - \mathrm{I_aI_b}$$

where $\mathrm{I_a}$ and $\mathrm{I_b}$ are intruder groups. They are first included to saturate A and B valence and then removed as the molecule $\mathrm{I_aI_b}$. The spatial position of the fragments is the same of the whole molecule, whereas the location of the intruder $\mathrm{I_a}$ and $\mathrm{I_b}$ is determined by the equilibrium geometry of the saturated fragments $\mathrm{AI_a}$ and $\mathrm{I_bB}$, which normally correspond to stable molecules. The simplest case is when $\mathrm{I_a}$ and $\mathrm{I_b}$ are H atoms, but the method is general and the intruder groups can be whatever (for example, saturation schemes with H atoms or $\mathrm{CH_3}$ groups were used in Ref. [131]). However, the recovered energy will depend upon the fragmentation and saturation scheme. FRM is successful only if a fundamental condition is

respected: the electronic density in A or B moiety has to be as close as possible to that in the AB un-fragmented molecule. As a consequence the intruders should mimic as much as possible the effect of the original molecular part being cut away on the electronic property of the remaining fragment.

Taking a step further in the above example, a second molecule CD interacting with AB can also be considered. Of course, CD can be the previous AB molecule just moved to a different spatial location. A similar fragmentation scheme leads to

$$\mathrm{CD} \rightarrow \mathrm{CI_c} + \mathrm{I_dD} - \mathrm{I_cI_d}$$

The complete interaction energy of the AB$\cdots$CD system can be recovered by summing up the interaction energy of all the involved pairs:

$$\begin{aligned} E(AB\cdots CD) &\rightarrow E((AI_a + I_bB - I_aI_b)\cdots(CI_c + I_dD - I_cI_d)) \\ &= E(AI_a\cdots CI_c) + E(AI_a\cdots I_dD) - E(AI_a\cdots I_cI_d) + \\ &\quad E(I_bB\cdots CI_c) + E(I_bB\cdots I_dD) - E(I_bB\cdots I_cI_d) - \\ &\quad E(I_aI_b\cdots CI_c) - E(I_aI_b\cdots I_dD) + E(I_aI_b\cdots I_cI_d) \end{aligned} \tag{2.8}$$

The sign of each term is determined by the sign in the above fragmentation schemes for AB and CD. From the last equation, the computational advantage of the FRM approach is apparent: the interaction energy is written as a sum of interaction energies of pairs well smaller than the whole AB$\cdots$CD system.

For HAB dimer the correct reproduction of Van der Waals interactions made it necessary to resort to QM methods able to recover a large part of the dispersion energy. As such QM methods scale at least as the fourth power of the number of electrons, the computational gain of the FRM can be further appreciated. Previous applications of the FRM approach [131, 92] have shown that, with a suitable choice of the method and basis set, a reliable database including many geometrical arrangements can be obtained and employed for FF parameterization.

The FRM fragmentation scheme chosen for HAB is reported in Figure 2.3. The reliability of the fragmentation using H_2 as intruder molecules along the aliphatic chain was already assessed [131]. Here, more attention has been paid to verify the quality of several possible fragmentation schemes of the aromatic core. With this aim preliminary calculations [132] were performed on the smaller homologue 4,4'-dimethylazoxybenzene. It was found that a cut along the N-C_4 bond (see Figure 2.1) was preferable to that along N_O-C_{n4}, as the

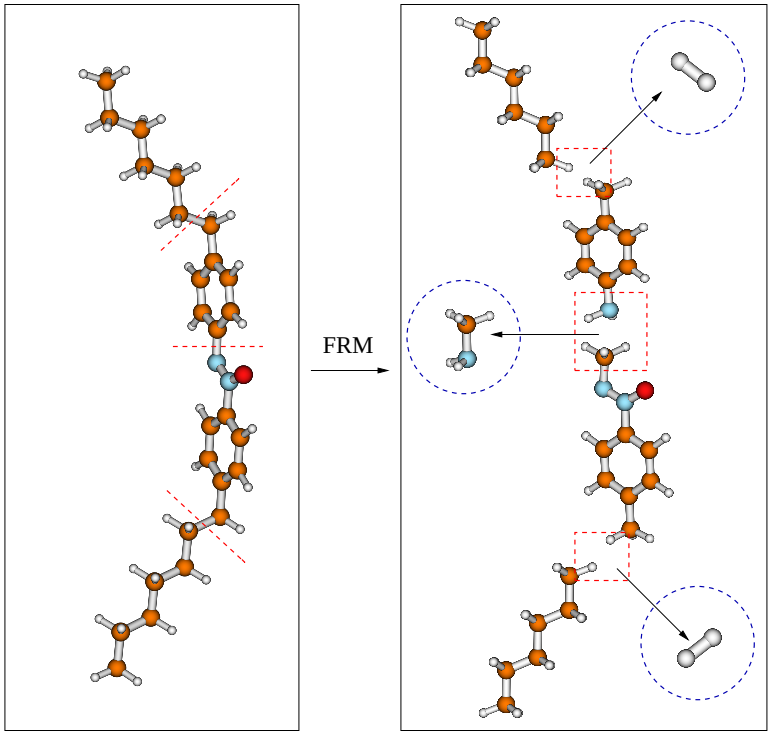

Figure 2.3: Fragmentation scheme for HAB. The fragmentation was performed by cutting bonds as shown by the red dashed lines (left panel). The four resulting fragments are shown on the right, together with the intruder fragments, which are blue circled. In the above picture, both moieties and intruder molecules have been shifted (black arrows) only for the sake of clarity (see text). For instance, CH_3 and NH_2 intruder groups lie on the C-N bond connecting the two central moieties.

electronic density distribution of the resulting fragments was more similar to that exhibited by the moieties in the whole molecule. Thus the final fragments were two hexanes, one 4-methylbenzenamine and one methyl,4-(methyl-NNO-azoxy)phenyl. The intruder molecule arising from the chosen scheme in the central core was a CH_3NH_2 molecule, as shown in Figure 2.3.

The Sampling

The absolute energy minimum of HAB was obtained by a complete geometry optimization at DFT level, using the B3LYP functional together with the correlation consistent basis set cc-pVDZ. The internal geometry of A and B monomers was kept frozen to this optimized conformation during the whole sampling, performed at MP2 level.

The low spatial symmetry of HAB made the sampling of the PES far from straightforward. However, a classification of the many dimer arrangements is still possible in terms

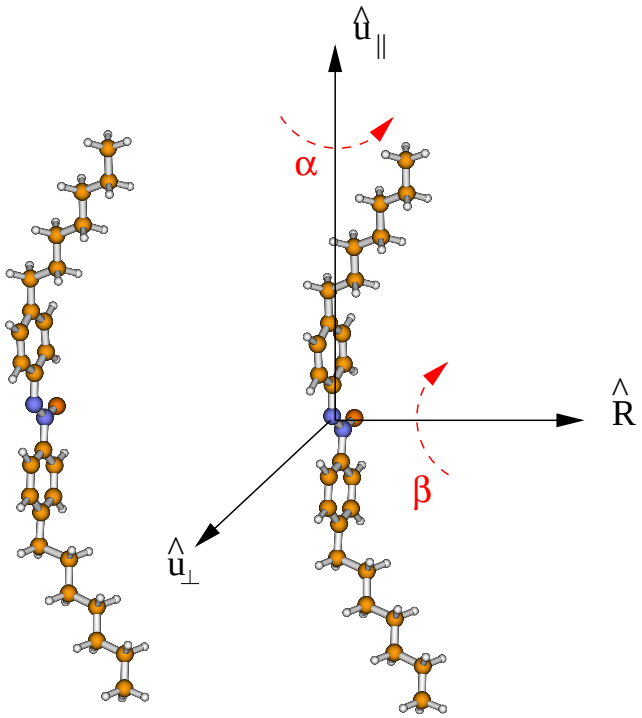

Figure 2.4: FRM sampling. Dimer arrangements are generated by displacing one HAB molecule with respect of the other by translation along $\hat{R}$, $\hat{u}_\perp$ or $\hat{u}_\parallel$ and/or rotation around α or β (γ Euler angle is not shown).

of displacement vectors ($\hat{R}$, $\hat{u}_\perp$ and $\hat{u}_\parallel$) and Euler angles (α, β and γ) [133], as reported in Figure 2.4. Face-to-face (FF) configurations can be obtained by shifting one molecule along the vector $\hat{R}$, with $\alpha = 0°$ and $\beta = 0°$ or 180°. In the former case, the vectors N_O-O point in the same direction, and the geometries obtained are labeled as parallel face-to-face (p-FF). In the latter, the vectors N_O-O point in opposite directions resulting in antiparallel (a-FF) arrangements. If both molecules are rotated by $\alpha = 90°$, the cores are found in a side-by-side disposition (p-SS or a-SS, whether $\beta = 0°$ or 180°). Side-to-face (p-SF and a-SF) geometries are obtained with a rotation of $\alpha = 90°$ of only one molecule. If the β angle is set to 90°, the two cores draw a cross and the x-FF, x-SF and x-SS arrangements can be created by applying a further rotation around the β-rotated long molecular axis of 0°, 90° on one or both molecules, respectively. Finally if one molecule is rotated around $\hat{u}_\perp$, the dimer is found in a T-shaped (TS) configuration.

Further subclasses can be created by exploiting the relative position of the side chains of the two dimer molecules. If the symbol "⊂" is used to sketch the HAB molecule, three

subclasses can be determined depending whether the alkyl chains point in the same direction ($\subset\subset$), towards each other ($\subset\supset$), or in opposite directions ($\supset\subset$).

The PES sampling was performed by computing the FRM energy of $N_{geom} \sim 2000$ geometries in the supermolecule approach with the MP2 method, and considering the Basis Set Superposition Error (BSSE) by the standard counterpoise correction [134]. A suitably 6-31G* modified basis set was used, where the exponents of the d polarization functions were decreased to $\alpha_d = 0.25$, following the suggestion of Hobza and coworkers [135, 136]. As to the benzene dimer, which can be considered as a prototype for the aromatic interactions, the interaction energies computed at the MP2/6-31G*(0.25) level were shown [135, 114, 136] to well reproduce the results of high quality calculations [137, 138]. Furthermore, the results of former FRM applications [25, 139, 114, 131, 140] suggested that this choice could be a good compromise between the accuracy required in the PES description and the high number of calculations required for an accurate sampling.

From a preliminary analysis of the resulting FRM database, the configurations with the more attractive interactions are the $\supset\subset$ ones, where the steric chain repulsion effect does not prevent the rings and the NNO group to reach their most favorable positions with respect of the same groups of the other molecule. For the same reason, less attractive energies are found for the $\subset\subset$ and $\subset\supset$ arrangements, in this order. In the latter, the steric effect

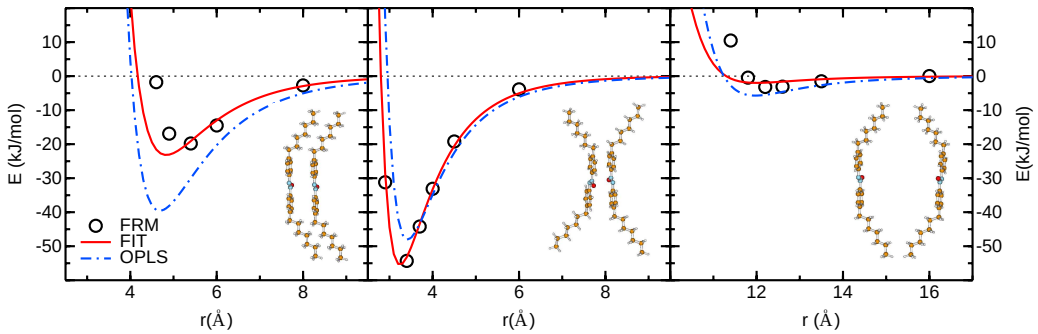

Figure 2.5: HAB computed and fitted interaction energy curves for selected geometrical arrangements: p-FF $\subset\subset$, p-FF $\supset\subset$ and p-FF $\subset\supset$. The points represent the FRM energies and the solid lines the fitted energies. OPLS predictions are also reported with dashed blue lines for comparison.

dominates and the interaction energy wells are far less deep and shifted to higher values of the displacement coordinate. For example, for the p-FF case, reported in Figure 2.5, $\supset\subset$ have a maximum interaction energy of about -50 kJ/mol, $\subset\subset$ reach -20 kJ/mol at most and

$\subset\supset$ only -5 kJ/mol. The situation is similar for the a-FF geometry: here the $\supset\subset$ is even more favorite since the oxygens point in opposite directions and the maximum interaction energy can reach -57 kJ/mol.

Among all classes, the most favored geometries are p-FF, a-FF and x-FF configurations, where the aromatic rings come closer to each other and the π interaction significantly contributes to the total interaction energy. It may be worth noticing that in the x-FF case, the aliphatic chains are not superimposed in any geometry with the result that their repulsion effect is not as important as in the previous configurations. This means that $\subset\subset$, $\subset\supset$ and $\supset\subset$ geometries show similar curves, with -40 kJ/mol maximum interaction energies in all cases. The interaction energies for the SS configurations are less attractive: the a-SS geometries do not reach -30 kJ/mol and p-SS ones arrive at -18 kJ/mol, at most. Furthermore, p-SF does not overstep the -20 kJ/mol, showing energies between the FF case and the SS one. Also the x-SF configurations are less energetic than the x-FF (-25 kJ/mol and - 40 kJ/mol, respectively). Finally TS arrangements present maximum interaction energy of about -12 kJ/mol.

As far as the contact distance is concerned, it can be noted that there are three different kind of disposition: p-FF, a-FF and x-FF configurations have a contact distance of about 3 Å, p-SS and a-SS of 6 Å and TS above 8 Å. The anisotropic nature of the HAB molecule shows up clearly from this picture. This is a well known feature of many calamitic LC: the contact distance and the well depths of all interaction curves strongly depend on the monomer relative orientations.

The fitting

The intermolecular parameters were obtained from a least square fitting procedure, by minimizing the functional

$$I^{inter} = \frac{\sum_{k=1}^{N_{geom}} (U_k^{FRM} - E_k^{inter})^2 e^{-\alpha U_k^{FRM}}}{\sum_{k=1}^{N_{geom}} e^{-\alpha U_k^{FRM}}} \tag{2.9}$$

where N_{geom} is the number of dimer geometries sampled, U_k^{FRM} is the intermolecular energy of the k^{th} dimer arrangement computed by FRM/MP2 and E_k^{inter} is the corresponding model function for the geometry k. E_k^{inter} has the following form:

$$E_k^{inter} = \sum_{i=1}^{N_{sites}} \sum_{j=1}^{N_{sites}} [E_{ij}^{LJ} + E_{ij}^{Coul}]_k = \sum_{i=1}^{N_{sites}} \sum_{j=1}^{N_{sites}} \left[4\epsilon_{ij} \left[\left(\frac{\sigma_{ij}}{r_{ij}} \right)^{12} - \left(\frac{\sigma_{ij}}{r_{ij}} \right)^{6} \right] + \frac{q_i q_j}{r_{ij}} \right]_k \tag{2.10}$$

Intermolecular parameters

Site	ϵ (kJ/mol)	σ (Å)	q (e)	Site	ϵ (kJ/mol)	σ (Å)	q (e)
C_{c1}	0.148	4.15	0.272	C_{c1*}	2.590	3.44	-0.009
C_1	1.878	2.79	-0.367	C_{n1}	1.652	2.00	-0.050
C_2	0.145	3.52	-0.043	C_{n2}	0.066	4.20	-0.066
C_3	1.076	3.38	-0.043	C_{n3}	0.664	3.10	-0.126
C_4	2.632	2.00	0.098	C_{n4}	3.402	2.69	-0.047
H_2	0.023	2.48	0.082	H_{n2}	0.053	2.00	0.119
H_3	0.074	2.35	0.048	H_{n3}	0.082	2.00	0.093
N	1.135	3.05	-0.374	C_{c2}	0.246	4.10	0.000
N_O	0.020	3.82	0.729	C_{c3}	0.020	3.70	0.240
O	0.180	3.03	-0.428				

Table 2.6: HAB: optimized intermolecular parameters.

where E_{ij}^{LJ} and E_{ij}^{Coul} are the standard 12-6 Lennard-Jones potential and the charge-charge interaction between a pair of sites i, j of two different molecules and σ_{ij} and ϵ_{ij} interaction parameters are the following:

$$\epsilon_{ij} = \sqrt{\epsilon_i \epsilon_j} \qquad \sigma_{ij} = \frac{\sigma_i + \sigma_j}{2} \tag{2.11}$$

As for other applications [114, 123], the minimization procedure of functional I^{inter} was performed by imposing for all geometries a Boltzmann-like weight with $\alpha = 1.6$ kJ/mol^{-1}. Equivalent sites (see Figure 2.1) were given the same σ, ϵ and q values.

No other constraints were imposed except for σ and q of the methylene (C_{c2}) groups of the chains. These sites were assumed chargeless since this allowed a straightforward extension of the FF to higher homologues. As to the $\sigma_{C_{c2}}$ parameter, a first fitting yielded a standard deviation of 2.22 kJ/mol, with a value (4.4 Å) significantly larger than that obtained for butane (3.905 Å [141]) or 5OCB (3.76 Å [92]). With this set of parameters, a preliminary MD run, performed in the NPT ensemble on an isotropic system of 64 HAB molecule at 1 atm and 370 K gave a density underestimated by $\sim 4\%$ with respect to the experimental value. However, another fit with $\sigma_{C_{c2}}$ reduced to 4.1 Å and a slightly larger standard deviation (2.48 kJ/mol), yielded a density within 1% of the experimental data.

The final optimized parameter set that corresponds to this fit can be seen in Table 2.6. In Figures 2.5 and 2.6, the energies obtained with FRM are compared with those predicted by

the OPLS [141, 115] empirical force field, widely employed in simulations of the liquid phase of many smaller molecules. The OPLS-FF describes the FRM energy surface with a standard deviation of 9.56 kJ/mol. This can be seen as a remarkable achievement and a proof of the

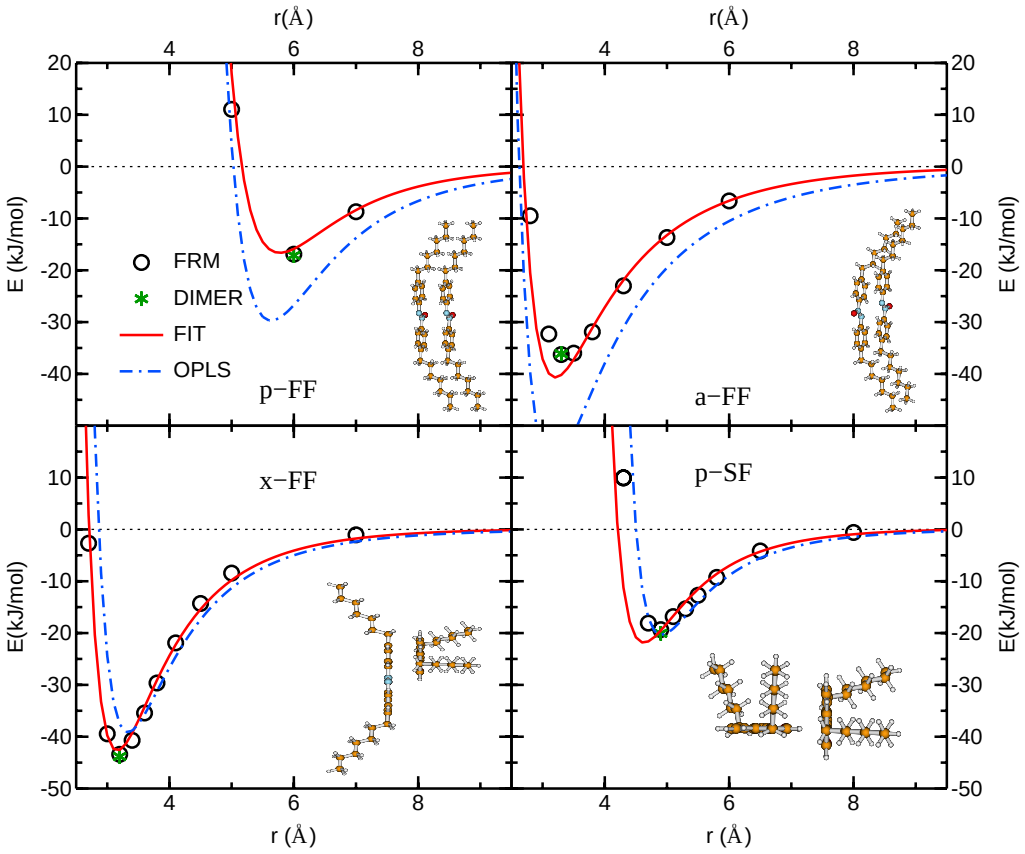

Figure 2.6: HAB computed and fitted interaction energy curves for selected geometrical arrangements: p-FF $\subset\subset$, a-FF $\subset\subset$, x-FF $\supset\subset$ and p-SF $\supset\subset$. In the first two geometries, a shift of -2 Å was applied along $\hat{u}_{\perp}$. The points represent the FRM energies and the solid lines the fitted energies. The green point marked 'DIMER' in each panel shows the interaction energy of the dimer, computed *ab initio* for the *whole* molecules (no FRM, see text). OPLS predictions are also reported with dashed blue lines for comparison.

good transferability of the OPLS parameters. Nevertheless, the extreme sensitivity of the properties of liquid crystalline materials to even minor changes of the molecular structures and interactions supports the need of a more accurate representation of the FRM PES, as attained by our fitting procedure, which led to the standard deviation of 2.48 kJ/mol. (See also Figures 2.5 - 2.6 for a visual estimate of the agreement at a few selected configurations). The need of an accurate description of the PES is also apparent if we consider that the FRM approach is able to reproduce the interaction energies of HAB dimers with great accuracy,

as Figure 2.6 shows. In each panel of this Figure a point labeled DIMER is included. It corresponds to the *ab initio* interaction energy of the dimer in that configuration without using the FRM scheme. The results of Figure 2.6 prove two things. First, the FRM gives an excellent agreement with the MP2 value of the interaction energy (e.g. -17.1 *vs* -16.9 kJ/mol with the FRM for the p-FF arrangement). Second, the employed fit faithfully describes the sampled PES.

As a test of the predictive capability of the *ab initio* derived FF, the energy curves of some unsampled geometries were calculated with the model function and using FRM. The results are reported in Figure 2.7, together with the OPLS predictions. In the top panel an energy curve for a β rotation is shown. One HAB molecule was also translated by 2 Å along $\hat{u}_\perp$, 3.5 Å along $\hat{R}$ and rotated by $\alpha = 180°$. Here, both curves are in good agreement with the FRM points. The central panel shows an interaction energy curve obtained by displacing

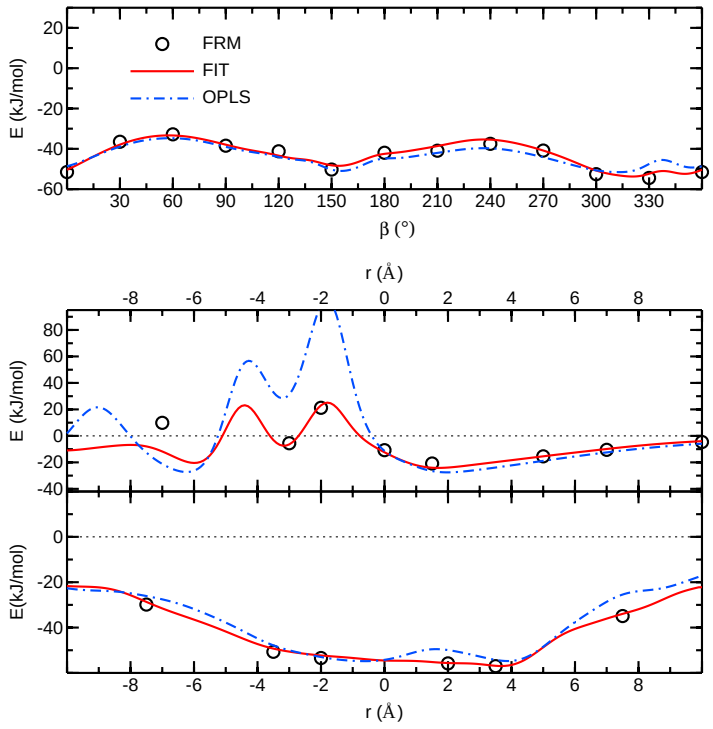

Figure 2.7: HAB interaction energy predicted by the fitting function (solid line) and control FRM values (open circles). The OPLS prediction is also shown (dashed line).

one molecule along the $u_\parallel$ direction, with a shift of 2.5 Å along $\hat{u}_\perp$, 4.0 Å along $\hat{R}$ and a rotation of $\alpha = 40°$ and $\beta = 50°$. In this case the fitted curve traces out the FRM point

positions better than the OPLS. Finally, in the third panel, a similar curve is reported for an a-FF $\supset\subset$ type, obtained by displacing the second molecule along $u_{\parallel}$ after a translation of 3.4 Å along $\hat{R}$, and a 180° rotation of both α and β. Even if the OPLS prediction is not so far from the FRM points, the fitted curve is significantly closer to the FRM data.

2.2 MD simulations

2.2.1 Computational details

The *ab initio* derived FF, obtained as shown above, was employed for MD simulations carried out with a parallel version of a the Moscito4.0 [142] package on systems of 210 and 600 HAB molecules. In all runs bond lengths were kept fixed at their equilibrium value using SHAKE algorithm [143] which allowed for using a timestep of 2 fs. Charge-charge long range forces were treated with the particle mesh Ewald method [144, 145], using a convergence parameter α of $5.36/2\mathrm{R}_c$ and a fourth order spline interpolation, while the short range interactions were truncated at $\mathrm{R}_c = 10$ Å, employing standard corrections for energy and virial [112]. In the NPT ensemble, temperature and pressure were kept constant using the weak coupling scheme of Berendsen *et al.* [146].

The equilibration of the resulting trajectories was assessed by monitoring the mass density (ρ), the positional and orientational order *vs* the simulation time. The phase director n was identified as the eigenvector corresponding to the largest eigenvalue of the Saupe ordering matrix $\hat{\mathbf{Q}}$, whose elements are

$$Q_{ab} = \Big\langle \frac{1}{2}(3u_a u_b - \delta_{ab}) \Big\rangle \tag{2.12}$$

where the mean value $\Big\langle ... \Big\rangle$ is obtained averaging on all molecules composing the system and $\mathbf{u}$ (a = x,y,z) is the unit vector of HAB molecular long axis. The orientational order was measured through the second rank order parameter P_2, computed as the maximum eigenvalue of $\hat{\mathbf{Q}}$. Positional order was monitored by computing the positional order parameter τ

$$\tau = \Big\langle \Big| exp\Big(2\pi i \frac{\mathbf{r}\cdot\mathbf{e}}{d}\Big) \Big| \Big\rangle \tag{2.13}$$

where $\mathbf{r}$ is the position of the molecular center of mass and $\mathbf{e}$ is the unit vector normal to the smectic layers and d is the layer separation. The latter is unknown and is optimized in order to maximize τ, since this ensures that the average we obtain has the same periodicity as the translational distribution function [147].

Once equilibrated, HAB systems at several temperatures were simulated in the NVE ensemble to calculate some dynamical properties, such as the isotropic translational diffusion coefficient D and the shear viscosity η_S. The former was computed as proportional to the long time limit of the center of mass mean square displacement (MSD)

$$D = \lim_{t\to\infty} D(t) = \lim_{t\to\infty} \frac{1}{6t}\Big\langle \Big[\mathbf{r}(t) - \mathbf{r}(0)\Big]^2 \Big\rangle \tag{2.14}$$

where $\Big\langle ... \Big\rangle$ means a double average over all configurations and molecules. The shear viscosity was computed as

$$\eta_S = \lim_{t\to\infty} \frac{V}{6k_BT} \int_0^t C_\sigma(t')dt' \tag{2.15}$$

where V is the volume of the simulation box, k_B the Boltzmann constant and $C_\sigma(t')$ the correlation function of the off-diagonal elements of the stress tensor $\hat{\boldsymbol{\sigma}}$ [148]. Due to the long time scales that characterize the collective dynamics of these systems, it was necessary to extrapolate the value of η_S from a fitting with a double exponential function (as in Ref. [149]).

2.2.2 Bulk simulations

MD simulations were carried out on condensed phases of HAB in the NPT and NVE ensembles. The first type of conditions were used to search for the transition temperatures, while the latter were adopted for the calculation of dynamic properties. In all cases, the largest number of molecules affordable with the available technologies was used. The chosen simulation box was cubic, to prevent any artificial ordering of the sample, induced *e.g.* by an elongated box.
210 HAB molecules were considered a sensible starting point, mainly for the simulation of the isotropic phase. However, a larger system of 600 molecules (corresponding to 22200 interaction sites) was adopted to study the ordered phases and to evaluate the system size effect on the results.

The isotropic phase was obtained starting from a 6x7x5 cubic lattice disposition where the HAB centers of mass were placed on the nodes, with the long molecular axis aligned along one of the box axes ($\hat{z}$). The system was equilibrated in the NPT ensemble at 400 K for 5 ns and then cooled at 380 K, and in successive steps at 370 K, 350 K, 330 K and 300 K. Given that the experimental [49] nematic-isotropic transition takes place at 342 K, the temperatures relevant for the isotropic phase are 350 K and 370 K.

The system of 600 molecules was obtained from a lattice structure in a cubic box at low density which was later compressed to the isotropic liquid density. After equilibration, an

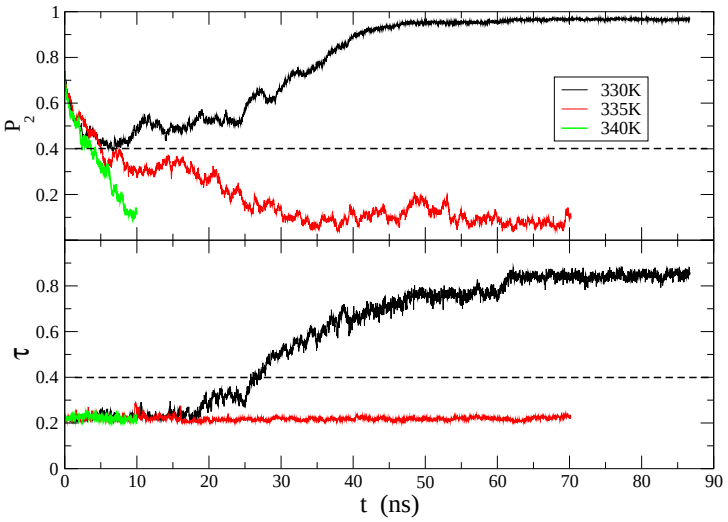

Figure 2.8: Time evolution of orientational, P_2, and positional, τ, order parameter at three temperatures for the system with 600 molecules. Horizontal dashed lines represent the conventional orientational and positional order threshold.

orienting field was applied for 0.5 ns under NPT conditions (T = 340 K). The field was able to produce a P_2 value of 0.74 with no positional order. Later, the field was switched off and this metastable state used as a common starting configuration for three runs at 340, 335 and 330 K. The evolution of the orientational and positional order parameter was then followed for some tens of ns, with the results shown in Figure 2.8. These data show clearly the existence of a smectic phase at 330 K and an isotropic phase at 335 and 340 K. This might indicate that our model did not lead to the nematic phase of HAB. However, it must be stressed that reproducing by atomistic simulation a phase that spans a range of temperature of just $\simeq$ 10 K is a formidable challenge [150].

As to the smectic phase, our analysis found an inter-layer spacing of $\simeq$ 22.5 Å significantly smaller than the experimental value of 28.9 Å (which corresponds to a tilt angle of $\simeq 18^\circ$) [50] found in a smectic A phase. As a consequence it is likely that our system was not arranged in a smectic A phase. However, it is certainly encouraging to observe a spontaneous positional reordering at a temperature just above the experimental smectic-nematic transition temperature (327 K [49]). The layered structure of the smectic phase is apparent in the left

panel of Figure 2.9; in the right panel a snapshot of the isotropic phase is shown.

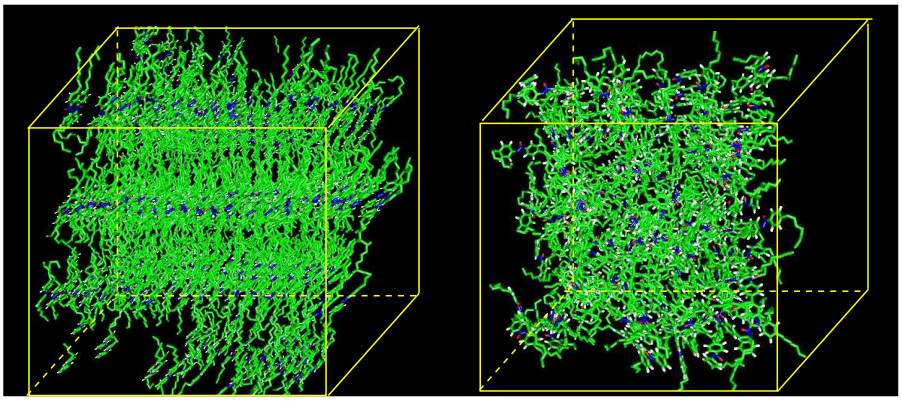

Figure 2.9: Snapshots of the smectic (left, T = 330 K, 600 molecules) and isotropic (right, T = 340 K, 210 molecules) phases of the simulated HAB systems.

In the case of the isotropic phase, the MD density values at atmospheric pressure are in very good agreement with the experimental data [49], with errors always below 1% (see Table 2.7). Previous experience showed that a good reproduction of density is essential, not only for a correct description of the structure of the system, but also for an accurate evaluation of dynamic properties, e.g. diffusion, which is extremely sensitive to the density in these materials.

Translational diffusion was evaluated from trajectories obtained in NVE runs, at four different temperatures in the isotropic phase. The same data were also used for a collective dynamical property, namely shear viscosity.

As far as diffusion is concerned, for all trajectories the MSDs were computed according to Eq. 2.14 using a 4 ns correlation time window and the curves are reported in Figure 2.10. The computed translational diffusion coefficient is reported in Table 2.7 together with its experimental counterpart [151], which is reproduced to a good extent. The Arrhenius treatment of the temperature dependence of D leads to an activation energy of 33.4 KJ/mol, also in good agreement with the experimental data of 31.9 kJ/mol [151]. Upon supercooling the isotropic system down to 330 and 300 K, a subdiffusive behavior becomes apparent, with the β relaxation regime plateau between 1 and 10 ps [152]. This is the same time window already found in a previous work on supercooled isotropic mesogens [91, 153], so it may be considered a fairly general feature of this kind of materials.

Density and translational diffusion results

T	$\rho_{exp}^{(a)}$	ρ_{MD}^{NPT}	T_{NVE}	ρ_{MD}^{NVE}	$D_{exp}^{(a)}$	D_{MD}
(K)	(g/cm^3)	(g/cm^3)	(K)	(g/cm^3)	$(10^{-10}m^2/s)$	$(10^{-10}m^2/s)$
300	1.002	-	302.0	0.972	0.27	0.23± 0.01
330	0.964	-	330.4	0.947	0.80	1.04± 0.04
350	0.939	0.930 ± 0.004	353.0	0.931	1.71	1.82± 0.06
370	0.915	0.914 ± 0.004	373.5	0.913	3.10	3.05± 0.01
380	0.902	0.906 ± 0.003	-	-	-	-
400	0.877	0.889 ± 0.003	-	-	-	-

Table 2.7: Experimental and simulated results of density and translational diffusion coefficient in the isotropic phase. At T = 300 K and T = 330 K ρ_{exp} means the density of the supercooled isotropic phase, *i.e.* that extrapolated from experimental densities in the isotropic range while D was obtained from a geometric average of the longitudinal and transverse diffusion coefficients; (a) Ref.[151].

Shear viscosity, η_s, for the isotropic phase was investigated, too. This is a collective property

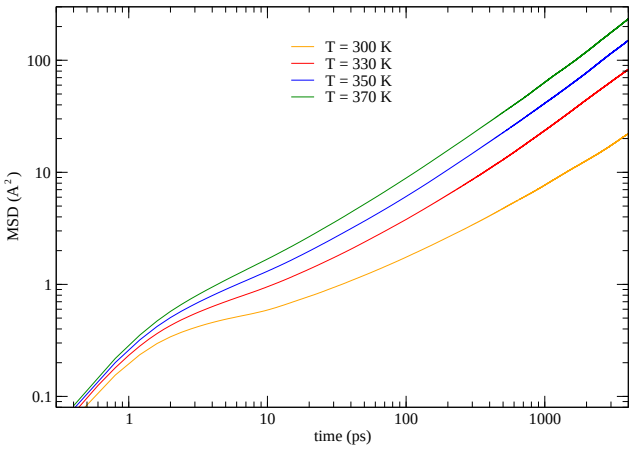

Figure 2.10: Time dependence of the MSD in the normal and supercooled isotropic phase (log-log scale).

that can be averaged only on successive time origins: as a consequence, it is affected by a larger statistical uncertainty and much longer simulations are needed to obtain reliable values for the long time limit of the function $C_\sigma(t)$ of eq. (2.15). To some extent, the situation can be improved fitting the curves with a double exponential function, as done elsewhere [149]. In Figure 2.11 the integral, whose infinite time limit yields η_s, is reported *vs* time, together

Shear viscosity	
T (K)	η_s^{MD} (mPa s)
300.2	11.9
330.4	6.3
353.0	3.8
373.5	2.1

Table 2.8: Temperature dependence of shear viscosity in the normal and supercooled isotropic phase.

with the fitting curves, where a fitting window of 0 – 400 ps was used at all temperatures. Unfortunately, experimental data are not available for HAB viscosity (to the best of our knoledge). An estimate of these MD results can be done by comparison with the corresponding experimental data for the nCB series. T = 353 K corresponds roughly to a reduced temperature of 1.05, where HAB shows (see Table 2.8) η_s = 3.8 mPa s, while experimental values for the nCB series oscillate between 10 and 20 mPa s (see Ref. [149] and references therein). Assuming [148] an inverse relationship between D and η_s, the experimental D value for HAB (1.71), compared to that of nCB series (0.60-1.0 (10^{-10}m^2/s) [149]), would yield a viscosity value in the range 5–10 mPa s, slightly larger than the computed value. However, only experimental data can definitely asses the accuracy of the present results.

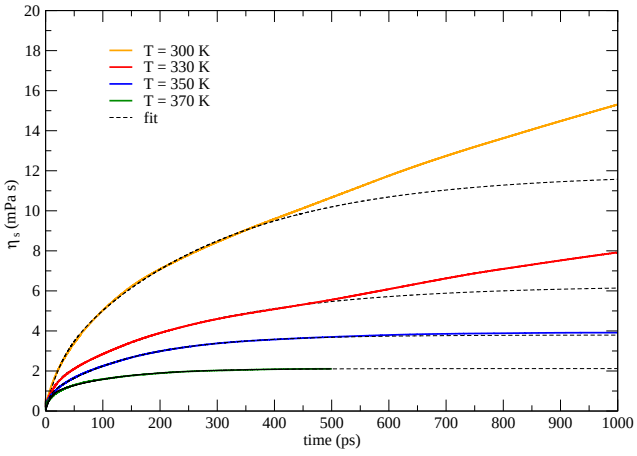

Figure 2.11: Calculation of HAB shear viscosity at different temperatures for the isotropic phase, according to equation 2.15. The exponential fits are reported in dashed lines.

2.3 Conclusions

This parameterization route led to a good reproduction of the density of the isotropic phase (within 1% of the experimental value) at several temperatures and of the diffusion coefficient D. This agreement supports some confidence that the MD results of shear viscosity also may be close to that of the real system, which are not available, to our knowledge.

In addition to the isotropic phase that appears faithfully modeled, a smectic phase at 330 K was obtained. It is rewarding that this smectic phase developed with a spontaneous positional reordering from a system with a P_2 as low as 0.4 and essentially no positional order. This locates the transition temperature to the isotropic phase between 330 and 340 K, i.e. within 10 K of the measured value of 342 K. However, from the data collected so far, the positionally ordered phase seems a SmC, instead of the SmA formed by the real system. Unfortunately, no nematic phase was detected with the present parameterization of the force field.

The incorrect smectic obtained (SmC rather than SmA) and the absence of the nematic phase indicate that some changes are necessary on the model: two are the focus issues. The first improvement would entail abandoning the hybrid model adopted so far (the hydrogens of the alkyl chains are fused to the carbon they are linked to). At a significant increase of the number of interaction sites and hence computational time, a truly full atomic model should be able to better match the *ab initio* PES. In this way the inaccuracies that now affect those geometries not included in the database for the fitting should be reduced. Consequently a more correct modeling of the phase diagram of HAB model should be achieved, given the well known sensitivity of these materials to apparently minor variations of the molecular structure and interactions.

The second point to address regards the selection of the configurations whose interaction energy is to be *ab initio* calculated. This database should include at least those configurations which are alike to be populated in bulk phases, because the goal of the FF parameterization is to reproduce bulk behavior. However, a "reference" database, which is representative of HAB bulk configurations, is not *a priori* easily constructed and the risk of excluding some important geometries is the modeling of an inaccurate potential. Instead, chemical intuition could be combined with short MD runs, from which significant dimer and/or trimer configurations could be extracted. In this way the problem of obtaining a database representative of the sample would be solved and, at the same time, a dynamical coupling between the internal

and intermolecular coordinates would be introduced. Consequently, a better exploration of the dimer PES would be achieved as the "visitable" configurations would not be limited to a six-dimensional grid any more ($\hat{R}$, $\hat{u}_{\perp}$, $\hat{u}_{\parallel}$, α, β, γ), but any internal geometry consistent with the simulation temperature and the employed intramolecular FF could be populated. These issues will be explored extensively in Chapter 3 and 4.

CHAPTER

3

HAB, FULL ATOMISTIC APPROACH

The UA parameterization route of Chapter 2 allowed for a partial reproduction of HAB experimental phase diagram: smectic and isotropic phases were detected in the correct experimental range, but no nematic phase was observed. In an attempt of improving the results, a full atomistic approach was employed modeling intermolecular interactions with a 12-6 Lennard-Jones or Buckingham potential, plus a Coulomb contribution. Unfortunately, this further atomistic detail did not succeed in detecting HAB nematic phase. Possible explanations seem to be, on one side, the parameterization of E^{inter} on a database of dimer geometries which is not fully representative of HAB bulk phases and, on the other, the use of a rigid model to sample the PES of the flexible dimer. An approach which hopefully will overcome these difficulties will be explored in Chapter 4.

3.1 Limits of the united atom approach

The united atom approach employed to tailor HAB FF (Chapter 2) has been shown capable of good results, but also affected by some limits. On one side, it does predict both isotropic and smectic phases in the correct experimental temperature range with density values in good agreement with literature data. On the other side, however, the model fails in a detailed description of HAB mesogenic behavior: no stable nematic phase is observed in simulation and the predicted smectic is of the C type instead of A. We think that possible explanations for these results can probably be the following:

1. accuracy of QM data.

The possibility that the QM data used for the parameterization of E^{inter} are affected by some errors and that they should be more accurately recomputed is certainly relevant, but it can not be pursued in the present context for evident computational reasons.

2. redundancy of the intermolecular parameter sets.

   This redundancy is inherently present in our approach as a consequence of fitting with a finite grid of points the continuous phase space of the dimer PES, but it is expected to be as more pronounced as the dimer energy database is small. In fact, the less dimer geometries are taken into account and the more parameter sets exist able to fit the energy data with similar standard deviations. For HAB, a set of more than 2000 dimer geometries was employed, a very demanding amount of QM data, but, nonetheless, the parameter redundancy made it necessary to resort to another additional criterion to choose one parameter set among many others. In Section 2.1, it was seen how an early fitting with the σ of methylenic groups at 4.4 Å yielded the minimum standard deviation (2.22 kJ/mol). This σ value, however, was significantly larger than that obtained, for example, for butane (3.905 Å [141]) or 5OCB (3.76 Å [92]). Consequently, according to chemical intuition, $\sigma_{C_{c2}}$ were reduced to 4.1 Å and another fitting was carried out obtaining a standard deviation of 2.48 kJ/mol. The difference between these two sets, in terms of standard deviation, was only 0.26 kJ/mol, but the effect on the bulk density was considerable: at 370 K the σ = 4.4 Å and 4.1 Å sets yielded an error of $\sim$ 4% and within 1% to the experimental value, respectively. Nevertheless, the absence of the nematic phase leads to the hypothesis that a a third *best set* might exist. How to find it is a difficult problem. A systematic tuning (see for example the study of Tiberio *et al.* on the nCB series in 2009 [93]) of all interacting parameters on the density or on other observable properties is a lengthy procedure and it has the defect of running out the *ab initio* nature of the present approach.

3. database of dimer geometries not representative of HAB bulk.

   Formally, the best force field is that obtained through a uniform sampling of the whole configurational space of the target dimer. In practice, a *complete* sampling is unfeasible and it is important to sample, at least, all those configurations that are alike to be found in real bulks. If some configurations are not sufficiently explored, the simulated phase diagram may result in large inaccuracies.

   It is probable that some populated regions of the configurational space of HAB dimer

have not been explored. In fact, from an *a posteriori* analysis, it comes out that the majority of the 2000 geometries of the database involves core-core interactions together with core-chain ones, but only in minor part chain-chain interactions. Some T-shape configurations make also part of the database, but in these cases it is only the methyl terminal group to explore the other monomer surface (core and alkylic regions). This non exhaustive sampling might have led to an overestimation of the energy (and consequently over stabilization) of face-to-face configurations with respects to some other geometries which are populated in experimental bulk phases, but that are not included in the reference database. For these reasons including in the database new geometries in which alkylic chains of molecule A interact with the ones of B should allow obtaining a more accurate model of HAB.

4. lack of full atomistic details due to the UA simplification.

   Previous applications of this FF protocol suggest that the long alkylic chains of HAB might be responsible for the failure in finding the nematic phase. The same protocol was employed, in fact, on 5CB in 2005 [121]. There, Cacelli *et al.* were able to predict the nematic-isotropic transition temperature between 300 and 310 K, in excellent agreement with an experimental value of $\sim$ 306 K. The model parameters were then extended to 6, 7 and 8CB [91] and for all members of the nCB series clearing temperatures were correctly reproduced within $\pm$10 K with respect to the experimental value. Encouraging results were also obtained for both static and dynamical properties, except for a systematic overestimate of the density ($\sim$6%). The same FF also led to the correct prediction of a smectic phase for 8CB [154]. In 2008 the same procedure was applied on 4-*n*-pentyloxy-4'-cyanobiphenyl (5OCB) [92] and the T_{NI} was located between 330 and 350 K, in agreement with the experimental value of 340 K. In both cases, nCB series and 5OCB, however, there was only one alkylic chain per molecule, whereas in HAB two tails are present. Consequently, issues related to conformational flexibility (and therefore to the rigid sampling of a flexible molecule) and to the delicate description of alkylic groups were probably less critical than in HAB.

Further investigations were thus addressed to find out whether the problem was a local minimum in the model PES or a non adequate sampling of the dimer PES or the united atom treatment of aliphatic chains.

3.2 Full atomistic approach, I (Lennard-Jones potential)

3.2.1 Full atomistic force field

Even if the common trend in MD simulations is to treat alkylic CH_2 and CH_3 groups as whole interacting sites [84, 85, 155, 89, 92, 93, 154], a higher degree of realism can be reached abandoning the UA approach to employ a full atomistic model [86, 87, 88, 90]. Within this model alkylic hydrogens are treated explicitly so that each of the 67 atoms of HAB becomes an interaction site (see Figure 3.1). As far as the intramolecular contribution to the FF

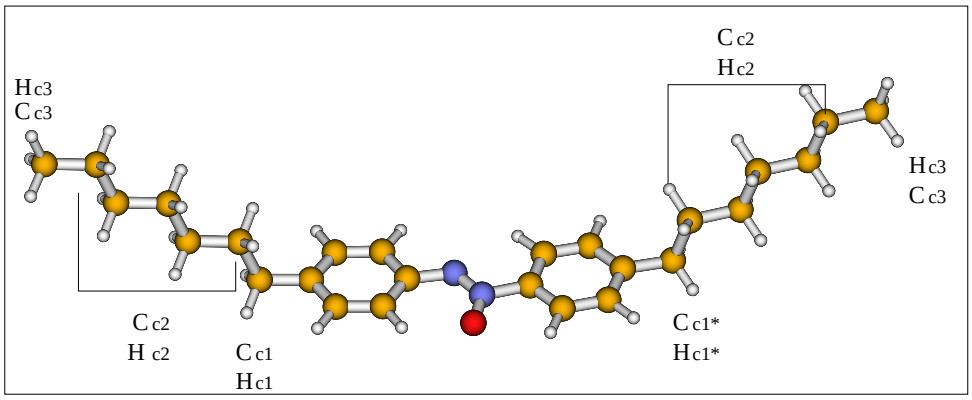

Figure 3.1: HAB: full atomistic (FA) model. All sites are labeled as in Figure 2.1. Alkylic hydrogens are labeled after the carbon atom they belong to, *i.e.* H_{c2} is an hydrogen bonded a C_{c2} site.

is concerned, exploding methylic and methylenic sites means that new internal coordinates appear: alkylic $C-H$ bond lengths, $\widehat{CHH}$ and $\widehat{HCH}$ angles as well as $H\widehat{CCH}$ and $C\widehat{CCH}$ dihedral angles. The fitting of Eq. 2.6 should be performed again to obtain the FA parameters of all the internal coordinates. However, the FA parameters describing internal coordinates of HAB core are not expected to be much different from those obtained for the UA model. It thus seemed a reasonable choice to maintain the UA equilibrium coordinate and force constant values for the core region and to simply add to the UA potential literature terms of stretching, bending and torsion involving the alkylic hydrogens. The extension from an UA model to a FA one was therefore straightforward. $H-C$ bonds were set to 1.09 Å and $\widehat{HCH}$ and $\widehat{CCH}$ bonding angles to 109.5° with k^b of ∼300 and ∼400 kJ/(mol·rad^2), respectively (values taken from [101, 116]). Finally, the torsional constants of the two terminal chain dihedral angles ($C\widehat{CCH}$) were derived on butane, relying on the parameter transferability already observed for inner $C\widehat{CCC}$ dihedrals (see Chapter 2). A torsional curve was thus

computed at DFT level (B3LYP/cc-pVDZ) on butane and then fitted with a three minima potential with $k^d = 6.40$ kJ/mol. The potential terms of the internal chain dihedrals, instead, were maintained the same as in the UA description, which means that the torsional energy for rotation around a $C-C$ bonds is totally accounted for in $C\widehat{CCC}$ terms, instead of being split up into three different contributions (namely $C\widehat{CCH}$, $H\widehat{CCH}$ and $C\widehat{CCC}$).

The intermolecular contribution to the FF was much more involving. Four new kinds of interacting sites were to be added: one for the hydrogens bonded to methylic carbons (H_{c3}), one for the methylenic hydrogens bonded to C_{c2} sites (H_{c2}) and one for those bonded to C_{c1} and C_{c1*} (H_{c1} and H_{c1*}). Atoms with the same label (see Figure 3.1) are considered equivalent and possess identical parameters. The number of intermolecular parameters in the model potential, E^{inter}, increases from the previous 63 (21*3) to 75 (25*3) because each new interacting site contributes with a triplet of parameters $< \sigma, \epsilon, q >$. This increase of the intermolecular parameters should lead to a better description of the dimer PES: the more parameters the model potential E^{inter} (Eq. 2.9) has, the greater its flexibility is and, consequently, the better is the matching of the two surfaces.

Many FA sets were investigated, changing the chosen starting parameters and the variability ranges applied to them. All sets were derived with the fitting procedure seen in Section 2.1.3, through the minimization of the difference between QM energy data and model analogous quantities, with the only difference that the sums of Eq. 2.10 ran on all the 67 atoms of HAB. However, the database of intermolecular energies was the same as for the UA approach, consequently the FA model function E^{inter} explores the same configuration phase space visited by the UA approach. These FA sets have standard deviations of 2.0 - 3.0 kJ/mol (the UA parameter set had a standard deviation of 2.48 kJ/mol) and they were all checked in preliminary MD runs: unfortunately, none of them was able to give a stable nematic phase.

As said in the Section 3.1, an *a posteriori* analysis of the database of dimer geometries reveals that chain-chain interactions have not been widely sampled. The majority of configurations, in fact, involves only core-core or chain-core energies. This insufficient sampling might have led to a poor description of chain-chain interactions. For this reason a further test was performed, describing C_{c2}, C_{c3}, H_{c2} and H_{c3} sites with OPLS [100] parameters. OPLS parameters, in fact, are empirical sets for computational simulations, derived to reproduce bulk experimental properties and in which three-bodies effects are therefore accounted for inherently. As all other empirical sets, OPLS has not a general validity: the set is tailored on a specific group of molecules (such as alkanes or aromatic molecules) and the more the molecule

Intermolecular parameters

Site	ϵ (kJ/mol)	σ (Å)	q (e)	Site	ϵ (kJ/mol)	σ (Å)	q (e)
C_{c1}	0.063	4.30	0.272	C_{c1*}	3.512	3.37	-0.009
C_1	5.230	2.47	-0.367	C_{n1}	0.053	2.21	-0.050
C_2	0.301	3.51	-0.043	C_{n2}	0.033	4.27	-0.066
C_3	0.652	3.46	-0.043	C_{n3}	0.751	3.30	-0.126
C_4	4.245	2.01	0.098	C_{n4}	4.130	2.62	-0.047
H_2	0.028	2.39	0.082	H_{n2}	0.074	2.00	0.119
H_3	0.021	2.31	0.048	H_{n3}	0.101	2.09	0.093
N	0.568	3.13	-0.374	$H_{c1(c1*)}$	0.021	2.30	0.120
N_O	0.040	3.64	0.729	H_{c2}	0.021	2.38	0.060
O	0.839	2.74	-0.428	H_{c3}	0.023	2.42	0.060
C_{c2}	0.139	3.50	-0.120	C_{c3}	0.603	3.50	-0.180

Table 3.1: FA-HAB: optimized intermolecular parameters for a 12-6 Lennard-Jones and Coulomb potential.

under study is similar to those used in the OPLS training set, the more the set is suitable for that molecule. In other words, the parameter transferability is granted only within similar molecules. OPLS all atom parameters for aliphatic chains were derived by Jorgensen *et al.* in 1994 [100] and they were used here for the σ of C_{c2} and C_{c3} atoms ($\sigma = 3.5$ Å). As far as electronic charges are concerned, in the previous approach C_{c2} groups were assumed chargeless, in order to allow a straightforward extension of the FF from HAB to higher homologues: here, C_{c2} and C_{c3} groups were described with OPLS charges of -0.12 and -0.18 e, respectively and their hydrogens with a charge of 0.06 e, so to respect electroneutrality.

With these assigned charges, all σ (except for the ones of C_{c2} and C_{c3}) and ϵ were optimized through the fitting procedure of Eq. 2.9 and the resulting parameters are reported in Table 3.1. The standard deviation of the fitting is 3.008 kJ/mol, 0.52 kJ/mol higher than that of the UA approach. In Figure 3.2 the same QM data of Figure 2.6 are reported and the new FA fitted energies are compared with the previous UA model. The striking feature is that the explicit hydrogen approach describes the parallel curve considerably worse than the UA model, while in the other three cases the accuracy on the QM data reproduction are comparable. However, these are only four among the many possible curves and they are far from sufficient to gauge the quality of the new fit. For example, exactly the opposite happens

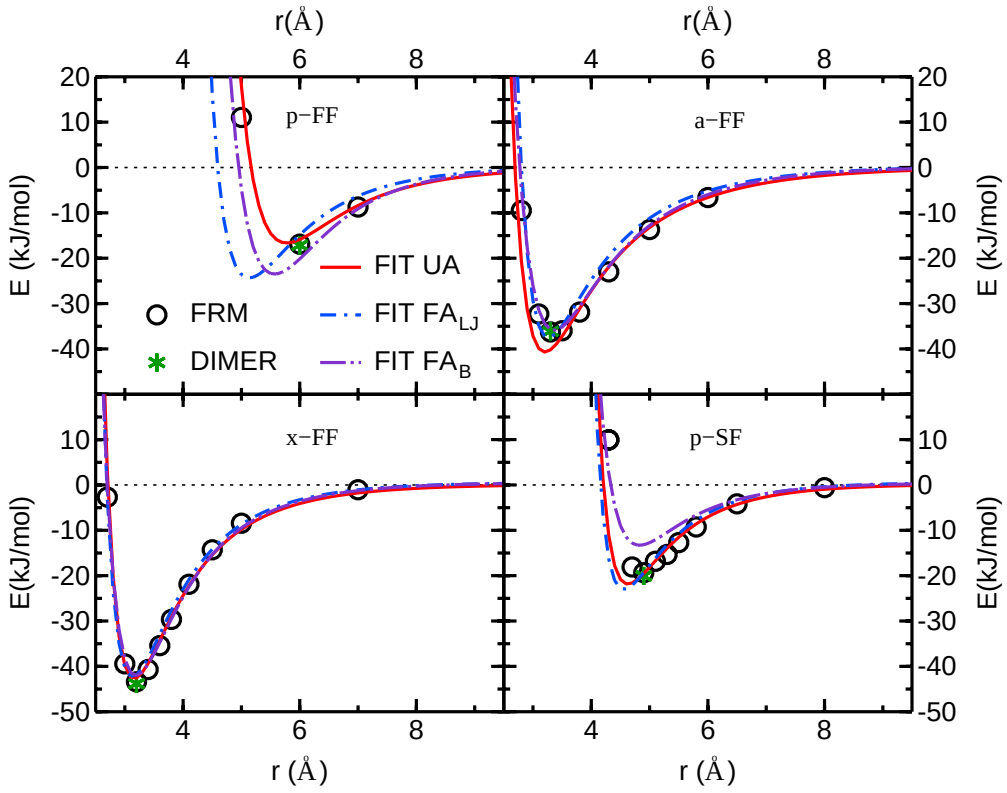

Figure 3.2: FA-HAB: computed and fitted energy curves for the same geometrical arrangement of Figure 2.6: parallel (p-FF), antiparallel (a-FF), cross (x-FF) and side-face (p-SF). Black circles represent the FRM energies and the green point marked 'DIMER' shows the interaction energy of the dimer, computed *ab initio* for the whole molecules (no FRM, see Chapter 2). Lines are fitted energies. The red solid one is the UA potential curve of Chapter 2, reported for comparison. The dot-dashed curves are FA fittings employing a 12-6 Lennard-Jones (blue) and a Buckingham potential function (violet) (see Section 2.2 and 2.3).

in an antiparallel arrangement slightly different from that of Figure 3.2. The QM data for a simple displacement of molecule B along $\hat{R}$ (no other shift applied) are shown in Figure 3.3. Here, it is the UA curve that largely overestimates the interaction energy while the FA model shows a much better matching to the QM data.

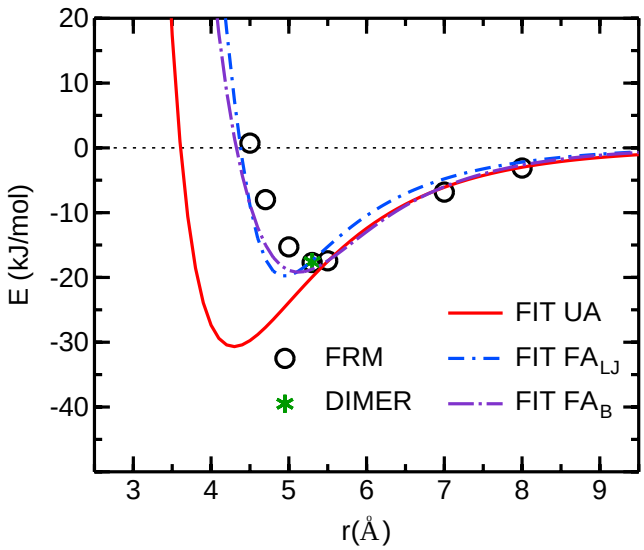

Figure 3.3: FA-HAB: computed and fitted energy curves for an antiparallel geometrical arrangement. It is the same geometry reported in Figure 2.6 and 3.2, but this time no shift on $\hat{u}_{\perp}$ has been applied on molecule B. Black circles represent the FRM energies and the green point marked 'DIMER' shows the interaction energy of the dimer, computed *ab initio* for the *whole* molecules (no FRM, see Chapter 2). The lines are fitted energies. The red solid one is the UA potential curve of Chapter 2, here reported for comparison. The dot-dashed curves are FA fittings employing a 12-6 Lennard-Jones (blue) and a Buckingham potential function (violet) (see Section 2.2 and 2.3).

3.2.2 MD simulations

Computational details

The above FA force field was employed for MD simulations carried out with the GROMACS 4 [10] package on a cubic systems of 400 and 1000 HAB molecules. In all runs bond lengths were kept fixed at their equilibrium value using SHAKE algorithm [143], with a timestep of 1.5 fs. Charge-charge long range forces were treated with the particle mesh Ewald method [144, 145], with a fourth order spline interpolation (Fourier spacing = 0.18 nm), while the short range interactions were truncated at $R_c = 11$ Å. In the NPT ensemble, temperature and pressure were kept constant using the coupling scheme of Nose-Hoover (coupling constant of 0.5 ps) [156, 157] and Parrinello-Rahman (coupling constant of 1.6 ps), respectively [158]. Standard corrections for energy and virial were employed [112].

Bulk simulations: FA-HAB, Lennard-Jones potential

As a first test of the mesogenic behavior of the FA model of HAB with intermolecular interactions modeled with a 12-6 Lennard-Jones potential and a Coulomb contribution, a phase of 400 molecules (26800 interaction sites) with orientational order ($P_2 = 0.6$), but positionally disordered ($\tau = 0.2$) was built up applying an electric field. The field was then switched off and the relaxation of the system was studied at different temperatures, from 320 K to 350 K for several ns to find out whether an explicit description of hydrogens was sufficient to lead to a stable nematic bulk. P_2 and τ trends for all temperatures are reported in Figure 3.4.
At 320 K HAB was smectic: after an initial decrease to 0.4, P_2 raised up to 0.6, whilst τ reached 0.5. 40 ns were considered sufficient to ascertain the formation of positional order in the system and the simulation was stopped.
HAB behavior at 330 K confirmed our assumption: P_2 and τ values above 0.9 and 0.8 in $\sim$ 60 ns pointed out at an extremely defined layering of molecules. This high value of τ is quite unexpected for a smectic A phase, where it oscillates normally around 0.5, as it can be seen for example in 4-n-octyl-4'-cyanobiphenyl [91]. The run was stopped after more than 60 ns and the resulting phase had a density of 0.984 g/cm^3, higher than that of the UA description at the same temperature (0.965 g/cm^3). The error with respect to the experimental value of the density (0.97 g/cm^3) is only 1.44%, but the inter-layer distance of $\sim$ 20.5 Å is still significantly smaller than the experimental value of 28.9 Å [50]. Moreover, the orientation of the director associated to P_2 does not coincide with the normal to the layers, but a tilt

angle was detected. These features suggest that, as in the UA approach, the model system does not arrange itself in a smectic A phase.

The evolution of the starting pseudo-nematic was also followed at 340 K and 350 K for a few tens of ns. In both cases the nematic phase melted to an isotropic phase and the orientational order parameter collapsed to 0.2. The 340 K system had a density of 0.954 g/cm^3 and this value is comparable with the UA analogous of 0.939 g/cm^3. Moreover, no nematic phase was

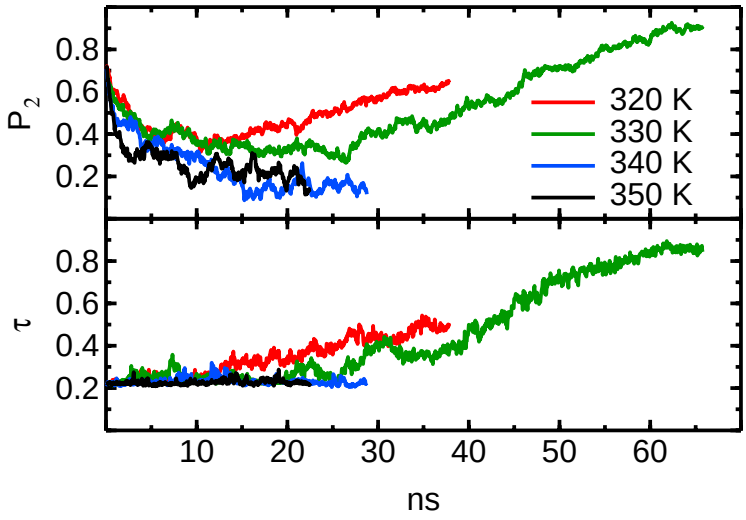

Figure 3.4: FA-HAB: MD simulations at different temperature with a FA model. Top panel: orientational order parameter, P_2; bottom panel: positional order parameter, τ.

detected; this FA model seems suffering from all the limits of the UA approach. However, the experimental range of existence of the nematic phase is 327 - 342 K, only ∼15 K, and its detection is a difficult challenge, also due to the unavoidable fluctuations. Due to this narrow range of existence, simulations would benefit from an enlargement of the system size: the bigger the number of molecules the smaller are the fluctuations of observable quantities. To rule out a possible dependence of the nematic stability on the system size a brief study with a thousand molecules was thus undertaken. With 67000 interaction sites two temperatures, 325 and 330 K, were investigated for more than ∼ 80 ns, starting from an isotropic phase. Unfortunately, neither this attempt was successful. At 330 K the system was isotropic, while a spontaneous reorganization into a smectic phase was observed at 325 K, Figure 3.5. The computational resources available did not allow for a further enlargement, and investigations were thus led to explore other possible causes for the missing of the nematic phase.

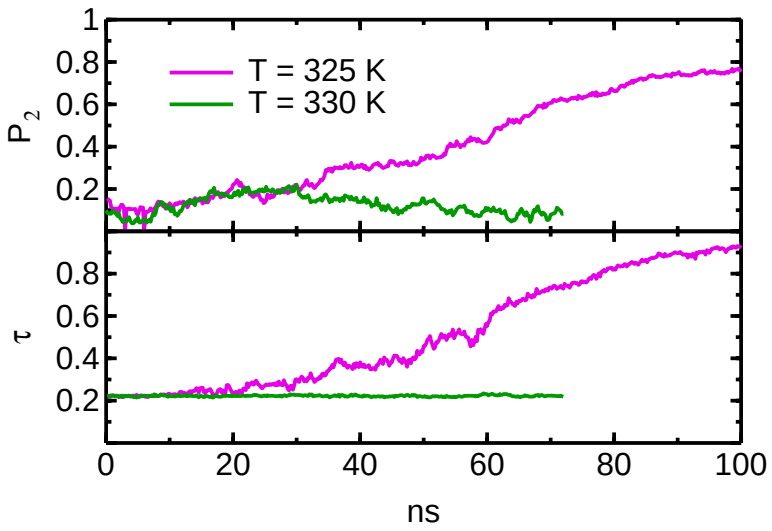

Figure 3.5: FA-HAB: MD simulations at different temperatures with an all atom model. The employed intermolecular potential is the 12-6 Lennard-Jones and the system is made up of 1000 molecules (67000 interaction sites).

3.3 Full atomistic approach, II (Buckingham potential)

Beyond a full atomistic description of HAB molecule, a higher degree of flexibility on E^{inter}, with respect of the UA Lennard-Jones approach, can be reached using a different model function, such as Buckingham potential [159]. This is a pair potential made up of two terms responsible for repulsion and attraction, respectively. As in the Lennard-Jones potential the attractive term is proportional to $1/r^6$, where r is the site - site distance. On the contrary, the exchange repulsion that originates from the Pauli exclusion principle is described by a more realistic exponential function of distance, instead of the inverse twelfth power used by the Lennard-Jones potential. Buckingham potential has thus the following form:

$$E_{ij}^{B} = A_{ij}e^{-B_{ij}r_{ij}} - \frac{C_{ij}}{r_{ij}^{6}} \tag{3.1}$$

where i and j are the interacting sites of two different molecules, r_{ij} is the site-site distance and A_{ij}, B_{ij} and C_{ij} are the interaction parameters. These are obtained with the following combination rules:

$$A_{ij} = \sqrt{A_i A_j} \qquad B_{ij} = \frac{2}{1/B_i + 1/B_j} \qquad C_{ij} = \sqrt{C_i C_j} \tag{3.2}$$

Buckingham potential has a clear advantage with respect of the Lennard-Jones one: each pair of interacting sites is described with three parameters (A, B and C) instead of two (σ,

ϵ). In the HAB case this means going from 63 (UA) or 75 (FA, I) parameters to 100. This should allow a better matching of the E^{inter}, model potential, to the PES dimer.

A new fitting was thus performed, as explained in Section 2.1, on the same energy database employed before, with the difference that E_k^{inter} of Eq. 2.10 has now the following form:

$$E_k^{inter} = \sum_{i=1}^{N_{sites}} \sum_{j=1}^{N_{sites}} [E_{ij}^B + E_{ij}^{Coul}]_k \tag{3.3}$$

where E_{ij}^B is the above Buckingham potential. All parameters were accurately checked to prevent "Buckingham catastrophe" in the range 2 - 12 Å. Buckingham potential, in fact, goes to $-\infty$ for $r \to 0$ (see Eq. 3.1), meaning that an atom pair is allowed to move into very close contact where the short range potential is unphysical. As for the first FA approach, many sets were derived and checked in preliminary MD runs. Among them only one is reported as a way of example (see Table 3.2). This set has a standard deviation of 1.75 kJ/mol, more than one kJ/mol lower with respect of the UA and FA-LJ ones (2.48 and 3.00 kJ/mol, respectively). In Figure 3.2 and 3.3 Buckingham curves for some configurations are also shown, in violet. In Figure 3.2, as far as the parallel arrangement is concerned, it can be seen that the Buckingham agreement on QM data is intermediate between that of the UA and FA approach. The three fittings perform comparatively both in the antiparallel and cross geometries, while Buckingham performs a little worse than the other two in the parallel side-face arrangement. The improvement in the PES matching can be appreciated, for example, in the antiparallel geometry of Figure 3.3.

In order to investigate the missing nematic phase, the same approach of Section 2.2 and 3.2 was used (and the same computational details of Section 3.2 are still valid). A system of 400 molecules was ordered in a pseudo-nematic phase and its relaxation was followed

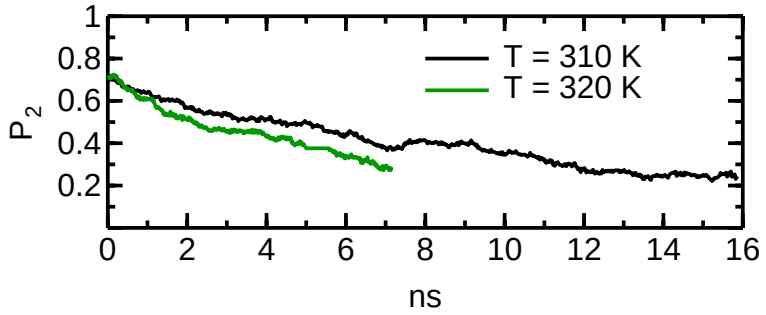

Figure 3.6: FA-HAB: MD simulations at different temperatures with an all atom model. The employed E^{inter} model is the Buckingham potential. The system is made up of 400 molecules (26800 interaction sites).

Intermolecular parameters

Site	A	B	C	q	Site	A	B	C	q
C_{c1}	353888.2	3.67	2617.9	0.172	C_{c1*}	103716.6	3.21	3716.6	0.029
C_1	713417.6	4.72	662.7	-0.304	C_{n1}	227917.8	5.55	114.2	-0.040
C_2	107415.8	3.17	2187.8	-0.046	C_{n2}	113078.3	3.49	176.1	-0.090
C_3	1104486.9	3.90	6995.2	-0.009	C_{n3}	73678.9	3.86	493.8	-0.133
C_4	1663947.1	5.08	50.6	0.102	C_{n4}	315420.8	4.39	456.2	-0.114
H_2	22180.6	4.38	107.1	0.051	H_{n2}	1500.9	3.95	31.8	0.064
H_3	2365.2	3.26	38.9	0.023	H_{n3}	1260.7	3.54	50.6	0.176
N	46834.9	3.12	2159.8	-0.368	$H_{c1(*)}$	1568.2	4.00	17.2	-0.005
N_O	19166.5	2.98	2540.5	0.727	H_{c2}	513.1	3.56	0.0	0.000
O	184674.2	4.02	911.3	-0.404	H_{c3}	1294.6	3.63	1.3	0.000
C_{c2}	1207892.4	3.89	4423.3	0.000	C_{c3}	132633.5	4.29	1180.8	0.074

Table 3.2: FA-HAB: optimized Buckingham intermolecular parameters. Units are the following: A (kJ/mol), B (A^{-1}) and C (A^6kJ/mol).

for some tens of ns at different temperatures. Once again the search revealed baffling: the pseudo-nematic orientational order collapsed even at 310 K, see Figure 3.6. Indeed the chosen parameter set was not the right one for HAB, notwithstanding the low standard deviation.

3.4 Conclusions

In this and in the previous Chapter the same protocol for FF parameterization has been presented, applied to different models for HAB molecule. Even if capable of good results, none of the models revealed sufficient accuracy to reproduce correctly the whole phase diagram of this mesogenic molecule and its nematic phase was never observed in simulation. The employed *ab initio* procedure seems affected by some serious limits, such as the parameter set redundancy and the lack of a systematic strategy to an adequate sampling of the dimer configurational phase space. In the case of HAB, many attempts were led to overcome these limits tuning some of the *ab initio* parameters in a way to reproduce experimental quantities in simulation, but this can not be a satisfactory solution. First of all this procedure is considerably lengthy, because it is practically impossible to evaluate how modifications on the parameters will propagate on bulk properties beforehand and many explorative simulations are required to compare the results with experimental data. Second, and most important, it is not an *a priori* procedure: experimental data are required for the tuning of the parameters with the natural consequence that the FF protocol looses its general validity (because it can be applied only in presence of experimental data) together with its pure *ab initio* and predictive nature.

In the following Chapter a different FF tailoring protocol will be explored, where intermolecular parameters are iteratively fitted on an increasing database of dimer interaction energies extracted from an MD bulk phase.

CHAPTER

4

INTERMOLECULAR FORCE FIELD PARAMETRIZATION, A NOVEL APPROACH

A new FF parametrization route is proposed. The novelty of this approach with respect of that of Chapter 2 and 3 is the way the "reference" set of dimer configurations is constructed. This is the set made up of chosen geometries whose energy is QM computed and used to parameterize the function E^{inter}. In Chapter 2 and 3 these configurations were *a priori* chosen, now they are extracted from short MD runs. In this way a better exploration of the dimer PES and of the monomer conformational space should be achieved. The intermolecular parameters are iteratively improved by fitting E^{inter} on the QM energies of the increasing database of dimer geometries extracted from the MD trajectory.

The strategy for the dimer selection has been coded in a Fortran program, named PICKY. A first test on a simple molecule, toluene, is presented as a way of example, but the method is general and it can be applied to whatever molecule. Work is currently in progress to improve and test the code.

4.1 Common problems in FF tailored parameterizations

The construction of accurate potentials for MD simulations is a challenging task as it is demonstrated by HAB (see Figure 1.1) study in Chapters 2 and 3. The adopted protocol consisted of two main steps for both the inter and intramolecular part of the potential. At first, there was the exploration with suitable QM methods of the PES of the molecule dimer and of the monomer conformational space of flexible dihedrals. Then, the QM interaction

energies of the dimers were fitted with a model potential E^{inter} and the torsional profiles, together with the energy of the full optimized geometry, were fitted with the model function E^{intra}. In this way the parameters of the FF, equilibrium values and force constants of internal coordinates on one side and interaction parameters (q, σ, ϵ or q, A, B, C) on the other, were derived.

Potentials obtained in this way have a strong *ab initio* nature and they could be used for realistic predictions of the properties of new materials. However, in some cases this predictive connotation is lost or weakened (as for HAB) because it becomes necessary to tune one or more parameters on experimental properties to improve the results. Strategies to avoid this inconvenience are fundamental to preserve unaltered all potentialities of the method and our studies on HAB have put in evidence some limits of the protocol, mainly connected to the way the selection of dimer geometries was operated. On this subject, three issues reveal to be critical.

The first is how to choose the geometries whose energy will be QM computed. This database should include at least those configurations which are alike to be populated in bulk phases, because the goal of the FF parameterization is indeed to reproduce bulk behavior. However, an *a priori* understanding of which configurations are needed to obtain a "reference" set of geometries that is representative of the real sample is not always an intuitive task. The problem concerns with the intermolecular arrangements different from the ones of the reference set, because they can be populated in the MD simulated sample, but inaccuracies on their predicted energies may affect bulk properties.

The second consideration concerns with the frozen monomer sampling. The exploration of the dimer PES was performed by changing the relative position of molecule B with respect of molecule A with movements along $\hat{u_\perp}$, $\hat{R}$, $\hat{u_\parallel}$, and rotations of α, β and γ (see Figure 2.4). The internal geometries of both A and B monomers, instead, were frozen in their optimized conformations. However, this is a rather drastic approximation. It can happen that the equilibrium conformation of A and B molecules in a dimer is different from that of the isolated molecules, because the presence of the other molecule can induce conformational changes in the more flexible degrees of freedom. Moreover, the kinetic energy of the atoms in the MD runs allows the system to explore portions of the PES not necessarily close to local PES minima, so that this constraint should be removed.

Finally, mapping the dimer PES onto a finite grid of points brings in the problem of the redundancy of the intermolecular parameter sets. The fewer points are considered and the less

the behavior of the model function E^{inter} is guided: a good fitting will be anyone performing satisfactorily at the grid points, no matter its value at all other points. Intuitively, the fewer points are sampled and the more parameter sets will be able to describe it within a certain standard deviation. These sets, however, can result in very different potentials in those non explored regions, with drastic consequences at run time. Therefore, the choice of the "right" set of parameters among many others is fundamental for the success of the simulation, but, at the same time it remains a tricky problem as no objective criteria can guide it. Clearly, an increase in the QM database would cut down this redundancy, but QM data can be very expensive from a computational point of view and such an extension is not always feasible. On the contrary, strategies could be adopted to improve the sampling, that is the quality of the explored model PES.

In summary, there are two main limits in the previously proposed route to intermolecular FF parameterization: the absence of a systematic strategy for the choice of dimer geometries and the rigid sampling.

4.2 Interatomic potential from *ab initio* data and MD simulations

Among the many attempts of obtaining intermolecular FF parameters from first principles results was that of Ercolessi and Adams in 1994 [160]. The numerical engine of their method is based on matching as closely as possible the first principles forces with those predicted from the classical potentials, and for this reason it was named as the force-matching (FM) method. After their first application to derive a glue potential for aluminium [160], this method was successfully applied to derive the force field for several systems [161, 162, 163] and its algorithm was coded in many softwares [164, 165]. Recently, in 2008, Akin-Ojo *et al.* proposed the adaptive energy force-matching method (AFM), a modification of the original FM method in which the parameters to reproduce atomic forces obtained from *ab initio* simulations in the condensed phase are iteratively improved [111].

Following their suggestion, a strategy different from that of Chapter 2 and 3 was entailed to overcome the problems seen in the previous Section. The basic idea is the following: sampling dimer configurations from MD trajectories, computing their *ab initio* energies and using them to fit E^{inter}, iteratively. Once chosen the internal FF (which stays the same throughout the whole process), the main steps of the procedure are illustrated in Figure 4.1

and are the following:

1. The MD run.

   An initial intermolecular FF is chosen to start the simulation (for example a set of q, σ, ϵ). It can be a general FF (such as OPLS [101], AMBER [103], CHARMM [7]), or a more specific one obtained in some other ways. It is a first guess and it does not need to be accurate. The simulation is run and some dimer configurations are extracted from the MD trajectory with criteria that will be discussed later on.

2. The QM computation.

   Interaction energies of the selected dimer configurations are *ab initio* computed at a sufficient level of theory (for example with suitable post-Hartree–Fock methods to correctly account for dispersion energies).

3. The Fitting.

   On one side there is the database of QM intermolecular energies and on the other there are the predicted energies for the same geometries by the current FF. A merit function is constructed, which contains the difference of these two quantities. From its minimization a new set of parameters (q', σ', ϵ') is obtained. The procedure goes on iteratively, until a convergence threshold on the value of the parameters is reached.

This procedure naturally addresses two of the three issues described in Section 4.1. The geometries of A and B monomers, in fact, are not any more rigid. They are extracted from an MD trajectory and as such they can be found in any internal geometry consistent with the simulation temperature and the employed intramolecular FF. This implies that E^{inter} is not derived from fitting a six-dimensional grid of points, but from a space which has the same dimensionality of the dimer PES and that a dynamical coupling between the internal and intermolecular coordinates is introduced.

Moreover, as parameters for condensed phases are looked for, the sampled configurational space should include at least those geometries alike to be found in bulk. This means that it is not important to sample homogeneously the whole configurational space, but, on the contrary, a sort of importance sampling is performed extracting the configurations from a simulated bulk. According to the quality of the guess FF, more or less important regions will be explored. If the initial parameter set is a poor one, it is probable that unimportant points will be chosen in the first iterations. On the contrary, if the set is a good minimum more

populated regions will be sampled. At any rates, along the iterations the FF improves and with it the importance of the visited space. Hopefully, there will not be any need of tuning the parameters on experimental properties and the *a priori* nature of the method will be thus preserved.

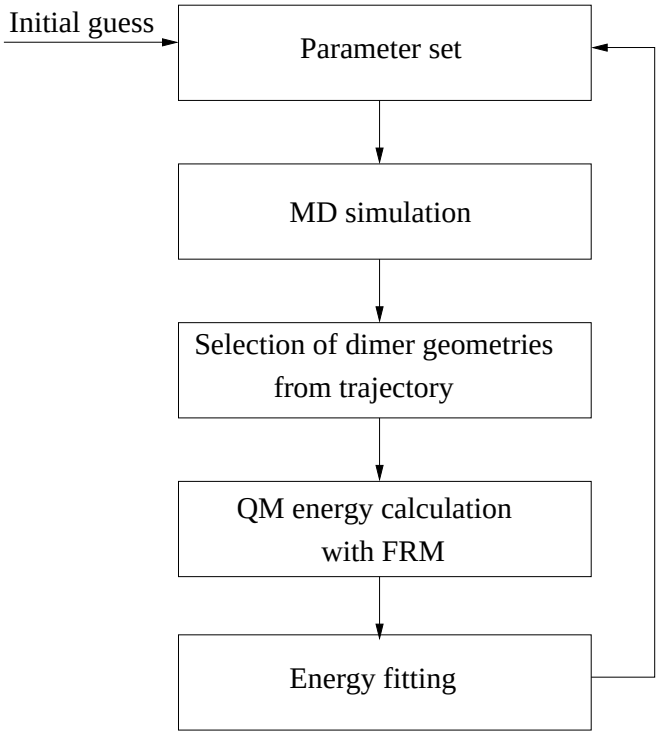

Figure 4.1: FF parametrization approach based on QM data and MD simulations: main steps of the method are shown.

4.3 The role of FRM

The FRM method (Section 2.1, [25]) has in the new approach the same fundamental importance as before. Once more, intermolecular energies of target dimers are computed with this method which allows us to recover E^{inter} as a suitable combination of the interaction energies of the smaller fragments making up monomers A and B. However, FRM does not provide only the total $A \cdots B$ interaction energy, but also the fragment-fragment contributions. These data have a clear physical meaning and they might help in cutting down the redundancy of the sets of intermolecular parameters. According to Eq. 2.9, the best set of parameters is the one that minimizes the difference between the QM energy and the model potential E^{inter}, no

matter how the various site-site interactions concur to it. The k^{th} geometry can be considered as a way of example. Its model interaction energy is a sum of pairwise terms and it has the following form:

$$E_k^{inter} = \sum_{i=1}^{N_{sites}} \sum_{j=1}^{N_{sites}} [E_{ij}^{LJ/B/\dots} + E_{ij}^{Coul}]_k \tag{4.1}$$

where LJ and B refer to a Lennard-Jones or Buckingham potential, and i and j are the interacting sites on monomer A and B, respectively. In the fitting, a suitable variability range is applied on each parameter to help absolute minimum research and to guide the minimization process towards physically sound solutions. Apart from that, however, there is nothing else to control the contributions to the total E^{inter} coming from the different molecular portions (to which i and j belong).

A molecule of 5CB can be considered. This has a rigid cyanophenyl portion connected to a five carbon alkylic chain. The interaction energy of a molecule A with a molecule B can be seen as made up of the interaction of the cyanophenyl portion of A(B) with the cyanophenyl and alkylic portions of B(A), in the following way:

$$\begin{aligned} &E(CNC_6H_4C_5H_{11} \cdots CNC_6H_4C_5H_{11}) \rightarrow \\ &\rightarrow E(CNC_6H_4 \cdots CNC_6H_4) + E(CNC_6H_4 \cdots C_5H_{11}) + \\ &\quad E(C_5H_{11} \cdots CNC_6H_4) + E(C_5H_{11} \cdots C_5H_{11}) \end{aligned} \tag{4.2}$$

These terms are very similar to possible FRM fragments, with the only difference that within the FRM method the valence of all moieties is saturated with intruder groups. The FRM fragmentation scheme of 5CB using H atoms as intruders would be the following:

$$CNC_6H_4C_5H_{11} \rightarrow CNC_6H_5 + C_5H_{12} - H_2$$

and the interaction energy of a dimer:

$$\begin{aligned} &E((CNC_6H_5 + C_5H_{12} - H_2) \cdots (CNC_6H_5 + C_5H_{12} - H_2)) \rightarrow \\ &\rightarrow \quad \underline{E(CNC_6H_5 \cdots CNC_6H_5)} + \underline{E(CNC_6H_5 \cdots C_5H_{12})} - E(CNC_6H_5 \cdots H_2) + \\ &\quad \underline{E(C_5H_{12} \cdots CNC_6H_5)} + \underline{E(C_5H_{12} \cdots C_5H_{12})} - E(C_5H_{12} \cdots H_2) - \\ &\quad E(H_2 \cdots CNC_6H_5) - E(H_2 \cdots C_5H_{12}) + E(H_2 \cdots H_2) \end{aligned} \tag{4.3}$$

In the last equation the underlined terms correspond to the four quantities of Eq. 4.2, apart for the H saturation. From this picture it may be required that the best parameter set is

the one able to minimize the differences $(U^{FRM} - E^{inter})^2$ of Eq. 2.9, but also to distribute correctly the total interaction energy between the different molecular portions. Consequently, FRM fragment-fragment energies may be included in the database of QM energies and used as useful guidelines to the PES via Eq. 2.9.

In Figure 4.2 a dimer of HAB is reported in a configuration in which a great part of the interaction energy arises from a favorable chain-chain disposition. Referring to Figure 2.4 the configuration is obtained with a 3.5, -12.7 and 15.0 Å shift on $\hat{u}_\perp$, $\hat{R}$ and $\hat{u}_\parallel$, respectively, and with $\alpha = 180°$. The geometry shown in the bottom right panel is obtained moving away molecule B along the direction shown by the dotted arrow in the bottom left panel. The FRM involved energy is also shown in Figure 4.2, where both the total interaction energy (green plus) and the chain-chain contribution (black circles) are reported. The blue dot-dashed curve is the potential energy predicted by the FA-LJ potential of Section 3.2 and the solid one is the portion of the same energy coming from interaction between alkylic sites, only. Analogous quantities are also presented for the Buckingham potential of Section 3.3. The four curves are predictions, as these geometries do not belong to the energy database used in the fittings. The agreement between the QM and model energy is quite satisfactory in the attractive range, less in the repulsive region. Moreover, it can be noted that the chain-chain LJ energy nearly coincides with the total one, as reasonable. As for the Buckingham potential, instead, two distinct curves can be seen. This means that a different partition of E^{inter} has occurred on the pairs of interacting sites.

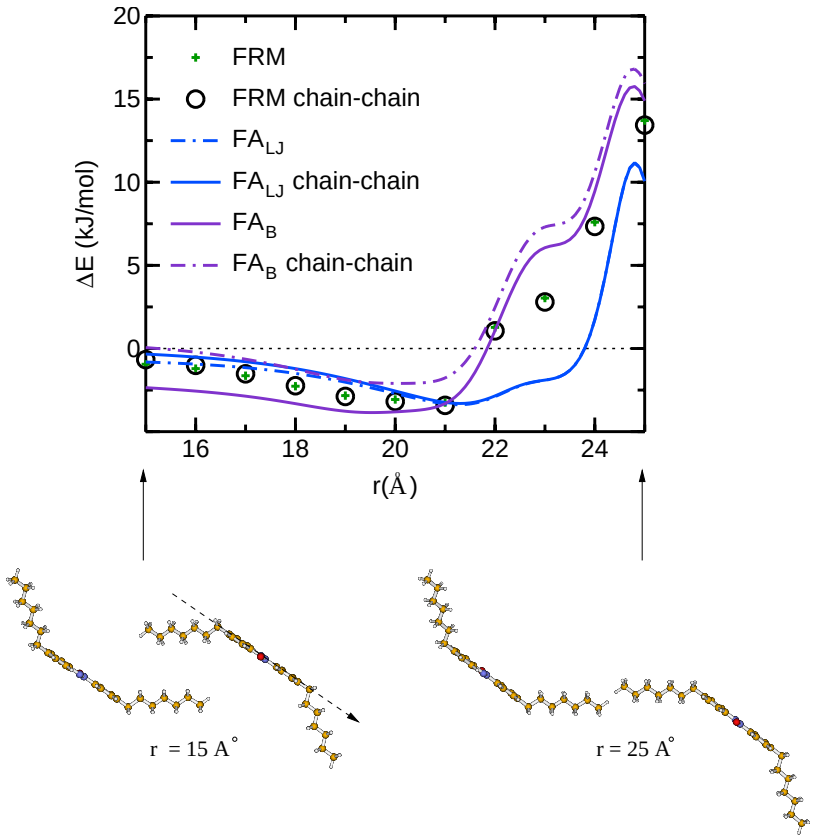

Figure 4.2: Bottom panel: a dimer of HAB. The configuration on the right is obtained moving molecule B of HAB dimer along the direction shown by the dotted arrow. Top panel: interaction energy curves for the displacement of molecule B are shown. Symbols are interaction energies computed with FRM: green plus and black circles are total and chain-chain interaction energies, respectively. Blue (FA-LJ) and violet (FA-B) curves are obtained with the potentials of Chapter 3. Dashed and solid curves are total and chain-chain interaction energies, respectively. r refers to the shift along $\hat{u}_{\parallel}$ (see text and Figure 2.4).

4.4 PICKY, a sampling code

Using MD configurations rules out the problem of a rigid sampling and it should help at an importance selection of bulk geometries, which is fundamental for the derivation of a reliable FF for condensed phases. However, how to choose a dimer geometry instead of another from an MD trajectory remains a critical step. At this purpose, we have coded a systematic strategy in a Fortran program, named PICKY. This program reads the MD trajectory and FF files (MOSCITO or GROMACS format) and it selects a certain number of dimers satisfying some conditions from the final snapshot of the simulation. The code is totally general and it can be applied both to rigid and flexible molecules, as the FF protocol, itself. PICKY is now a beta version and work is in progress to improve and assess the quality of its performances.

4.4.1 Selection criteria

It was said previously that, ideally, the best sampling is the one which explores the whole configurational space homogeneously. However, this is an unfeasible task. First of all because it can become extremely expensive from a computational point of view. Secondly, as we are looking for FFs to study condensed phases, it is useless to choose, for example, those configurations which do not occur in real bulk. There is a sort of hierarchy of importance in the different geometries: some are more fundamental than others for the realism of the FF and sampling from an MD trajectory should apply this hierarchy naturally.
The idea of the strategy has two main aspects. The first is that when a dimer is extracted from the trajectory, a comparison with each of the already accepted dimers is performed to check if a dimer with very *similar* geometry was already included in the database. In fact, it would be pointless to include very similar configurations in the sample as it is more convenient to explore as much as possible the variety of the configurational space of the current MD trajectory. The second is connected to the improvement of the FF along the iterations. In the first runs, in fact, the quality of the selection (in terms of importance) depends on the quality of the initial guess of the FF. As the iterations go on, however, the MD is governed by more and more relevant potentials and more populated geometries are gradually added.

4.4.2 The Difference Index (DI)

The central idea of PICKY is that a dimer is accepted (i. e. included in the reference sample) only if it is sufficiently different from the others in the database and the difference index (DI) is the quantity that translates this concept into a mathematical quantity. This index ranges from 0 to 1 and refers to a pair of dimers. The more it approaches 1 and the less the two dimers have in common, while $DI = 0$ means the two dimer are identical.
At the moment, DI has been designed to compare two dimers of homologous molecules having a central rigid core and flexible lateral chains (the prototype of mesogens), but the constraints can be easily removed. DI has been thought as a combination of three contributions. The first refers to the reciprocal position of A and B cores within the dimer. The second accounts for the relative position of alkylic chains and the third compares the internal geometries of A and B monomers of the two dimers.

The descriptors chosen to evaluate the degree of difference between the cores of the two dimers are scalar products of the following form:

$$V = \left\| (\hat{V}_{iA} \cdot \hat{V}_{jB})_{k1} - (\hat{V}_{iA} \cdot \hat{V}_{jB})_{k2} \right\| \tag{4.4}$$

where $\hat{V}_{i(j)}$ is a chosen versor belonging to A or B molecule in the kth sampled configuration. For each monomer core four atoms are chosen to define a long and a short molecular axis whose versors are $\hat{L}_{A(B)}$ and $\hat{S}_{A(B)}$, respectively. A and B versors can be combined in scalar products to obtain the following quantities $\hat{L}_A \cdot \hat{L}_B$, $\hat{L}_A \cdot \hat{R}$, $\hat{L}_B \cdot \hat{R}$, $\hat{S}_A \cdot \hat{S}_B$, that taken together provide a synthetic description of the relative position of the two molecules, according to the invariance of the dimer for rotation and translation. Moreover two possibilities have to be studied in the comparison of two dimers. The first is the one in which the first molecule (A) of dimer χ is compared to the first monomer (A) of dimer k and the second molecule (B) of χ to the second monomer (B) of k. The second case is the one in which the first molecule (A) of χ is compared to the second (B) of k and the second (B) of χ to the first (A) of k.
By way of example, let χ be the dimer under examination and the database of already accepted geometries have N_c configurations. χ is compared to each k ($k = 1, N_c$), in turn. As for DI$_{core}$, two quantities are computed. The first refers to the comparison of A$_\chi$ with A$_k$ and B$_\chi$ with B$_k$:

$$\begin{aligned} DI^k_{core} \;=\; & \frac{1}{8}\Big(\left\| (\hat{L}_A \cdot \hat{L}_B)_\chi - (\hat{L}_A \cdot \hat{L}_B)_k \right\| + \left\| (\hat{S}_A \cdot \hat{S}_B)_\chi - (\hat{S}_A \cdot \hat{S}_B)_k \right\| + \\ & \left\| (\hat{L}_A \cdot \hat{R})_\chi - (\hat{L}_A \cdot \hat{R})_k \right\| + \left\| (\hat{L}_B \cdot \hat{R})_\chi - (\hat{L}_B \cdot \hat{R})_k \right\| \Big) \end{aligned} \tag{4.5}$$

where $\hat{R}$ is the versor connecting the barycenter of A and B monomers.
The second quantity refers, instead, to the comparison of A_χ with B_k and B_χ with A_k. As the scalar product $\hat{L}_A \cdot \hat{L}_B$ and $\hat{S}_A \cdot \hat{S}_B$ are invariant, but $\hat{L}_A \cdot \hat{R}$ and $\hat{L}_B \cdot \hat{R}$ are not, we have:

$$\begin{aligned} DI^{*k}_{core} &= \frac{1}{8}\Big(\Big\|(\hat{L}_A \cdot \hat{L}_B)_\chi - (\hat{L}_B \cdot \hat{L}_A)_k\Big\| + \Big\|(\hat{S}_A \cdot \hat{S}_B)_\chi - (\hat{S}_B \cdot \hat{S}_A)_k\Big\| + \\ &\quad \Big\|(\hat{L}_A \cdot \hat{R})_\chi + (\hat{L}_B \cdot \hat{R})_k\Big\| + \Big\|(\hat{L}_B \cdot \hat{R})_\chi + (\hat{L}_A \cdot \hat{R})_k\Big\|\Big) \end{aligned} \tag{4.6}$$

where A and B of the second dimer have been exchanged.

As for DI_{chain}, the conformation of lateral chains can be accounted for defining two atoms at the extremes of each tail. The elongation of the chain is computed as the distance of these two atoms and it is compared with the analogous quantity in the k^{th} dimer. Scalar products of the chain versors $\hat{C}_i$ are also computed, as they provide useful information on the relative dispositions of alkylic groups. DI_{chain} has the following form:

$$DI^{k}_{chain} = \frac{1}{2 \cdot n_{ax}} \sum_{i=1}^{n_{ax}} \left(\frac{1}{2} \Big\|(\hat{C}_{iA} \cdot \hat{C}_{iB})_\chi - (\hat{C}_{iA} \cdot \hat{C}_{iB})_k\Big\| + c \cdot \|(C_{iA} + C_{iB})_\chi - (C_{iA} + C_{iB})_k\| \right) \tag{4.7}$$

where n_{ax} is the number of chain axis, C_i is the elongation of the i^{th} chain axis and c is a suitable normalizing factor.

Finally, a third contribution to DI comes from the comparison of internal geometries. In this case, the similarity of the two dimers is ascertained comparing the value of all internal coordinates λ (bond lengths, angle bending and rigid dihedral angles) of A and B monomers of the current dimer with those of the accepted dimers, in turn.

$$DI^{k}_{intra} = \frac{c_{ic}}{2 \cdot n_{ic}} \sum_{\lambda=1}^{n_{ic}} (\|\lambda_{iA\chi} - \lambda_{iAk}\| + \|\lambda_{iB\chi} - \lambda_{iBk}\|) \tag{4.8}$$

where $\lambda_{iA\chi}$ means the i^{th} internal coordinate of monomer A in the geometry χ and c_{ic} is another normalizing factor. Following the above considerations, the following quantity has to be computed, as well:

$$DI^{*k}_{intra} = \frac{c_{ic}}{2 \cdot n_{ic}} \sum_{i=1}^{n_{ic}} (\|\lambda_{iA\chi} - \lambda_{iBk}\| + \|\lambda_{iB\chi} - \lambda_{iAk}\|) \tag{4.9}$$

The complete DI of dimers χ and k is therefore the minimum value between the two combinations of the above three contributions:

$$DI^k = Min \begin{cases} w_{core} DI^k_{core} + w_{chain} DI^k_{chain} + w_{intra} DI^k_{intra} \\ w_{core} DI^{*k}_{core} + w_{chain} DI^k_{chain} + w_{intra} DI^{*k}_{intra} \end{cases} \tag{4.10}$$

where w are weights that can have different values so to weight a contribution more than the others. The dimer χ is accepted if DI^k is above a threshold value for each k, because this

means that χ is sufficiently different from all k. The threshold value is chosen in input and it can be varied in the different iterations to obtain a more or less severe selection.
Apart from this, distance and energy constraints are also available in PICKY to customize the selection. Their definition takes place in the input file of the program, where the number of dimers to choose is indicated, together with the name of the files from where the code reads the trajectory and the FF, the atoms defining the long, short and chain axis, the FRM fragmentation scheme of the molecule and the requested level of theory for the QM computation of dimer energies. Of the selected dimers PICKY stores in separate files the geometry, so that visual inspection can be done, and descriptors, such as scalar products. Furthermore PICKY automatically prepares for each accepted geometry suitable GAUSSIAN 03 [119] input files for the QM calculation of the dimer interaction energy, if necessary, within FRM method.
By way of example here is the algorithm of PICKY at the j^{th} dimer selection:

1. Molecule A is chosen near the center of the simulation box

2. Interaction energies with all molecules within a radius R_{AB} around A are computed and an ordered list is created. On top of the list are the dimers (A and one of its neighbors) with minima interaction energies (attractive range).

3. The A B dimer with minimum interaction energy is chosen. If this energy falls in the range of acceptance selected in the input file the dimer moves up to the following step, otherwise another B is selected from the ordered list of step 2.

4. The Difference Index is computed between this dimer and each of those in the accepted database, in turn.

5. If the dimer is sufficiently different from all geometries in the database it is accepted and a new A is selected, going back to step 1. Otherwise the dimer is rejected and another B is chosen, going back to step 3.

The procedure goes on until a certain number of dimers is sampled. The same molecule can not be sampled twice in the same run, as to provide the largest possible variability of the sample. R_{AB} and the range of acceptance on the energy are useful to orient the sampling, for example, in repulsive regions instead of attractive ones. Finally, short MD runs at high temperature and/or pressure could be used to sample those regions of the dimer

PES which are less populated at room temperature, but that could be useful for an accurate determination of the contact distance parameters σ.

4.5 Preliminary application: toluene

The following is just a proof of concept as work is currently in progress to improve PICKY code. As a first test of PICKY performances, the new FF parameterization route was applied on toluene. This molecule seemed a good first benchmark as it does not possess any flexible alkylic chains. Therefore, the difference index between two dimers is made up of only two contributions:

$$DI = w_{core} DI_{core} + w_{intra} DI_{intra}$$

allowing a first, partial control of the code behavior.

Toluene was modeled full atomistic (see Figure 4.3) and the initial FF was derived as follows. As for the intramolecular contribution, toluene was fully optimized at DFT (B3LYP/cc-pVDZ) level and atomic charges as well as the intramolecular parameters of E^{intra} were derived as described in Section 2.1. As for the E^{inter} term of the FF (modeled as a 12-6 Lennard-Jones potential and a charge - charge contribution), instead, literature σ and ϵ intermolecular parameters were employed [166], scaled by +30% and -30%, respectively.

A simple cubic arrangement of 512 molecules was then created and equilibrated for a few ns at 298 K and atmospheric pressure with the MOSCITO package [142]. In all runs bond lengths were kept fixed at their equilibrium value using SHAKE algorithm [143] which allowed for using a timestep of 1.5 fs. Charge-charge long range forces were treated with the particle mesh Ewald method [144, 145], using a convergence parameter α of $5.36/2R_c$ and a fourth order spline interpolation, while the short range interactions were truncated at R_c= 10 Å , employing standard corrections for energy and virial [112]. Temperature and pressure were kept constant using the weak coupling scheme of Berendsen *et al.* [146].

From the final snapshot of the trajectory 50 dimers in the attractive range were extracted employing PICKY code, with the following restrictions: $R_{AB} = 20$ Å and $E^{inter} < -1$ kJ/mol. The DI was set to 0.1, because this value allowed for a variety of configurations to be sampled. However, many parameters concurring to DI still need accurate tuning and this value can not be taken as reference.

On this reference set the interaction energy was not QM computed, as previously done in

Chapter 2. A literature FF (σ and ϵ of [166]) was employed instead to reduce computational time. This set is here labeled as FF^{QM} because it replace the QM calculations of interaction energies and it is reported in the last column of Table 4.1. The "exact" value towards which the starting σ and ϵ ($\pm 30\%$ of the FF^{QM}) should converge is therefore known.

The fitting of Eq. 2.9 was performed on this reference set of 50 geometries, yielding a

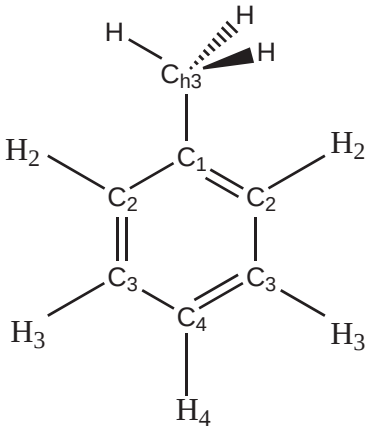

Figure 4.3: Toluene: full atomistic model

standard deviation of 2.12 kJ/mol. Due to the limited number of dimer configurations in the database, a small range of variability was applied on the parameters, so to prevent the function E^{inter} from going into an unphysical local minimum among the many presents. The obtained parameters are reported in the third column of Table 4.1.
These new intermolecular interaction parameters were employed for a second MD run, in the same conditions of temperature and pressure as the first and other 50 dimers were extracted. The fitting on the database of 100 geometries cat down the standard deviation of three order of magnitude: from 2.12 to $7.9 \cdot 10^{-3}$ kJ/mol (see fourth column of Table 4.1).

Finally, a third MD run was led, at high temperature (500 K) and pressure (1000 atm), to sample more repulsive geometries with shorter contact distances. Selection constraints were set as following in PICKY input file: $R_{AB} = 6$ Å and $-5 < E^{inter} < 20.0$ kJ/mol. A fitting performed on these 150 geometries yielded a standard deviation of $2.3 \cdot 10^{-2}$ kJ/mol, a value higher than that obtained in second run. It is apparent by looking at the last column of Table 4.1 that the reference σ are very well reproduced. As for ϵ, instead, the agreement is not as satisfactory. The fitting does not distribute the aromatic interactions equally on the five carbon sites and the function E^{inter} remains trapped in a local minimum. However,

if a further fit is performed on these parameters adding the constraint of equivalence among all aromatic C and H sites the function reaches a new minimum with a standard deviation of $1.3 \cdot 10^{-5}$ kJ/mol (set IV of Table 4.1). At any rates this is only a first investigation of PICKY performances on a very simple molecule and the obtained standard deviations can not be taken as reference values.

Intermolecular parameter: ϵ ($\cdot 10^{-2}$kJ/mol)						
Site	Start	I	II	III	IV	FF^{QM}
C_{h3}	14.05	11.97	11.06	19.87	20.12	20.12
H	9.39	7.32	17.29	13.30	13.39	13.39
C_1	23.03	23.03	36.17	27.69	32.93	32.96
C_2	23.03	23.03	32.59	39.08	32.93	32.96
C_3	23.03	23.03	31.26	24.61	32.93	32.96
C_4	23.03	23.03	33.09	47.81	32.93	32.96
H_2	8.98	6.90	12.97	12.64	12.80	12.80
H_3	8.98	6.90	13.14	13.63	12.80	12.80
H_4	8.98	6.90	13.47	10.56	12.80	12.80
Intermolecular parameter: σ (Å)						
	Start	I	II	III	IV	FF^{QM}
C_{h3}	4.63	4.33	3.58	3.56	3.56	3.56
H	3.19	2.89	2.46	2.46	2.45	2.46
C_1	4.54	4.24	3.54	3.54	3.49	3.49
C_2	4.54	4.24	3.50	3.46	3.49	3.49
C_3	4.54	4.24	3.52	3.56	3.49	3.49
C_4	4.54	4.24	3.46	3.41	3.49	3.49
H_2	3.13	2.83	2.40	2.41	2.41	2.41
H_3	3.13	2.83	2.41	2.39	2.41	2.41
H_4	3.13	2.83	2.42	2.45	2.41	2.41
St. Dev. (kJ/mol)	-	2.12	$7.9 \cdot 10^{-3}$	$2.3 \cdot 10^{-2}$	$1.3 \cdot 10^{-5}$	-

Table 4.1: Test on Toluene: intermolecular parameters ϵ and σ for toluene interacting sites. Starting and target parameters are listed in the second and last columns, respectively. Three iterations are reported. Set IV is obtained fitting on the same database of set III, but considering equivalent all aromatic H and C, see text.

4.6 Conclusions

In this Chapter a new approach for FF parameterization has been presented. The novelty with respect to the protocol seen in Chapter 2 and 3 is that the database of dimer geometries is extracted from MD trajectories. This strategy seems promising, because it provides a systematic way to sample populated regions of the dimer configurational and conformational phase spaces. However, this study is in its early stage and there are not enough tests to gauge if it will turn out to be a sound improvement of the protocol for the FF parameterization and if it will be sufficient to overcome the many problems of sampling and fitting. The application on toluene is presented just as a first test. Further ones are planned to accurately tune the DI threshold value and the weights of Eq. 4.10, so that DI_{core}, DI_{chain} and DI_{intra} might concur in appropriate proportions. Toluene and pyridine seem good candidates for these preliminary tests, because they do not possess flexible chains and allow for a more simple control of PICKY good working. Molecules with alkylic tails (for example 5CB) will be used for successive investigations. Once ascertained the reliability of the algorithm, PICKY will be inserted in the full FF procedure, and the parameters of an already studied molecule (such as HAB) could be thus refined and verified in MD simulations.

Finally, we plan to insert the fragment-fragment interaction energies of the FRM method in the fitting procedure. They could help in cutting down the redundancy of the sets of intermolecular parameters guiding the model function E^{inter} towards more physically sound minima.

CHAPTER

5

GEOMETRY OPTIMIZATION OF VAN DER WAALS DIMERS WITH FRM

In this Chapter a novel approach for exploring the energy minima of the potential energy surface of large and flexible van der Waals dimers is presented and tested. The total dimer energy is divided in intra- and inter-molecular contributions which can be computed at different levels of theory. The intermolecular energy, which is the time consuming part of the calculation, is computed by means of the Fragmentation Reconstruction Method (FRM), making possible the calculation of the interaction energy of large molecules. The method is validated by performing geometry optimizations through a quasi-Newton technique on two benchmark medium-size systems, where the comparison with a direct *ab initio* calculation is still computationally feasible. In both cases, a good agreement is achieved between geometries and energies of the resulting energy minima. The results presented in this Chapter have been published in the following article: "Geometry Optimization of Large and Flexible van der Waals Dimers: A Fragmentation-Reconstruction Approach", J. Chem. Theory Comput., **6**, 2536, (2010) [167].

5.1 Van der Waals interactions

Van der Waals (vdW) interactions [168, 169, 170, 171, 172] are known to play a relevant role in many different fields of science, ranging from soft matter [173, 174, 175, 176], to biochemistry [177, 178, 179], from molecular recognition [180] to nanotechnologies [181, 182, 183] and astrobiology [184]. The accurate calculation of these interactions with standard Quantum

Mechanical (QM) or *ab initio* methods still remains a great challenge. The nature of these interactions is purely quantum mechanical and strongly relies on a correct representation of the dynamical electron correlation. For this reason, within the *ab initio* methods, one has to employ post-Hartree–Fock (HF) techniques, whose computational cost dramatically increases along with molecular dimensions. Several strategies based on fragmentation have been proposed over the years to overcome this problem [25, 123, 124, 125, 126, 127, 128, 129, 130]. They rely on the possibility of dividing the whole system into small sub-systems and performing the calculations of interaction energies for each sub-system.

If an accurate calculation of interaction energies is problematic, the geometry optimization of a dimer of flexible molecules with respect to the total energy is even more challenging. The isolated equilibrium conformation of monomer A, in fact, can be altered by the interactions with a molecule B. A striking example can be found even in a relatively small molecule such as biphenyl, where the torsional angle between the two phenyl rings assumes different values according to the phase (crystal, liquid or gas) in which it is measured (see Ref. [185] and references therein). That is the reason why dimer energy minimizations need be performed in a non-rigid monomer geometry approximation.

Moreover, soft matter is characterized [173, 174, 175] by molecular and collective conformational changes driven by thermal fluctuations. An accurate sampling of several local energy minima is required to spot the most probable dimer conformations, fundamental to the understanding of condensed phase properties. This information can be accessed straightforwardly with molecular mechanics (MM), but it has been shown recently [114, 186, 187] that literature force-fields are not able to provide dimer structures in agreement with reference QM data for a large variety of systems.

A novel approach to study vdW complexes has been developed by our group, where minima of a dimer PES are explored by optimizing the relative position of monomers A and B, as well as their intramolecular geometry. This approach has been implemented in an original software code (POLDO) and takes advantage of the FRM [25, 91] route to intermolecular energy to perform geometry optimizations of large and flexible vdW dimers that would be otherwise impracticable with standard methods.

5.1.1 Investigation methods for Van der Waals complexes

Optimization of dimer geometries can become very expensive from a computational point of view and a compromise with method accuracy is necessary, even if fragmentation methods

are employed to speed up the computation of the interaction energy.

In the last decade, along with the impressive development of the computational resources, several groups have reported highly accurate calculations for model $\pi \cdots \pi$ interacting systems. Among others, the groups of Tsuzuki [188, 137], Hobza [136, 186, 179, 189] and Sherrill [190, 191, 138, 192, 187, 193, 194] have reported interaction energies at CCSD(T) level, extrapolated at the complete basis set limit, which is now often referred to as the "gold standard" of quantum chemistry. This approach, however, has an extremely high computational cost. It scales approximatively as N^7 and even calculations on monomers become rapidly unfeasible with the increase of molecular dimensions.

Methods based on density functional theory (DFT) are generally less expensive. Unfortunately, none of the standard density functionals was shown to be able to reproduce even benzene dimer interaction curves at a qualitative level [195, 196] because of an incorrect evaluation of dispersion contribution. Only recently, Zhao and Truhlar [197, 198, 199] succeeded in re-parameterizing DFT functional (M06-2X) in order to take dispersion into account, achieving a reasonable agreement with reference data for benchmark systems [200]. However, very recent results [189] have put in evidence some defects in the overall representation of the computed interaction energy curves. In the same paper [189], somewhat better performance was reported for the dispersion corrected DFT-D approach, where the standard DFT energy is corrected with an empirical term [201, 202, 193, 194] to reproduce most of the dispersion interaction energy of aromatic dimers.

Among mixed DFT-wavefunction techniques, SAPT-DFT approach was shown [203, 204, 189] to yield results in good agreement with the most accurate *ab initio* values. Its scaling properties with both the molecular dimensions and basis sets are more favorable than CCSD(T) methods [203], but this approach is still computationally too expensive for its straightforward application to the calculation of large vdW dimers.

Among the wavefunction-based methods, a computationally convenient post-HF method is the Møller-Plesset second order perturbation (MP2) theory. On the other hand, a major drawback of the MP2 method is the remarkable over-binding found for aromatic interactions [205, 206, 188, 190, 193, 207] when large basis sets are employed. To overcome this flaw, a few MP2-based methods were recently proposed. Among these, the spin-component-scaled MP2 (SCS-MP2) [208] was compared to CCSD(T) reference values for model systems [194, 207], resulting in a good agreement for $\pi \cdots \pi$ interactions, but not for H-bonded systems. The scaled MP3 method (MP2.5) [207] appears to be more accurate, but the computational cost

of this method is about one order of magnitude higher than standard MP2. A promising method [209] combines MP2 and time-dependent TDDFT response theory. It was proposed to improve the agreement with the reference data on a set of benchmark aromatic dimers, at a computational cost slightly higher than standard MP2, but the best agreement was obtained making use of rather large basis sets.

An alternative choice can be the adoption of the standard MP2 method, coupled with a small basis set (6-31G*), where the polarization exponent is modified to a smaller value (0.25 instead of the standard 0.80) and therefore named 6-31G*(0.25) [210]. The comparison with more expensive computational methods is positive for molecular complexes with stacking interactions [114, 211, 212, 189], because the intermolecular energy overestimation found with larger basis sets is avoided.

5.2 POLDO: a Fortran code for dimer geometry optimizations

POLDO is an original code written in our group in which a new method for accurate geometry optimizations is implemented. It can be used either to search for the most stable configuration or to investigate the relative stability of different local minima to explore some relevant portions of the dimer configurational space. The optimization algorithm is guided by the energy gradients and an approximate Hessian, in the framework of the so called quasi Newton methods.

The pivot of the whole procedure is the FRM method (see Section 2.1), thanks to which a dimer interaction energy can be recovered avoiding the energy calculation on the entire system. This is a consistent saving of computational costs and it allows for calculations on molecules made up of a large number of atoms, that would be otherwise unaffordable (such as large and flexible van der Waals complexes).

For the present purposes it is convenient to express the absolute energy E_{tot} of a vdW $A \cdots B$ dimer in the following way:

$$E_{tot}\left(AB\right) = \Delta E\left(AB\right) + E\left(A_0\right) + E\left(B_0\right) \tag{5.1}$$

where the labels A_0 and B_0 indicate the monomers in their isolated minimum energy conformations, whereas AB stands for the dimer geometry. As the last two terms of Equation (5.1) are constant, the geometry is optimized considering the $\Delta E\left(AB\right)$ term, which can be seen as the sum of two separate parts, namely an intermolecular ($\Delta E_{inter}\left(AB\right)$) and an

intramolecular ($\Delta E_{intra}(AB)$) contribution,

$$\Delta E(AB) = \Delta E_{intra}(AB) + \Delta E_{inter}(AB) \tag{5.2}$$

where

$$\Delta E_{intra}(AB) = [E(A) - E(A_0)] + [E(B) - E(B_0)] \tag{5.3}$$

and

$$\Delta E_{inter}(AB) = E(AB) - E(A) - E(B) \tag{5.4}$$

The main reason for considering two distinct contributions in Eq. 5.2 is that accurate calculation of ΔE_{intra} and ΔE_{inter} presents a different level of difficulty and in the proposed approach are computed in different ways. The former term may be evaluated employing standard QM techniques or by a suitable and accurate MM intramolecular force field (FF). In this case only the internal geometrical degrees of freedom to be optimized need to be included in the set of intramolecular coordinates. Conversely, the intermolecular term ΔE_{inter} is computed using the FRM approach (see Section 2.1), which includes the Counter Poise (CP) correction [134] to the Basis Set Superposition Error (BSSE). FRM approach does not rely on any specific method/basis set, on the contrary it can be used within whatever method. This fact, together with the possibility of treating intra- and intermolecular interactions at a different level of theory make POLDO extremely versatile.

POLDO code makes use of the following geometrical quantities:

1. The translational vector $\overrightarrow{R} \equiv (X, Y, Z)$, connecting a defined point of monomer A with a defined point of monomer B. These points may be the monomer center of mass (default choice), a defined atom or the midpoint of an assigned bond.

2. Vectors $\overrightarrow{\Omega}_i \equiv (\alpha, \beta, \gamma)$ of each monomer i. $\overrightarrow{\Omega}_i$ $(i = A, B)$ defines the absolute orientation of one monomer in a fixed reference frame through the three Euler angles α, β, γ. The rotation center is a point defined within each monomer. As the internal geometry of both monomers can change during the optimization path, the values of the Euler angles are not sufficient to describe the effective rotation of each monomer, and should be merely considered as degrees of freedom. Moreover, since the interaction energy only depends on the relative orientation, six orientational parameters are a redundant set. However, the inclusion in the optimization of Euler angles for both monomers, though

not strictly necessary, was found to speed up the convergence towards the absolute minimum.

3. Vector $\overrightarrow{Q}_i$ $(i = A, B)$, containing the internal coordinates of both monomers. Although POLDO can handle in principle any type and number of coordinates, it can sometimes be preferable [213] to optimize only "soft" degrees of freedom, *i.e.* those internal coordinates which exhibit rather flat energy profiles, as for instance torsional angles along σ bonds. Indeed, considering the low values of the interaction energies as compared with the intramolecular contribution, it is expected that in common vdW complexes only the "soft" degrees of freedom can be significantly affected by the presence of the second molecule.

The optimization is performed using a gradient-based technique in which at each step the new geometry is determined by a quasi Newton method. The QM Cartesian gradients are converted to energy derivatives with respect to the chosen degrees of freedom. The needed transformation matrices are computed by numerical techniques using a five point interpolation formula, which assures a sufficient accuracy and avoids singularities connected with the use of analytical derivatives involving quaternion, in the case of rotational motion. In particular, for the derivative with respect to the translational degrees of freedom, in which the monomer A is fixed in space and B is moved, one has

$$\frac{\partial E_{tot}}{\partial I} = \sum_{i \in B} \left(\frac{\partial \left(\Delta E_{inter} \left(AB \right) \right)}{\partial r_i} \right) \left(\frac{\partial r_i}{\partial I} \right) \quad ; \quad I = X, Y, Z \tag{5.5}$$

where r_i $(i = 1, ...3N_B)$ are the Cartesian coordinates of the atoms belonging to molecule B formed by N_B atoms. Similarly, for the rotational degrees of freedom

$$\frac{\partial E_{tot}}{\partial \alpha_{B(A)}} = \sum_{i \in B(A)} \left(\frac{\partial \left(\Delta E_{inter} \left(AB \right) \right)}{\partial r_i} \right) \left(\frac{\partial r_i}{\partial \alpha_{B(A)}} \right) \tag{5.6}$$

and analogous equations hold for β and γ. Finally the gradients for an internal coordinate $Q_{A(B)}$ of the molecule A(B) is computed by

$$\frac{\partial E_{tot}}{\partial Q_{A(B)}} = \sum_{i \in A(B)} \left(\frac{\partial E(A(B))}{\partial r_i} \right) \left(\frac{\partial r_i}{\partial Q_{A(B)}} \right) + \sum_{i \in A(B)} \left(\frac{\partial \left(\Delta E_{inter} \left(AB \right) \right)}{\partial r_i} \right) \left(\frac{\partial r_i}{\partial Q_{A(B)}} \right) \tag{5.7}$$

As many of the internal coordinates are kept frozen, the dummy index i in Equation (5.7) runs over all atoms involved in a change of the $Q_{A(B)}$ coordinate and not only over those involved in its definition. For instance for biphenyl (see next section), the only internal

coordinate $Q_{A(B)}$ chosen for optimization is the inter-ring dihedral angle $\phi_{A(B)}$. In this case the transformation matrix $\left(\partial r_i/\partial\phi_{A(B)}\right)$ is computed numerically by small rigid rotation $\delta\phi_{A(B)}$ of all atoms of the rings and detecting the corresponding changes δr_i.

The POLDO code is interfaced with the GAUSSIAN 03 [119] software and automatically starts a GAUSSIAN run for each QM calculation. The full minimization proceeds through the following steps.

1. The energy of each isolated monomer is optimized with respect to all its internal coordinates using the method chosen for the intramolecular contribution and reference energies, $E(A_0)$ and $E(B_0)$, are recovered.

2. The energy of each monomer at the starting geometry, $E(A)$ and $E(B)$, is computed with the same method chosen for step 1. POLDO recovers energies, relative Cartesian gradients and computes the $\Delta E_{intra}(AB)$ contribution according to equation (5.3).

3. POLDO builds all the GAUSSIAN input files needed by the FRM calculation. Thereafter all QM runs are automatically performed. Finally, all the resulting energies and Cartesian gradients are recovered from GAUSSIAN output files and combined in order to reconstruct the FRM interaction energy term $\Delta E_{inter}\,(AB)$.

4. The full energy E_{tot} is computed as a sum of internal and intermolecular contributions according to Equations (5.1) and (5.2).

5. All Cartesian gradients are converted into derivatives with respect to the chosen degrees of freedom and the Hessian matrix is updated for the current geometrical arrangement.

6. A new set of coordinates is computed according to the Newton-Raphson algorithm. If the total energy gradient and the computed displacements are small enough, the program ends.

7. Steps 2. to 4. are repeated with the new geometry. If the total energy decreases POLDO proceeds through steps 5. and 6., otherwise it performs a line search in the direction of the predicted displacement and it goes back to step 2.

5.3 Two case studies: biphenyl and 5CB

Two benchmark medium-size molecules were chosen to test and validate the proposed method for dimer optimizations: biphenyl and 4-*n*-pentyl-4'-cyanobiphenyl (5CB). Biphenyl is a com-

mon case study for vdW interactions and it was chosen for two main reasons. The first is that it has sufficiently "small" molecular dimensions to allow us for direct optimizations (*i.e.* without fragmenting) and these are fundamental tests to assess the quality of FRM performances. The second is that a fragmentation scheme of biphenyl molecule into benzene moieties had already been validated (at MP2/6-31G*(0.25) level) [114].
5CB was chosen because it is one among the smaller prototypes of vdW dimers containing three different moieties, namely aromatic (phenyl), substituted aromatic (cyano-phenyl) and aliphatic (pentyl) bricks and because FRM had already been successfully employed on it, too (at MP2/6-31G*(0.25) level) [25, 131].

As said previously, POLDO allows for the use of any methods for both intra- and intermolecular energies. However, even if FRM reduces the dimensions of the problem avoiding the computation of the intermolecular energy on the whole dimer, a reasonable compromise with the method accuracy has to be adopted, also in view of the large number of calculations possibly involved in a dimer geometry optimization. A brief overview of some investigation methods for vdW complexes was given in Section 5.1. Among them the MP2/6-31G*(0.25) level of theory was chosen for this study, as beside its numerous advantages, FRM fragmentation schemes for both molecules had already been validated within this approach.

5.3.1 Computational details

All isolated monomer calculations (Eq. 5.3) were performed at the DFT level of theory, using the B3LYP functional with a correlation consistent cc-pVDZ basis set. In the case of biphenyl the intramolecular contribution $E(k)$ ($k = A, B$), was computed at MM level, using the following expression for the inter-ring dihedral

$$E(k) = \sum_n C_n(1 + cos(n\phi_k)); \qquad k = A, B \tag{5.8}$$

where all the remaining internal coordinates are at their equilibrium values. The set of parameters C_n was taken from Ref. [185], where they were derived from accurate QM calculations.

All FRM fragment-fragment calculations were performed at the MP2/6-31G*(0.25) level, in the supermolecule approach and corrected for the BSSE with the CP correction. MP2 direct optimizations and single point calculations performed on the whole dimers were correspondingly computed with the same basis set and CP corrected.

5.3.2 MP2/6-31G*(0.25) validation

Large and flexible vdW dimers may exhibit several energy minima, in which the relative arrangements of the monomers can be very different from simple stacked geometries and where, for instance, both $\pi \cdots \pi$ and $H \cdots \pi$ interactions play different roles. For this reason, the validation of any level of theory has to be performed for several geometries. The benzene dimer is a good candidate for this validation. It can be considered as a prototype of vdW interactions and, at the same time, its dimensions allow high-level reference calculations.

To this aim, MP2/6-31G*(0.25) interaction energies were computed and results validated *vs* those of Ref. [193] and [194]. In these papers Sherrill and coworkers reported the interac-

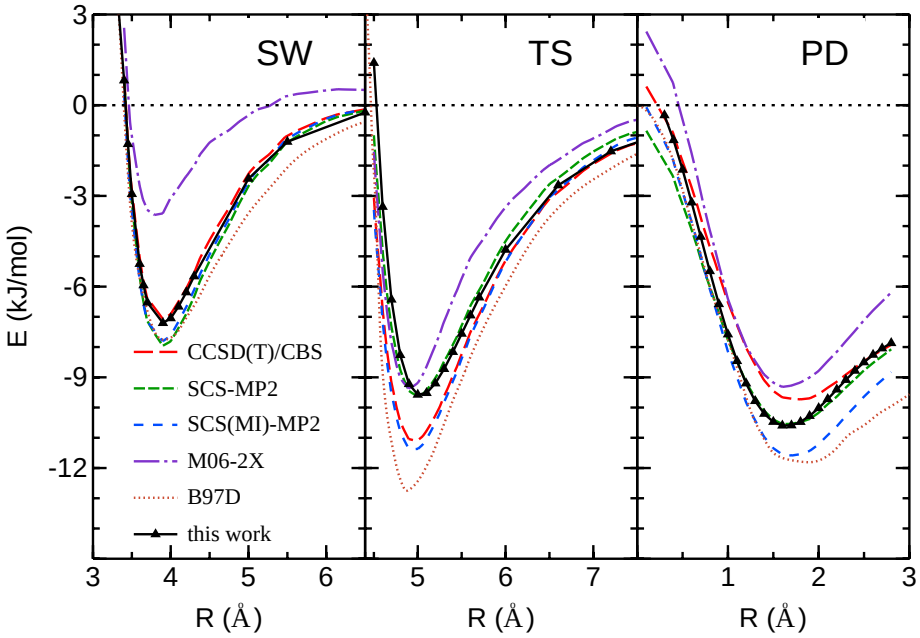

Figure 5.1: Interaction energies for sandwich (SW), T-shaped (TS) and parallel displaced (PD) arrangements of benzene dimer at different levels of theory. E is the ΔE_{inter} (AB) of Eq. 5.4. All energies were taken from Ref. [193] and [194] where dimer geometries are described in detail (PD displacement is 3.4 Å). Curves calculated at MP2/6-31G*(0.25) level are reported with triangles.

tion energy curves for sandwich (SW), T-shaped (TS) and parallel displaced (PD) benzene dimers at CCSD(T) level, extrapolated at the complete basis set limit (CCSD(T)/CBS), which can be considered the reference values. In Figure 5.1 some of those curves are shown and compared with those obtained using the MP2 method with the modified 6-31G*(0.25) basis set.

Besides maintaining the correct relative order ($\Delta E_{inter}^{TS} \simeq \Delta E_{inter}^{PD} < \Delta E_{inter}^{SW}$), MP2/6-

31G*(0.25) shows an overall good agreement with the reference data. The accord is quantitative for the SW arrangement, whereas it slightly overestimates and underestimates CCSD(T)/CBS binding energies for PD and TS geometries by ~ 0.9 and ~ 1.5 kJ/mol, respectively. A good agreement results on the intermolecular separation at the minimum for all geometries. Most important, the comparisons reported in Ref. [193] and [194] show that all other methods taken into account perform either worse or comparably. Therefore, MP2/6-31G*(0.25) method seems a good compromise between accuracy and computational cost, at least for the benzene dimer.

5.3.3 Case Study I: biphenyl

Preliminary tests

Two preliminary tests were envisaged on a sandwich configuration of a biphenyl dimer. In both tests the intramolecular contribution ΔE_{intra} was computed at MM level according to Eq. 5.8, while ΔE_{inter} was computed at MP2/6-31G*(0.25) level of theory, within the FRM approach.

The FRM fragmentation scheme applied to each biphenyl monomer is that shown in Figure 5.2. Indeed, cutting along the inter-ring bond is the only possible fragmentation choice that

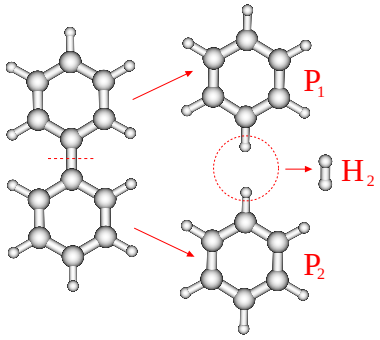

Figure 5.2: Fragmentation scheme for biphenyl: P_1 and P_2 are two benzenes and H_2 is an intruder molecule. In the above picture, both moieties and intruder molecule have been shifted (red arrows) only for the sake of clarity (see text). For instance both H atoms of the intruder molecule H_2 lie on the C-C bond connecting the two aromatic moieties. These moieties will be labeled with a further subscript A or B (that is $P_{1A(B)}$, $P_{2A(B)}$, $H_{2A(B)}$) depending on which of the two biphenyl monomers they belong to.

respects the necessary electronic density criteria explained in Section 2.1. H atoms were added to saturate the valence of the resulting C_6H_5 moieties. The spatial positions of the fragments are unchanged with respect to the whole molecule and the location of the intruders H_{2A} and H_{2B} is unambiguously determined by the internal geometry of the saturated fragments. In other words, the Cartesian coordinates of all atoms in the fragments are unchanged with respect to the ones in the whole molecule, resulting in a slightly altered H_2 bond distance (0.68 Å, instead of the equilibrium value of 0.74 Å). The intermolecular energy of the whole biphenyl dimer is thus made up of the following contributions (see Figure 5.2):

$$\Delta E_{inter}(AB) =$$

$$\underbrace{\Delta E(P_{1A}\cdots P_{1B})+\Delta E(P_{1A}\cdots P_{2B})+\Delta E(P_{2A}\cdots P_{1B})+\Delta E(P_{2A}\cdots P_{2B})}_{PhH\cdots PhH}-$$
$$(\underbrace{\Delta E(H_{2A}\cdots P_{1B})+\Delta E(H_{2A}\cdots P_{2B})+\Delta E(P_{1A}\cdots H_{2B})+\Delta E(P_{2A}\cdots H_{2B})}_{H_2\cdots PhH})+$$
$$\Delta E(H_{2A}\cdots H_{2B}) \tag{5.9}$$

where $\Delta E(i_A\cdots j_B)$ is the interaction energy between fragment i, belonging to A, and fragment j, belonging to B.

The first test was the optimization of a Face to Face arrangement at a distance of 5.5 Å in the Y direction (see Figure 5.3, top panels). The two dihedral angles defining the torsion around the inter-ring bonds were constrained at 0°, in planar conformation. Only

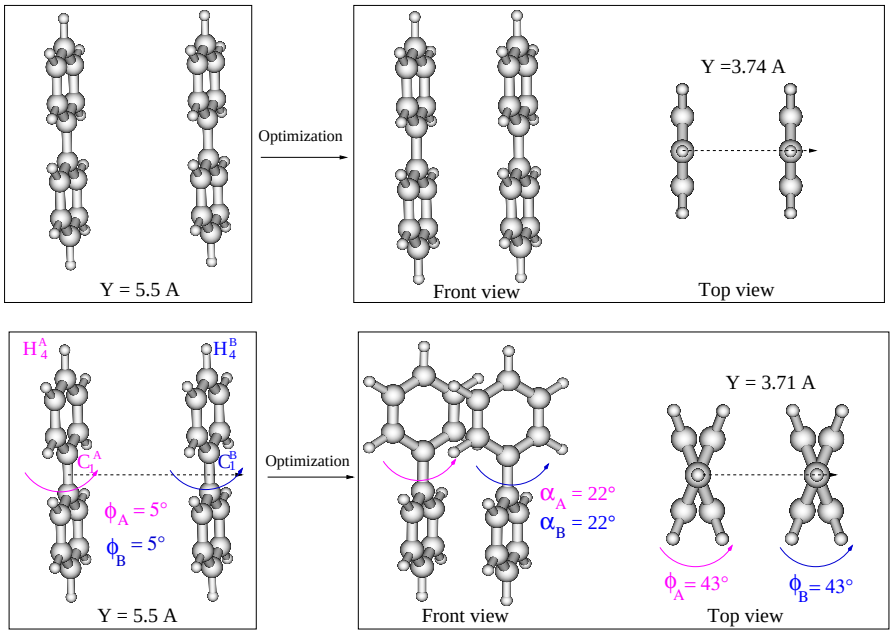

Figure 5.3: Biphenyl dimer, Test 1 (top panels) and 2 (bottom panels), starting (left) and final (right) geometries.

the intermolecular distance Y was optimized: all other coordinates were kept frozen to their initial value, including ϕ dihedrals. The trend of the total energy and its gradient with respect to Y along this mono-dimensional minimization are reported in Figure 5.4. In the left top panel it appears that the total energy $E_{tot}(AB)$ decreases to -5 kJ/mol, shortening the intermolecular separation from 5.5 Å to 3.75 Å. The energy derivative reported in the top right panel correctly goes to 0. Owing to planar internal geometry of A and B, the FF

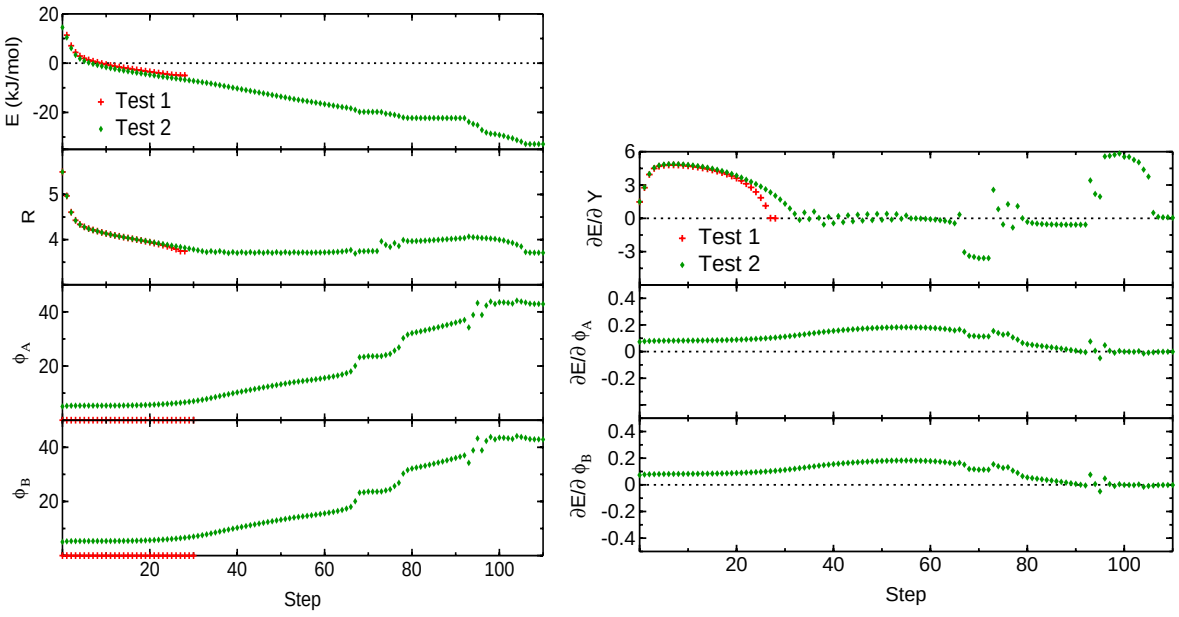

Figure 5.4: Optimized variables and derivatives during preliminary tests performed on the biphenyl dimer. Red cross symbols refer to the first test (Test 1, where monomer geometries were constrained to be planar) and green diamonds to the second test (Test 2, where ϕ of A and B monomers could relax).

torsional potential energy $\Delta E_{intra}(AB)$ amounts to $\simeq$ 20 kJ/mol, whereas the intermolecular energy $\Delta E_{inter}(AB)$ is $\sim$ -25 kJ/mol.

In the final geometry (Figure 5.3, top right panel) the phenyl groups of A and B are in sandwich (SW) and parallel displaced (PD) arrangements. Table 5.1 shows the different fragment pairs contributions to the intermolecular energy. Dimers $P_{1A}\cdots P_{1B}$ and $P_{2A}\cdots P_{2B}$ are isoenergetic ($\sim$ -7 kJ/mol), as it could be expected considering the symmetry of their spatial arrangement. This value results in good agreement with a literature value of -6.7 kJ/mol, recently reported by Sherrill *et al.* [193] at the best level of theory for two benzenes in the same stacked SW configuration (at 3.5 Å). Fragment pairs $P_{1A}\cdots P_{2B}$ and $P_{2A}\cdots P_{1B}$ are, instead, in a PD geometry and contribute to the total interaction energy for a non negligible amount (-5.1 kJ/mol). Remaining energy contributions coming from intruder fragments modify the final sum only in a minor way. It is worth noticing that, due to the fact that HF contribution is strongly repulsive for the SW benzene moieties, the dispersion is the main attractive force which accounts for the stability of the biphenyl dimer, at least in this geometrical arrangement.

In a second test both intra (ϕ) and intermolecular (Y, $\alpha_{A(B)}$) coordinates were optimized.

Fragments $i_A \cdots j_B$		ΔE_{inter}	ΔE^{HF}_{inter}
$P_{1A} \cdots P_{1B}$	(SW)	-7.00	20.41
$P_{2A} \cdots P_{2B}$			
$P_{1A} \cdots P_{2B}$	(PD)	-5.12	-0.07
$P_{2A} \cdots P_{1B}$			
$H_{2A} \cdots H_{2B}$		0.06	0.10
$H_{2A} \cdots P_{1B}$		0.14	0.47
$H_{2A} \cdots P_{2B}$			
$P_{1A} \cdots H_{2B}$			
$P_{2A} \cdots H_{2B}$			
Biphenyl $\cdots$ Biphenyl		-24.73	38.90

Table 5.1: Fragment-fragment interaction energies in kJ/mol for the final geometry of the first test (Fig. 5.3, top right). The second and third column reports intermolecular MP2 and HF energies, respectively. All contributions sum to the interaction energy of the biphenyl dimer with a positive or negative sign according to Eq. (9).

A and B monomers were displaced in SW arrangement at 5.5 Å far from each other and their inter-ring dihedral ϕ were set at 5° (Figure 5.3, bottom left panel). In the top left panel of Fig 5.4 it can be seen as the total energy $E_{tot}(AB)$ decreased to -33 kJ/mol during optimization. The total energetic gain with respect to the former test is ascribed to the null value of the intramolecular contribution, and to the intermolecular energy which lowered by $\sim$ 8 kJ/mol. The coupling between intermolecular and internal degrees of freedom is rather evident during optimization. As the intermolecular distance drops below 4 Å, the interaction between the phenyl rings helps the rotation of the ϕ dihedral, which starts a rapid increase toward $\sim 40°$. During the final steps, conversely, even small changes of ϕ may lead to repulsive arrangements of $P_{1A} \cdots P_{1B}$ and $P_{2A} \cdots P_{2B}$ fragment pairs, causing abrupt changes in the energy gradient with respect to Y. However, the intermolecular distance Y eventually decreases to 3.71 Å , not far from the value found in the previous test, showing that the internal flexibility does not modify the equilibrium separation. In fact, in the final geometry ($\phi_A \simeq \phi_B \simeq 40°$) intramolecular contributions are null, indicating that, at least for this particular arrangement, two-body interactions are not sufficient to move ϕ towards the planar geometry observed in the crystal phases of biphenyl.

Table 5.2 lists all the contributions to $\Delta E_{inter}(AB)$ from the fragment pairs. In the final

Fragments $i_A \cdots j_B$		ΔE_{inter}	ΔE_{inter}^{HF}
$P_{1A} \cdots P_{1B}$	(PD)	-10.36	23.28
$P_{2A} \cdots P_{2B}$			
$P_{1A} \cdots P_{2B}$	(CD)	-5.52	1.18
$P_{2A} \cdots P_{1B}$			
$H_{2A} \cdots H_{2B}$		0.07	0.12
$H_{2A} \cdots P_{1B}$		0.30	0.72
$H_{2A} \cdots P_{2B}$			
$P_{1A} \cdots H_{2B}$			
$P_{2A} \cdots H_{2B}$			
Biphenyl $\cdots$ Biphenyl		-32.89	46.16

Table 5.2: Fragment-fragment interaction energies in kJ/mol for the final geometry of the second test (Fig. 5.3, bottom right). The second and third column reports intermolecular MP2 and HF energies, respectively.

geometry, fragment pairs $[P_{1A} \cdots P_{1B}\ ;\ P_{2A} \cdots P_{2B}]$ and $[P_{1A} \cdots P_{2B}\ ;\ P_{2A} \cdots P_{1B}]$ are found in PD and CD (Cross Displayed) arrangements, respectively (see bottom right panel of Figure 5.3). Thus the introduction of internal flexibility allows the formation of PD fragments that are more stable than the SW ones found in Test 1 (where the planarity was imposed) and cause the aforementioned energy decrease of 8 kJ/mol.

Validation

The starting geometry was created by randomly displacing monomer B and setting both ϕ at 28° as shown in Figure 5.5. The energy of this dimer is -10.8 kJ/mol and it results from a sum of ΔE_{inter} = -15.4 kJ/mol and ΔE_{intra} = 4.0 kJ/mol. The dimer conformation was optimized with POLDO software by varying the translational ($\overrightarrow{R}$) and rotational ($\overrightarrow{\Omega}_B$) sets of coordinates together with the internal dihedrals ϕ_A and ϕ_B.

A rapid decrease to 0° of β_B angle takes place during the optimization. This indicates a

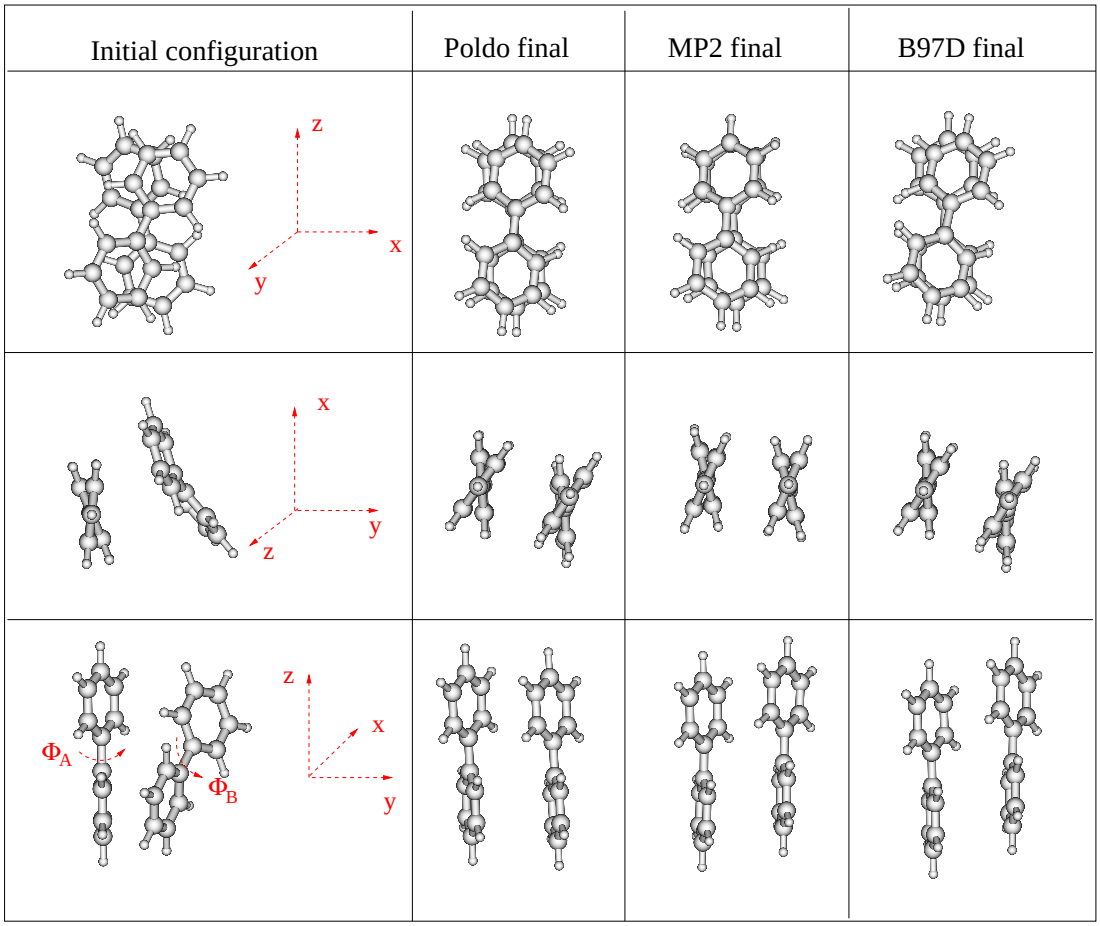

Figure 5.5: Complete optimization of a randomly placed biphenyl dimer. Starting (left column) and POLDO optimized (second column) geometries are shown from different points of view. The third and fourth columns refer to MP2 and B97D direct optimizations of the whole dimer, respectively.

tendency of the two biphenyl monomers to realign their *para* axes, in order to maximize the $\pi \cdots \pi$ interactions. The inclusion of translational degrees of freedom allows the molecules to move along Y reducing their distance to 3.6 Å, with a small displacement (-1.7 Å) along the X direction. Both torsional dihedrals reach the equilibrium value found for the isolated

monomer. The result is a local dimer minimum, almost isoenergetic (-31.5 kJ/mol *vs* -32.9 kJ/mol) with that found in the second test of the preliminary optimizations, where the

	Direct MP2	POLDO	B97D
ϕ_A	37.0°	40.0°	34.4°
ϕ_B	37.0°	40.0°	34.6°
$H_4^A\widehat{C_1^AC_1^B}H_4^B$	4.6°	8.0°	9.6°
$H_4^AH_4^B$	3.85 Å	4.04 Å	3.91 Å
$H_{4'}^AH_{4'}^B$	3.84 Å	3.62 Å	3.92 Å
$C_4^AC_4^B$	3.81 Å	3.97 Å	3.87 Å
$C_{4'}^AC_{4'}^B$	3.80 Å	3.64 Å	3.88 Å
$C_1^AC_1^B$	3.70 Å	3.81 Å	3.79 Å
$C_{1'}^AC_{1'}^B$	3.70 Å	3.74 Å	3.79 Å
$E(AB)$	-34.2 kJ/mol	-31.5 kJ/mol	-31.2 kJ/mol

Table 5.3: Optimized biphenyl dimer: total energy and geometrical values obtained with a direct MP2 (second column), POLDO (third column) and B97D optimizations.

biphenyl long axes were constrained to be parallel. Some relevant geometrical data of the final optimized dimer are reported in Table 5.3.

As biphenyl molecular dimensions still allow us for an MP2 direct optimization on the whole dimer, this was performed for comparison and for the validation of our method. The direct MP2 optimization was performed with the same basis set employed in all fragment-fragment calculations, that is 6-31G*(0.25), starting from POLDO final geometry, and each optimization step was CP corrected for BSSE. The final energy found with the direct MP2 route is -34.2 kJ/mol: 2.7 kJ/mol more attractive with respect to the minimum computed by our algorithm. This difference can be ascribed to the different level of theory used for ΔE_{intra} and to small rearrangements of the internal geometry which are allowed in direct MP2 but not in POLDO. It is worth stressing that this energy difference cannot be attributed to FRM inaccuracies, as the direct MP2 energy of the final geometry obtained by POLDO is -31.9 *vs* -31.5 kJ/mol.

A further test was performed by optimizing the whole biphenyl dimer using a DFT-D technique, namely the B97D functional with the TZV2P basis set as first proposed by Grimme [202]. The performances of this dispersion corrected approach were recently tested [194] on

the benzene dimer, giving results comparable with the MP2/6-31G*(0.25) method, as reported in Figure 5.1. A B97D calculation was performed on the final geometry optimized by POLDO and an intermolecular energy of -29.7 kJ/mol was found. Conversely, the final optimized energy found with this method was -31.2 kJ/mol, not far from the direct MP2 value, and very close to the one obtained with POLDO procedure.

Fragments $i_A \cdots j_B$		ΔE_{inter}	ΔE_{inter}^{HF}
$P_{1A} \cdots P_{1B}$	(PD)	-9.70	26.72
$P_{2A} \cdots P_{2B}$		-10.67	18.06
$P_{1A} \cdots P_{2B}$	(CD)	-4.59	-0.07
$P_{2A} \cdots P_{1B}$		-5.71	2.02
$H_{2A} \cdots H_{2B}$		0.05	0.09
$P_{1A} \cdots H_{2B}$		0.01	0.36
$P_{2A} \cdots H_{2B}$		0.41	0.88
$H_{2A} \cdots P_{1B}$		0.42	0.94
$H_{2A} \cdots P_{2B}$		0.03	0.35
Biphenyl - Biphenyl		-31.51	49.35

Table 5.4: Fragment-fragment energy contributions (kJ/mol) in the POLDO optimization of the biphenyl dimer. The second and third column report intermolecular MP2 and HF energies, respectively.

In Table 5.3 geometrical values for direct MP2 and B97D optimizations are reported for comparison and in Figure 5.5 POLDO, direct MP2 and B97D final geometries are shown in second, third and fourth columns, respectively. Notwithstanding the satisfactory agreement among the three energy values, the final optimized geometries show some minor differences, suggesting that the PES around the minimum is rather flat. All algorithms predict a non planar value for ϕ_A and ϕ_B and an intermolecular distance in the range 3.7-3.9 Å. An estimate of how much A and B long axis are collinear can be gained measuring the dihedral angle defined by the quadruplet of atoms $H_4^A - C_1^A - C_1^B - H_4^B$. The latter goes from an initial value of 38° to a final one of 5°, 8° and 10° in the direct MP2, POLDO and B97D optimized geometries, respectively.

Within the FRM, the intermolecular energies of all fragment pairs are directly available and can be used to get a deeper insight into the forces driving the optimization. Referring to the fragment labels defined in Figure 5.2, it can be seen that in the final geometry the

benzenes of A and B monomers are in parallel (PD) and cross displaced (CD) arrangements. In Table 5.4, energy contributions for all fragment pairs are reported. From these values it results that also the moities placed in CD geometries give a not negligible contribution to the intermolecular energy, even though the major contribution comes from the PD arrangements.

5.3.4 Case study II: 5CB

5CB dimer was chosen as second benchmark calculation. In this case, both intra- and intermolecular energies were computed with QM methods. The intramolecular energy was evaluated at the DFT level (B3LYP/cc-pVDZ) and the intermolecular calculations were performed using MP2/6-31G*(0.25) level of theory, within the FRM method.

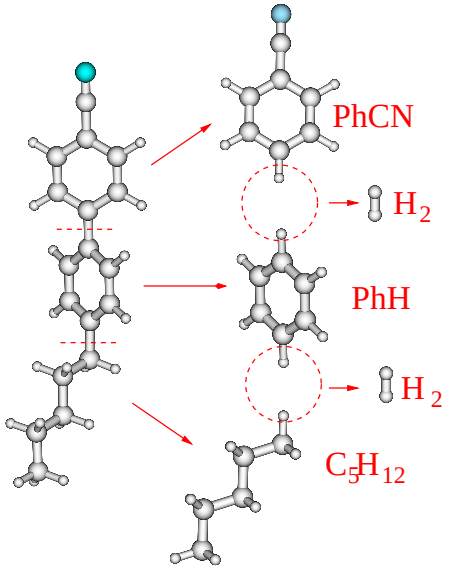

Figure 5.6: 5CB fragmentation scheme. All moieties are labeled with a subscript A or B (*i.e.* $PhH_{A(B)}$) depending on which of the two 5CB monomers they belong to.

Each 5CB monomer was fragmented by a cut along the inter-ring bond and the aromatic-aliphatic linkage. The valence of all fragments was saturated with H atoms, obtaining for each monomer three moieties (cyanobenzene, benzene and *n*-pentane) and two H_2 intruder molecules [131], as shown in Figure 5.6.

Energy minima were searched starting from different configurations. The two molecular long axis can be considered in first approximation as lying along the cyano-biphenyl *para* axis, so that Parallel (P) and Antiparallel (An) arrangements can be distinguished according

Geometry	$\Delta E(AB)$	$\Delta E_{intra}(A)$	$\Delta E_{intra}(B)$	$\Delta E_{inter}(AB)$
PFF1	-44.40	0.77	1.30	-46.47
PFF2	-47.23	0.79	2.85	-50.87
PSF	-31.05	0.37	0.04	-31.46
PD	-39.86	0.00	0.00	-39.86
An	-51.16	0.33	0.02	-51.51

Table 5.5: 5CB, summary of optimized energies for different arrangements. All energies are in kJ/mol.

on their mutual orientation. In the first, the long axes point in the same direction, while they point in opposite directions in the second. Among all possible P dimers Face-to-Face (PFF), Side-to-Face (PSF) and Displaced (PD) geometries were investigated. In PFF the aromatic rings of the two monomers are in a sandwich spatial disposition, they are found in a T-shaped geometry in the PSF and Parallel displaced geometries were obtained from PFF by displacing one monomer along its long axis. Final energy contributions and selected geometrical quantities for all investigated arrangements are summarized in Table 5.5 and 5.6, respectively.

PFF1 arrangement was obtained as shown in Figure 5.7. Two 5CB monomers in their

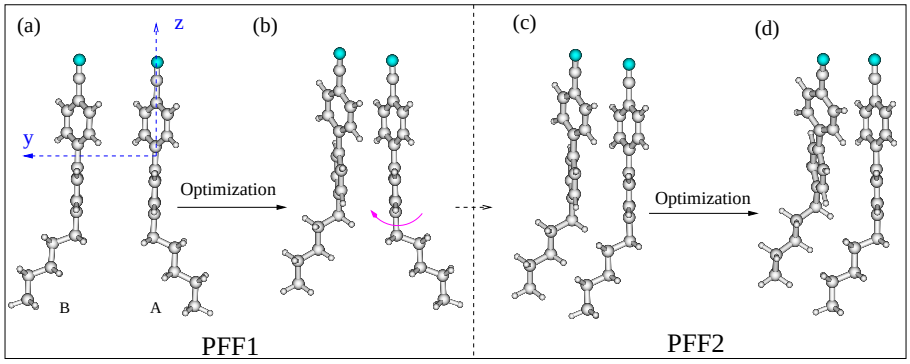

Figure 5.7: 5CB PFF1 (starting (a) and final (b)) and PFF2 (starting (c) and final (d)) geometries. (c) was obtained from (b) through rotation of the first dihedral of the side chain.

isolated optimized conformation were superimposed. After that, monomer B was shifted by 5.5 Å along the vector normal to the central ring plane and an $\alpha_B = 180°$ rotation was performed (geometry (a) in Figure 5.7). During optimization PFF1 turns into a sort of PD arrangement: the aromatic rings come nearer, but a displacement takes place along

the long molecular axis and the X direction (see Figure 5.7). In the final configuration (geometry (b) in Figure 5.7), 5CB long molecular axes are not anymore parallel and the dihedral angle defined by the quadruplet $C_1^A - C_{1'}^A - C_{1'}^B - C_1^B$ changes from 0° to 20°. A possible cause of this rotation may be the CN dipole - dipole repulsion. As far as dihedral

	PFF1	PFF2	PSF	PD	An
$\phi_A - \phi_B$	29.0 - 30.0	30.0 - 27.0	31.8 - 37.5	34.0 - 33.0	32.0 - 34.0
$C_1^A\widehat{C_{1'}^A C_{1'}^B}C_1^B$	-20.7	-31.4	-24.0	13.7	-14.7
N-N	4.2	4.8	6.4	5.95	13.6
C_4-C_4	3.8	4.1	5.7	5.7	3.7 (C_4-$C_{4'}$)
C_1-C_1	3.7	3.7	5.1	5.4	3.7 (C_1-$C_{1'}$)
$C_{1'}$-$C_{1'}$	3.7	3.8	4.9	5.2	3.7 ($C_{1'}$-C_1)
$C_{4'}$-$C_{4'}$	3.9	4.3	4.7	5.0	3.9 ($C_{4'}$-C_4)

Table 5.6: Characterization of the resulting 5CB dimer minima by selected geometrical quantities. Angles are reported in degrees and distances in Å.

angles are concerned, it is interesting to note that inter-ring (ϕ) values are different from the ones computed in gas phase ($\sim 42°$), but similar to those expected in condensed phase ($\sim$30°) [121]. Conversely, no conformational changes are induced in side chains by dimer interactions. The total energy of the dimer, E_{tot}(AB), decreases from -17.5 kJ/mol to -44.4 kJ/mol, with A and B intramolecular energies accounting for 0.8 and 1.3 kJ/mol, respectively, and ΔE_{inter}(AB) = -46.5 kJ/mol. As reported in Table 5.7, FRM correctly reconstructs the interaction energy, once more. An MP2 direct calculation performed on the final POLDO optimized whole dimer geometry gives, in fact, $\Delta E_{inter}(AB)$ = -47.5 kJ/mol.

The most relevant fragment-fragment contributions to ΔE_{inter} are reported in Table 5.7. As expected, the main contributions to the total intermolecular energy come from the $\pi \cdots \pi$ pair interactions. Cyanobenzene pair is found in a PD-like configuration whose large stability is little affected by the repulsive dipole-dipole interaction, due to the aforementioned rotation of the CN groups. The second contribution comes from the benzene pair, which takes advantage from the SW to PD displacement. In the optimized geometry, chain-chain interactions do not contribute significantly, because they point in opposite directions. If one of them is rotated by 180° around the *para* axis of 5CB, PFF2 geometry is generated as shown in Figure 5.7 ((c)). After optimization (Figure 5.7, (d)), the chain $\cdots$ chain energy amounts to -5.35 kJ/mol (see

Fragment $i_A \cdots j_B$	PFF1	PFF2	PSF	PD	An
PhCN $\cdots$ PhCN	-14.50	-12.97	-7.37	-9.86	-3.54
PhCN $\cdots$ PhH	-7.77	-8.62	-5.95	-0.53	-14.09
PhCN $\cdots$ C_5H_{12}	-0.58	-0.61	-0.44	-0.05	-5.25
PhH $\cdots$ PhCN	-4.86	-5.23	-1.75	-13.75	-14.81
PhH $\cdots$ PhH	-10.36	-9.74	-8.65	-6.56	-6.09
PhH $\cdots$ C_5H_{12}	-2.62	-2.44	-3.39	-0.38	-0.45
C_5H_{12} $\cdots$ PhCN	-0.20	-0.18	-0.13	-2.34	-4.72
C_5H_{12} $\cdots$ PhH	-1.63	-3.27	-1.27	-4.58	-0.42
C_5H_{12} $\cdots$ C_5H_{12}	-1.34	-5.35	-2.62	-1.15	-0.02
$\Delta E_{inter}(AB)$ total	-46.47	-50.87	-31.46	-39.86	-51.51
Direct MP2:	-47.50	-51.09	-31.63	-40.17	-52.57

Table 5.7: 5CB, more relevant optimized fragment-fragment contributions to the dimer $\Delta E_{inter}(AB)$ in different geometries. In the last row the MP2 energy computed on the whole POLDO optimized geometry is reported. All energies are in kJ/mol.

Table 5.7) and, due to the fact that all other fragment pair interactions are little affected by this chain rotation, PFF2 total interaction energy decreases from -46.7 kJ/mol (PFF1-opt) to -50.9 (PFF2-opt).

The next optimization was performed selecting a PSF arrangement as starting geometry (see Figure 5.8, left panel), which is characterized by a T-shaped-like initial disposition of the aromatic rings. Owing to the stability of the T-shaped benzene dimer, an interaction energy comparable with the previous ones was expected. However, as reported in Table 5.7, this was not the case. The main reason resides in a reduced stability of the PhCN dimer in a T-shaped configuration with respect to a PD one. On the contrary, the T-shaped benzene pair accounts for the maximum contribution (-8.6 kJ/mol) to the total intermolecular energy. This global lower interaction is consistent with the ϕ_A, ϕ_B values closer to those of the isolated molecule.

Another test was devised by displacing the monomer B of PFF1 dimer by ~ 4 Å along Z in a PD arrangement. During optimization, a β rotation of B took place, together with minor translational shifts bringing the C_4 atom of B in front of the $C_{1'}$ of A monomer. A better comprehension of spatial displacement of A and B can be gained looking at the intermolecular energies of fragment-fragments pairs, as reported in Table 5.7. Benzene-cyanobenzene pairs

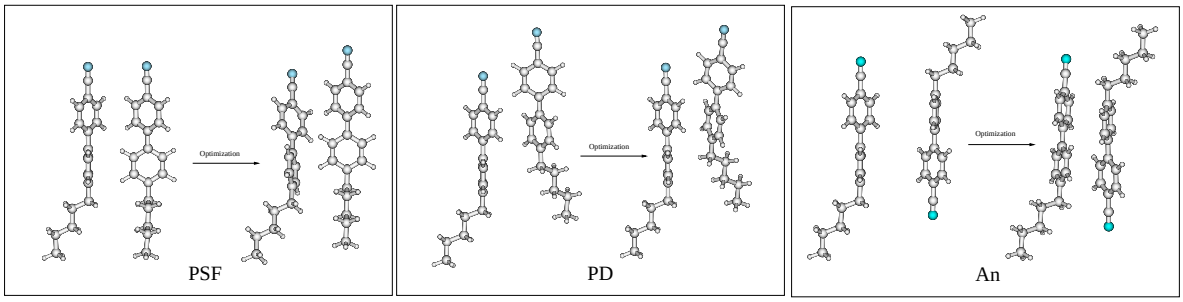

Figure 5.8: Parallel side-face (PSF, left panel), parallel displaced (PD, central panel) and antiparallel (An, right panel) starting and final geometries.

contribute by -13.75 kJ/mol and -0.53 kJ/mol, because the displacement along Z led the former pair in a stacked conformation and the latter to large distance. The optimized PD dimer is also stabilized by $\pi \cdots \pi$ homo-dimer interactions (-9.86 and -6.56 kJ/mol) as well as one pentane-cyanobenzene pair (-4.58 kJ/mol). The final interaction energy $\Delta E_{inter}(AB)$ sums up to -39.86 kJ/mol, showing that the PD optimized geometry is a local minimum more stable than the PSF dimer, but less favorable than the PFF ones.

Finally, an antiparallel Face-to-Face (An) 5CB dimer geometry was generated. This configuration is reported in Figure 5.8 and it was obtained rotating monomer B of 180° around β and displacing it at 6 Å far from A, along Y. In this way the C_4 atom of one molecule faces the $C_{4'}$ of the other, and the C_1 atom of A(B) overlooks the $C_{1'}$ atom of B(A). During the optimization Y distance decreased to 3.7 Å and B was subjected to a small β rotation. This caused a non perfect stacking of the aromatic rings in the final configuration. By Table 5.7 it appears that the most important contributions are the cyanobenzene-benzene interactions, each accounting for ∼-14 kJ/mol. This is due to the antiparallel arrangement and it was not seen in the previous cases. The cyanobenzene and benzene homo-dimer contributions are much smaller, whereas the aliphatic-aromatic interactions play now an important role. Once again side chain dihedrals are not affected by the presence of the second molecule, whereas inter-ring dihedral is found around 33°. The final interaction energy $\Delta E_{inter}(AB)$ is -50.1 kJ/mol. This suggests that, at least for the phase space explored here, dimers of An type are the most stable configurations. This conclusion seems to be consistent with experimental observation of 5CB's nematic phases with zero permanent dipole (see Ref. [91] and references therein). This is an example of how information on dimers can help in a deeper understanding of condensed phase properties: in this case the origin of the lack of permanent dipole in

5CB condensed ordered phases can, in fact, be tracked down to the greater stability of the antiparallel configuration of the dimers.

5.4 Conclusions

The optimization procedure implemented in the POLDO code was successfully tested on some biphenyl and 5CB dimers. Thanks to the use of FRM the computational cost of the intermolecular interaction was lowered by almost four and five times (for biphenyl and 5CB, respectively), with respect of a direct (without fragmentation) performance. This is a great advantage, together with the possibility of computing inter- and intra-molecular interactions at different level of theory. In the next future we plan to employ this method for the geometry optimization of large systems with a particular attention to molecules of biological interest. Indeed, this approach allows to take into account, during the optimization process, selected internal degrees of freedom, while retaining a fixed geometry for more rigid parts of the monomer under study. This possibility seems for instance to fit the case of nucleobase quadruplets, where the flexibility around H-bonds of two base pairs can be taken into account together with the intermolecular separation of the stacked pairs, whereas the planarity of the aromatic rings may be kept frozen during optimization.

CONCLUSIONS AND PERSPECTIVES

The aim of this work has been the validation and the development of some computational methods for the study of molecular interactions in soft matter, in particular in liquid crystals.

On one side, a novel approach for exploring the energy minima of the potential energy surface of large and flexible van der Waals dimers was tested on two benchmark molecules [167]. This method allows the geometry optimization of a dimer with respect to the total energy, which is the sum of the intra and intermolecular contributions. Its strong point is the cheap way the interaction energy is computed, while preserving a good accuracy. In fact, the optimization of large flexible dimers becomes rapidly unfeasible along with molecular dimensions as very expensive methods are required for an accurate evaluation of the interaction energy. Pivot of the optimization procedure is therefore the Fragmentation-Reconstruction Method (FRM) [25], thanks to which the expensive (sometimes unaffordable) calculation of the intermolecular energy is substituted by many computations on well smaller molecules.

On the other side, some strategies were investigated for the parameterization of force fields to be used in molecular dynamics simulations. In this context, a protocol developed in our group [25] was tested on a mesogenic molecule, namely 4,4'-diheptylazoxybenzene (HAB). In this parameterization the intra and intermolecular contributions to the force field were derived separately, in two main steps.

Firstly, the conformational and configurational spaces of the molecule monomer and dimer, respectively, were explored with suitable quantum mechanical (QM) methods. In particular,

the interaction energy of the dimer was computed within the FRM approach.

Secondly, parameterized model potentials E^{inter} and E^{intra} were fitted on the QM energies obtaining the parameters of the force field, equilibrium values and force constants of internal coordinates on one side and interaction parameters (q, σ, ϵ) on the other.

Different models of HAB were studied, varying the definition of the interacting sites (united atom or full atomistic approaches) and the form of the intermolecular potential (Lennard-Jones or Buckingham). Both approaches produced satisfactory results, succeeding in the correct prediction of HAB smectic behavior and providing estimates for various observable properties in good agreement with experimental data. However, the models seemed incapable of predicting the nematic behavior of HAB.

This fact led to a deeper analyses of the protocol weaknesses and two main limits emerged. The first can be found in the way the configurations for the QM database of energies were selected. With an *a priori* selection, in fact, a reference database which is not representative of bulk phases can be obtained, as some populated geometries might go neglected.

The second is that during the sampling the internal geometries of A and B monomers were kept frozen to their minimum. This limits severely the regions of the dimer configurational space that can be sampled and runs out the possibility of a simultaneous exploration of the monomer conformational one.

To overcome these limits the possibility of choosing the dimer geometries from an MD trajectory was considered. This approach allows for an iterative improvements of the intermolecular parameters and it is currently under study in our laboratory. A strategy for a systematic selection of dimer configurations has been coded in a Fortran program, named PICKY. Tests are being carried on to improve and validate the code performances first on simple case studies and then on more complex (flexible) large molecules.

At the same time, a strategy to reduce the redundancy of the sets of intermolecular parameters is being developed. This redundancy is a direct consequence of fitting the dimer PES on a limited number of points and the choice of a certain set among many others, even with very similar standard deviations, is pivotal for the success of a simulation. Unfortunately, the approach tested on HAB lacked of objective choosing criteria (apart from the standard deviation) and the parameter set had to be chosen, at least in minor part, according to the results of short MD runs. In this way, however, the *ab initio* nature of the force field was weakened. In this context, we plan to insert the fragment-fragment interaction energies, available thanks to the use of FRM, in the fitting procedure. These energies are expected

to give useful information on how contributions to the total interaction energy arise from the different molecular portions and they might succeed in guiding the model function E^{inter} towards more physically sound minima.

BIBLIOGRAPHY

[1] P. G. de Gennes, Soft Matter, Physics Reports **256**, 495 (1992).

[2] C. N. Likos, Effective interactions in soft condensed matter physics, Physics Reports **348**, 267 (2001).

[3] P. G. de Gennes, Soft matter: more than words, Soft Matter **1**, 16 (2005).

[4] M. Praprotnik, L. Delle Site, and K. Kremer, Multiscale Simulation of Soft Matter: From Scale Bridging to Adaptive Resolution, Annu. Rev. Phys. Chem. **59**, 545 (2008).

[5] M. R. Wilson, Computer simulations of soft self-organising molecular materials, Soft Matter **979**, 166 (2008).

[6] M. Wilson, Themed issue: modelling of soft matter, Soft Matter **5**, 4355 (2009).

[7] A. D. MacKerell, D. Bashford, M. Bellott, R. Dunbrack, J. D. Evanseck, M. J. Field, S. Fischer, J. Gao, H. Guo, S. Ha, D. Joseph-McCarthy, L. Kuchnir, K. Kuczera, F. T. K. Lau, C. Mattos, S. Michnick, T. Ngo, D. T. Nguyen, B. Prodhom, W. E. Reiher, B. Roux, M. Schlenkrich, J. C. Smith, R. Stote, J. Straub, M. Watanabe, J. Wiorkiewicz-Kuczera, D. Yin, and M. Karplus, All-atom empirical potential for molecular modeling and dynamics studies of proteins, J. Phys. Chem. B **102**, 3586 (1998).

[8] J. C. Phillips, R. Braun, W. Wang, J. Gumbart, E. Tajkhorshid, E. Villa, C. Chipot, R. D. Skeel, L. Kale, and K. Schulten, Scalable molecular dynamics with NAMD, J. Comp. Chem. **26**, 1781 (2005).

[9] J. M. Wang, R. M. Wolf, J. W. Caldwell, P. A. Kollman, and D. A. Case, Development and testing of a general amber force field, J. Comp. Chem. **25**, 1157 (2004).

[10] B. Hess, C. Kutzner, D. van der Spoel, and E. Lindahl, GROMACS 4: Algorithms for Highly Efficient, Load-Balanced, and Scalable Molecular Simulation, J. Chem. Theory Comput. **4**, 435 (2008).

[11] H. J. Limbach, A. Arnold, B. A. Mann, and C. Holm, ESPResSO-an extensible simulation package for research on soft matter systems, ChemPhysChem. **174**, 704 (2006).

[12] M. G. Guenza, Theoretical models for bridging timescales in polymer dynamics, J. Phys: Condens. Matter **20**, 033101 (2008).

[13] C. N. Likos, Soft Matter with soft particle, Soft Matter **2**, 478 (2006).

[14] M. R. Wilson, Molecular simulation of liquid crystals: progress towards a better understanding of bulk structure and the prediction of material properties, Chem. Soc. Rev. **36**, 1881 (2007).

[15] M. R. Wilson, Computer simulations of soft self-organising molecular materials, AIP Conference Proceedings **979**, 166 (2008).

[16] M. Karplus and A. McCammon, Molecular dynamics simulations of biomolecules, Nat. Struct. Mol. Biol. **9**, 646 (2002).

[17] M. Karplus and J. Kuriyan, Molecular dynamics and protein function, Proceedings of the National Academy of Sciences of the USA **102**, 6679 (2005).

[18] S. A. Adcock and J. A. McCammon, Molecular Dynamics: Survey of Methods for Simulating the Activity of Proteins, Chem. Rev. **106**, 1589 (2006).

[19] A. Redondo and R. LeSar, Modeling and Simulation of Biomaterials, Annu. Rev. Mater. Res. **34**, 279 (2004).

[20] J. Crain and A. V. Komolkin, Simulating molecular properties of liquid crystals, in *Advances in chemical physics*, volume 109, pages 39–113, JOHN WILEY & SONS INC, New York, 1999.

[21] K. Kremer, Simulation studies of soft matter: generic statistical properties and chemical details, Eur. Phys. J. B **64**, 525 (2008).

[22] W. G. Noid, J.-W. Chu, G. S. Ayton, V. Krishna, S. Izvekov, G. A. Voth, A. Das, and H. C. Andersen, The multicale coarse-graining method. I. A rigorous bridge between atomistic and coarse-grained models, J. Chem. Phys. **128**, 244114 (2008).

[23] T. Murtola, A. Bunker, I. Vattulainen, M. Deserno, and M. Karttunen, Multiscale modeling of emergent materials: biological and soft matter, Phys. Chem. Chem. Phys. **11**, 1869 (2009).

[24] C. Peter and K. Kremer, Multiscale simulation of soft matter systems, Faraday Discuss. **144**, 144 (2010).

[25] C. Amovilli, I. Cacelli, S. Campanile, and G. Prampolini, Calculation of the intermolecular energy of large molecules by a fragmentation scheme: Application to the 4-n-pentyl-4 '-cyanobiphenyl (5CB) dimer, J. Chem. Phys. **117**, 3003 (2002).

[26] P. G. de Gennes and J. Prost, *The Physics of Liquid Crystals*, Oxford University Press, New York, 1993.

[27] G. R. Luckhurst and G. W. Gray, *The Molecular Physics of Liquid Crystals*, Academic Press, New York, London, 1979.

[28] S. Kumar, *Liquid Crystals: experimental study of physical properties and phase transitions*, Cambridge Press University, Cambridge, 2001.

[29] P. Das, A. N. Biswas, A. Choudhury, P. Bandyopadhyay, H. Sripada, P. K. Mandal, and S. Upreti, Novel synthetic route to liquid crystalline 4,4 '-bis(n-alkoxy)azoxybenzenes: spectral characterisation, mesogenic behaviour and crystal structure of two new members, Liq. Cryst. **35**, 541 (2008).

[30] J. V. D. Veen, W. H. de Jeu, A. H. Grobben, and J. Boven, Low Melting Liquid Crystalline p,p'-di-n-Alkylazoxy- and Azobenzenes, Mol. Cry. Liq. Cry. **17**, 291 (1972).

[31] S. Sabol-Keast and M. E. Neubert, Improved Synthesis of Dialkylazoxybenzenes, Mol. Cry. Liq. Cry. **182**, 287 (1990).

[32] J. Van Der Veen, W. H. de Jeu, M. W. M. Wanninkhof, and C. A. M. Tienhoven, Transition Entropies and Mesomorphic Behavior of Para-Disubstituted Azoxybenzenes, J. Phys. Chem. **77**, 2153 (1973).

[33] E. F. Gramsbergen and W. H. de Jeu, First- ad Second-order Smectic-A to Nematic Phase Transitions in *p,p'*-Dialkylazoxybenzenes studied by Birefringence, J. Chem. Soc, Faraday Trans. 2 **88**, 1015 (1988).

[34] A. Primak, M. Fisch, and S. Kumar, Effect of mosaicity in x-ray studies of critical behavior at the nematic to smectic-*A* transition, Phys. Rev. E **66**, 51707 (2002).

[35] L. Chen, J. D. Brock, J. Huang, and S. Kumar, Critical Behavior at the Nematic-to-Smectic-*A* Transition in a Nonpolar Liquid Crystal with Wide Nematic Range, Phys. Rev. Lett. **67**, 2037 (1991).

[36] S. Y. Jeong, D. W. Kim, K. W. Rhie, M. P. Hong, S. Kumar, W. G. Jang, and S. T. Shin, Studies of critical behavior at the nematic to smectic A phase transition in C6 and C7 binary mixture system, J. Phys. D: Appl. Phys. **41**, 62002 (2008).

[37] E. A. L. Mol, G. C. L. Wong, J. M. Petit, F. Rieutord, and W. H. de Jeu, Thinning Transitions and fluctuations of freely suspended smectic-A films as studied by specular and diffuse X-ray scattering, Physica B **248**, 191 (1998).

[38] W. H. de Jeu, T. W. Lathouwers, and P. Bordewijk, Dielectric Properties of Di-it n-Heptyl Azoxybenzene in the Nematic and in the Smectic-*a* Phases, Phys. Rev. Lett. **32**, 40 (1974).

[39] W. H. de Jeu, W. J. A. Goossens, and P. Bordewijk, Influence of smectic order on the static dielectric permittivity of liquid crystals, J. Phys. Chem. **61**, 1985 (1974).

[40] J. P. Parneix and A. Chapoton, Dynamic Dielectric Anisotropy of Nematics with Respect to Molecular Structure, Mol. Cry. Liq. Cry. **78**, 115 (1981).

[41] L. Bata and A. Buka, Dielectric Permittivity and Relaxation Phenomena in Smectic Phases, Mol. Cry. Liq. Cry. **63**, 307 (1981).

[42] V. R. Murthy and R. N. V. R. Reddy, Polarizabilities and susceptibilities of nematic azoxybenzenes, J. Quant. Spectrosc. Radiat. Transfer. **25**, 183 (1981).

[43] P. Diehl, J. Jokisaari, F. Moia, and J. Lounila, The Smectic Phase of *p,p'*-di-*n*-heptylazoxybenzene: A ^{1}H NMR Study of Its Anisotropy of Diamagnetic Susceptibility and of Its Use for Measuring Proton Chemical Shift Anisotropies, Mol. Cry. Liq. Cry. **87**, 319 (1982).

[44] W. H. de Jeu and W. A. P. Claassen, The elastic constants of nematic liquid crystalline terminally substituted azoxybenzenes, J. Chem. Phys. **67**, 3705 (1977).

[45] J. W. van Dijk, W. W. Beens, and W. H. de Jeu, Viscoelastic properties of some nematic liquid crystalline azoxybenzene, J. Chem. Phys. **79**, 3888 (1983).

[46] V. Domenici, J. Czub, M. Geppi, B. Gestblom, S. Urban, and C.-A. Veracini, Dynamics of 4,4'-di-*n*-heptylazoxybenzene (HAB) studied using dielectric and ^{2}H NMR relaxation measurements, Liq. Cryst. **31**, 91 (2004).

[47] C. Forte, M. Geppi, and C. A. Veracini, Study of the Molecular Dynamics from Deuterium Zeeman and Quadrupolar NMR Relaxation of 4,4'-di-n-Heptylazoxybenzene in the Nematic and Smectic A Phases, Z. Naturforsch. A **49**, 311 (1994).

[48] W. Zajac, S. Urban, V. Domenici, M. Geppi, C.-A. Veracini, M. T. F. Telling, and B. J. Gabryś, Stochastic molecular motions in the nematic, smectic-*A*, and solid phases of *p,p'*-di-*n*-heptyl-azoxybenzene as seen by quasielastic neutron scattering and ^{13}C cross-polarization magic-angle-spinning NMR, Phys. Rev. E **73**, 51704 (2006).

[49] B. Jagadeesh, A. Prabhakar, M. H. V. R. Rao, C. V. S. Murty, V. G. K. M. Pisipati, A. C. Kunwar, and C. R. Bowers, Probing the Anisotropic Environment of Thermotropic Liquid Crystals Using ^{129}Xe NMR Spectroscopy, J. Phys. Chem. B **108**, 11272 (2004).

[50] E. H. Pape, On packing in smectics: X-ray diffraction study on the homologous series 4,4'-di-n-alkyl-azoxybenzenes, Mol. Cry. Liq. Cry. **102**, 271 (1984).

[51] E. H. Pape, Modulated structures in smectics: Longitudinal and transverse modulations in smectic a phases of terminally nonpolar molecules as shown by X-ray diffraction, Mol. Cry. Liq. Cry. **1**, 139 (1985).

[52] E. F. Gramsbergen and W. H. de Jeu, X-ray study of the sharpness of the smectic A layer structure, Liq. Cryst. **4**, 449 (1989).

[53] W. W. Beens and W. H. de Jeu, The flow alignment of some nematic liquid crystals, J. Chem. Phys. **82**, 3841 (1985).

[54] W. H. de Jeu and P. Bordewijk, Physical studies of nematic azoxybenzenes. II. Refractive indices and the internal field, J. Chem. Phys. **68**, 109 (1978).

[55] M. Giordano, D. Leporini, M. Martinelli, L. Pardi, C. A. Veracini, and C. Zannoni, Electron Resonance Investigation of a Cholesteric Meophase Induced by a Chiral Probe, J. Chem. Soc. Faraday Trans. 2 **78**, 307 (1982).

[56] N. Tomašovičova, M. Koneracká, P. Kopčanský, M. Timko, and V. Závišová, The Anchoring Energy of Liquid Crystal Molecules to Magnetic Particles in HAB-Based Ferronematics, Acta Physica Polonica A **113**, 591 (2008).

[57] J.-W. Park, J. Cho, and E. L. Thomas, Alignment and anchoring transition of liquid crystals on the surface of self-assembled block copolymers films with periodic defects, Soft Matter **4**, 739 (2008).

[58] M.-D. B. údez, G. Martínez-Nicolás, and F.-J. Carríon-Vilches, Tribological properties of liquid crystals as lubrificant additives, Wear **212**, 188 (1997).

[59] P. M. anc C. C. Huang, T. Stoebe, E. D. Wedell, T. Nguyen, W. H. de Jeu, F. Guittard, J. Naciri, R. Shashidhar, N. Clark, I. M. Jiang, F. J. Kao, H. Liu, and H. Nohira, Surface Tension Obtained from Various Smectic Free-Standing Films: The Molecular Origin of Surface Tension, Langmuir **14**, 4330 (1998).

[60] V. G. Nazarenko, O. P. Boiko, A. B. Nych, Y. A. Nastishin, V. M. Pergamenshchik, and P. Bos, Selective light-induced desorption: The mechanism of photoalignment of liquid crystals at adsorbing solid surfaces, Europhys. Lett. **75**, 448 (2006).

[61] M. Duchêne, J. W. Emsley, J. C. Lindon, J. Overstall, D. S. Stephenson, and S. R. Salman, The molecular structure and reorientation of parafluorobenzaldeyde dissolved in a smectic mesophase studied using NMR spectroscopy, Mol. Phys. **33**, 281 (1977).

[62] Y. Hiltunen, J. Jokisaari, Pulkkinen, and T. V*ää*n*ä*nen, An experimental ^{1}H NMR study of the structural deformation of benzene and the dipolar C-H splitting of methane in various nematic liquid crystals and in smectic HAB, Chem. Phys. Lett. **109**, 509 (1984).

[63] J. W. Emsley, G. R. Luckhurst, and G. N. Shilstone, The orientational Order of Solutions of a Dye Molecule in Liquid-Crystalline Solvents, J. Chem. Soc., Faraday Trans. 2 **83**, 371 (1987).

[64] M. Ghedini, I. Aiello, A. Crispini, A. Golemme, M. L. Deda, and D. Pucci, Azobenzenes and heteroaromatic nitrogen cyclopalladated complexes for advanced applications, Coord. Chem. Rev. **250**, 1373 (2006).

[65] M. P. Allen and M. R. Wilson, Computer simulation of liquid crystals, J. Computer Aided Mol. Design **3**, 335 (1989).

[66] M. Glaser, Atomistic simulation and modeling of smectic liquid crystals, in *ADVANCES IN THE COMPUTER SIMULATIONS OF LIQUID CRYSTALS*, edited by P. Pasini and C. Zannoni, volume 545 of *NATO ADVANCED SCIENCE INSTITUTES SERIES, SERIES C, MATHEMATICAL AND PHYSICAL SCIENCES*, pages 263–331, DORDRECHT, NETHERLANDS, 1999, SPRINGER, Conference of the NATO-Advanced-Study-Institute on Advances in the Computer Simulations of Liquid Crystals, ERICE, ITALY, JUN 11-21, 1998.

[67] C. M. Care and D. J. Cleaver, Computer simulation of liquid crystals, Rep. Prog. Phys. **68**, 2665 (2005).

[68] P. A. Lebwohl and G. Lasher, Nematic-Liquid-Crystal Order—A Monte Carlo Calculation, Phys. Rev. A **6**, 426 (1972).

[69] L. Onsager, The effects of shape on the interaction of colloidal particles, Ann. N.Y. Acad. Sci. **51**, 627 (1949).

[70] J. Vieillard-Baron, Phase Transitions of the Classical Hard-Ellipse System, J. Chem. Phys. **56**, 4729 (1972).

[71] D. Frenkel, B. M. Mulder, and J. P. McTague, Phase Diagram of a System of Hard Ellipsoids, Phys. Rev. Lett. **52**, 287 (1984).

[72] D. Frenkel and B. M. Mulder, The hard ellipsoid-of-revolution fluid I. Monte Carlo simulations, Mol. Phys. **55**, 1171 (1985).

[73] M. P. ALLEN, Computer-simulation of a biaxial liquid-crystal, Liq. Cryst. **8**, 499 (1990).

[74] P. J. Camp and M. P. Allen, Phase diagram of the hard biaxial ellipsoid fluid, J. Chem. Phys. **106**, 6681 (1997).

[75] J. Vieillard-Baron, The equation of state of a system of hard spherocylinders, Mol. Phys. **28**, 809 (1974).

[76] A. Stroobants, H. N. W. Lekkerkerker, and D. Frenkel, Evidence for Smectic Order in a Fluid of Hard Parallel Spherocylinders, Phys. Rev. Lett. **57**, 1452 (1986).

[77] J. A. C. Veerman and D. Frenkel, Phase diagram of a system of hard spherocylinders by computer simulation, Phys. Rev. A **41**, 3237 (1990).

[78] S. C. McGrother and D. C. Williamson and G. Jackson, A re-examination of the phase diagram of hard spherocylinders, J. Chem. Phys. **104**, 6755 (1996).

[79] P. Bolhuis and D. Frenkel, Tracing the phase boundaries of hard spherocylinders, J. Chem. Phys. **106**, 666 (1997).

[80] J. Gay and B. Berne, Modification of the overlap potential to mimic a linear site-site potential, J. Chem. Phys. **74**, 3316 (1981).

[81] R. Berardi, C. Fava, and C. Zannoni, A gay-berne potential for dissimilar biaxial particles, Chem. Phys. Lett. **297**, 8 (1998).

[82] D. J. Cleaver, C. M. Care, M. P. Allen, and M. P. Neal, Extension and generalization of the Gay-Berne potential, Phys. Rev. E **54**, 559 (1996).

[83] S. J. Picken, W. F. Vangunsteren, P. T. Vanduijnen, and W. H. Dejeu, A molecular-dynamics study of the nematic phase of 4-normal-pentyl-4'-cyanobiphenyl, Liq. Cryst. **6**, 357 (1989).

[84] C. McBride, M. R. Wilson, and J. A. K. Howard, Molecular dynamics simulations of liquid crystal phases using atomistic potentials, Mol. Phys. **95**, 121 (1998).

[85] Y. Lansac, M. A. Glaser, N. A. Clark, and O. D. Lavrentovich, Photocontrolled nanophase segregation in a liquid-crystal solvent, Nature **398**, 54 (1999).

[86] M. J. Cook and M. R. Wilson, The First Thousand-Molecule Simulation of a Mesogen at the Fully Atomistic Level, Mol. Cry. Liq. Cry. **363**, 181 (2001).

[87] R. Berardi, L. Muccioli, and C. Zannoni, Can nematic transitions be predicted by atomistic simulations? A computational study of the odd even effect, ChemPhysChem **5**, 104 (2004).

[88] J. Peláez and M. R. Wilson, Atomistic Simulations of a Thermotropic Biaxial Liquid Crystal, Phys. Rev. Lett. **97**, 267801 (2006).

[89] A. J. McDonald and S. Hanna, Atomistic simulation of a model liquid crystal, J. Phys. Chem. **124**, 164906 (2006).

[90] J. Pelaez and M. Wilson, Molecular orientational and dipolar correlation in the liquid crystal mixture E7: a molecular dynamics simulation study at a fully atomistic level, Phys. Chem. Chem. Phys **9**, 2968 (2007).

[91] I. Cacelli, G. Prampolini, and A. Tani, Liquid crystal properties of the n-alkyl-cyanobiphenyl series from atomistic simulations with Ab initio derived force fields, J. Phys. Chem. B **111**, 2130 (2007).

[92] I. Cacelli, C. F. Lami, and G. Prampolini, Force-Field Modeling through Quantum Mechanical Calculations: Molecular Dynamics Simulations of a Nematogenic Molecule in its Condensed Phases, J. Comp. Chem. **30**, 366 (2008).

[93] G. Tiberio, L. Muccioli, R. Berardi, and C. Zannoni, Toward *in Silico* Liquid Crystals. Realistic Transition Temperatures and Physical Properties for *n*-Cyano-biphenyls via Molecular Dynamics Simulations, ChemPhysChem **10**, 125 (2009).

[94] P. P. Ewald, The calculation of optical and electrostatic grid potential, Ann. Phys **369**, 253 (1921).

[95] R. Pecheanu and N. M. Cann, Molecular dynamics simulations of the liquid-crystal phases of 2-(4-butyloxyphenyl)-5-octyloxypyrimidine and 5-(4-butyloxyphenyl)-2-octyloxypyrimidine, Phys. Rev. E **81**, 041704 (2010).

[96] C. Peter, L. Delle Site, and K. Kremer, Classical simulations from the atomistic to the mesoscale and back: coarse graining an azobenzene liquid crystal, Soft Matter **4**, 859 (2008).

[97] I. Cacelli, A. Cimoli, L. D. Gaetani, G. Prampolini, and A. Tani, Chemical Detail Force Fields for Mesogenic Molecules, J. Chem. Theory Comput. **5**, 1865 (2009).

[98] M. W. van der Kamp, K. E. Shaw, C. J. Woods, and A. J. Mulholland, Biomolecular simulation and modelling: stauts, progress and proscpects, J. R. Soc. Interface **5**, S173 (2008).

[99] W. L. Jorgensen and J. Tiradorives, The opls potential functions for proteins - energy minimizations for crystals of cyclic-peptides and crambin, J. Am. Chem. Soc. **110**, 1657 (1988).

[100] G. Kaminski, E. M. Duffy, T. Matsui, and W. L. Jorgensen, Free Energies of Hydration and Pure Liquid Properties of Hydrocarbons from the OPLS All-Atom Model, J. Phys. Chem. **98**, 13077 (1994).

[101] W. L. Jorgensen, D. S. Maxwell, and J. Tirado-Rives, Development and Testing of the OPLS All-Atom Force-Field on Conformational Energetics and Properties of Organic Liquids, J. Am. Chem. Soc. **118**, 11225 (1996).

[102] G. A. Kaminski, R. A. Friesner, J. Tirado-Rives, and W. L. Jorgensen, Evaluation and reparametrization of the OPLS-AA force field for proteins via comparison with accurate quantum chemical calculations on peptides, J. Phys. Chem. **105**, 6474 (2001).

[103] S. J. Weiner, P. A. Kollman, D. A. Case, U. C. Singh, C. Ghio, G. Alagona, S. profeta, and P. Weiner, A new force-field for molecular mechanical simulation of nucleic-acids and proteins, J. Am. Chem. Soc. **106**, 765 (1984).

[104] D. A. Pearlman, D. A. Case, J. W. Caldwell, W. S. Ross, T. E. Cheatman, S. Debolt, D. Ferguson, G. Seibel, and P. Kollman, Amber, a package of computer-programs for applying molecular mechanics, normal-mode analysis, molecular-dynamics and free-energy calculations to simulate the structural and energetic properties of molecules, Computer Physics Communications **91**, 1 (1995).

[105] B. R. Brooks, R. E. Bruccoleri, B. D. Olafson, D. J. States, S. Swaminathan, and M. Karplus, Charmm - a program for macromolecular energy, minimization, and dynamics calculations, J. Comp. Chem. **4**, 187 (1983).

[106] A. D. Mackerell, Empirical force fields for biological macromolecules: Overview and issues, J. Comp. Chem. **25**, 1584 (2004).

[107] Y.-P. Liu, K. Kim, B. J. Berne, R. A. Friesner, and S. W. Rick, Constructing *ab initio* force fields for molecular dynamics simulations, J. Chem. Phys. **108**, 4739 (1998).

[108] G. A. Kaminski, H. A. Stern, B. J. Berne, and R. A. Friesner, Development of an Accurate and Robust Polarizable Molecular Mechanics Force Field from ab Initio Quantum Chemistry, J. Phys. Chem. **108**, 621 (2004).

[109] M. Masia, *Ab Initio* based polarizable force field parameterization, J. Chem. Phys. **128**, 184107 (2008).

[110] P. Maurer, A. Laio, H. W. Hugosson, M. C. Colombo, and U. Rothlisberger, Automated Parameterization of Biomolecular Force Fields from Quantum Mechanics/Molecular Mechanics (QM/MM) Simulations through Force Matching, J. Chem. Theory Comput. **3**, 628 (2007).

[111] O. Akin-Ojo, Y. Song, and F. Wang, Developing *ab initio* quality force fields from condensed phase quantum-mechanics/molecular -mechanics calculations through the adaptive force matching method, J. Chem. Phys. **129**, 64108 (2008).

[112] M. P. Allen and D. J. Tildesley, *Computer Simulation of Liquids*, Clarendon, Oxford, 1987.

[113] L. Wang and R. Sadus, Relationships between three-body and two-body interactions in fluids and solids, J. Chem. Phys. **125**, 074503 (2006).

[114] I. Cacelli, G. Cinacchi, G. Prampolini, and A. Tani, Computer simulation of solid and liquid benzene with an atomistic interaction potential derived from ab initio calculations , J. Am. Chem. Soc. **126**, 14278 (2004).

[115] W. L. Jorgensen and D. L. Severance, Aromatic aromatic interactions - free-energy profiles for the benzene dimer in water, chloroform, and liquid benzene, J. Am. Chem. Soc. **112**, 4768 (1990).

[116] I. Cacelli and G. Prampolini, Parametrization and validation of intramolecular force fields derived from DFT calculations , J. Chem. Theory Comput. **3**, 1803 (2007).

[117] A. D. Becke, Density-functional thermochemistry .3. The role of exact exchange, J. Chem. Phys. **98**, 5648 (1993).

[118] S. Dasgupta, T. Yamasaki, and W. A. Goddard, The Hessian biased singular value decomposition method for optimization and analysis of force fields, J. Chem. Phys. **104**, 2898 (1996).

[119] M. J. Frisch, G. W. Trucks, H. B. Schlegel, G. E. Scuseria, M. A. Robb, J. R. Cheeseman, J. A. Montgomery, Jr., T. Vreven, K. N. Kudin, J. C. Burant, J. M. Millam, S. S. Iyengar, J. Tomasi, V. Barone, B. Mennucci, M. Cossi, G. Scalmani, N. Rega, G. A. Petersson, H. Nakatsuji, M. Hada, M. Ehara, K. Toyota, R. Fukuda, J. Hasegawa, M. Ishida, T. Nakajima, Y. Honda, O. Kitao, H. Nakai, M. Klene, X. Li, J. E. Knox, H. P. Hratchian, J. B. Cross, V. Bakken, C. Adamo, J. Jaramillo, R. Gomperts, R. E. Stratmann, O. Yazyev, A. J. Austin, R. Cammi, C. Pomelli, J. W. Ochterski, P. Y. Ayala, K. Morokuma, G. A. Voth, P. Salvador, J. J. Dannenberg, V. G. Zakrzewski, S. Dapprich, A. D. Daniels, M. C. Strain, O. Farkas, D. K. Malick, A. D. Rabuck, K. Raghavachari, J. B. Foresman, J. V. Ortiz, Q. Cui, A. G. Baboul, S. Clifford, J. Cioslowski, B. B. Stefanov, G. Liu, A. Liashenko, P. Piskorz, I. Komaromi, R. L. Martin, D. J. Fox, T. Keith, M. A. Al-Laham, C. Y. Peng, A. Nanayakkara, M. Challacombe, P. M. W. Gill, B. Johnson, W. Chen, M. W. Wong, C. Gonzalez, J. A. Pople, and Gaussian 03, Revision C.02, Gaussian, Inc., Wallingford, CT, 2004.

[120] G. Cinacchi and G. Prampolini, DFT study of the torsional potential in ethylbenzene and ethoxybenzene: The smallest prototypes of alkyl- and alkoxy-aryl mesogens, J. Phys. Chem. A **107**, 5228 (2003).

[121] I. Cacelli, G. Prampolini, and A. Tani, Atomistic simulation of a nematogen using a force field derived from quantum chemical calculations, J. Phys. Chem. B **109**, 3531 (2005).

[122] S. Tsuzuki, K. Honda, T. Uchimaru, M. Mikami, and K. Tanabe, The magnitude of the CH/pi interaction between benzene and some model hydrocarbons, J. Am. Chem. Soc. **122**, 3746 (2000).

[123] C. Amovilli, I. Cacelli, G. Cinacchi, L. D. Gaetani, G. Prampolini, and A. Tani, Structure and dynamics of mesogens using intermolecular potential derived from *ab initio* calculations, Theor. Chim. Accounts **117**, 885 (2007).

[124] D. W. Zhang and J. Z. H. Zhang, Molecular fractionation with conjugate caps for full quantum mechanical calculation of proteinmolecule interaction energy, J. Chem. Phys. **119**, 3599 (2003).

[125] Y. Xiang, D. W. Zhang, and J. Z. H. Zhang, Fully quantum mechanical energy optimization or protein-ligand structure, J. Comp. Chem. **25**, 1431 (2004).

[126] S. Li and T. Fang, An Efficient Fragment-Based Approach for Predicting the Ground-State Energies and Structures of Large Molecules, J. Am. Chem. Soc. **127**, 7215 (2005).

[127] V. Ganesh, R. Dongare, P. Balarayan, and S. Gadre, Molecular tailoring approach for geometry optimization of large molecules: Energy evaluation and parallelization strategies, J. Chem. Phys. **125**, 104109 (2006).

[128] D. Fedorov and K. Kitaura, editors, *The Fragment Molecular Orbital Method: Pratical Applications to Large Molecular Systems*, CRC press, Boca Raton, FL, 2009.

[129] D. Fedorov, T. Ishida, and K. Kitaura, The fragment molecular orbital method for geometry optimizations of polypeptides and proteins, J. Phys. Chem. A **111**, 2722 (2007).

[130] E. Dahlke and D. Truhlar, Electrostatically embedded many-body expansion for large systems, with applications to water clusters, J. Chem. Theory Comput. **3**, 46 (2007).

[131] M. Bizzarri, I. Cacelli, G. Prampolini, and A. Tani, Intermolecular Force Fields of Large Molecules by the Fragmentation Reconstruction Method (FRM): Application to a Nematic Liquid Crystal, J. Phys. Chem. A **108**, 10336 (2004).

[132] A. Cimoli, *Diagramma di fase e proprietà dinamiche di un modello di 4,4'-dieptilazoxybenzene (HAB) con simulazioni atomistiche da potenziali ab initio* Tesi di Laurea, Dipartimento di chimica, Università degli studi di Pisa, Pisa, a.a. 2006/2007.

[133] M. E. Rose, *Elementary theory of angular momentum*, Wiley, New York, 1957.

[134] S. F. Boys and F. Bernardi, Calculation of small molecular interactions by differences of separate total energies - some procedures with reduced errors, Mol. Phys. **19**, 553 (1970).

[135] P. Hobza, H. L. Selzle, and E. W. Schlag, Potential energy surface for the benzene dimer. Results of ab initio CCSD(T) calculations show two nearly isoenergetic structures: T-shaped and parallel-displaced, J. Phys. Chem. **100**, 18790 (1996).

[136] P. Hobza, R. Zahradník, and K. Müller-Dethlefs, The world of non-covalent interactions: 2006, Collect. Czech. Chem. Comm. **71**, 443 (2006).

[137] S. Tsuzuki, K. Honda, T. Uchimaru, M. Mikami, and K. Tanabe, Origin of attraction and directionality of the x/x interaction: Model chemistry calculations of benzene dimer interaction, J. Am. Chem. Soc. **124**, 104 (2002).

[138] M. O. Sinnokrot and C. D. Sherrill, High-accuracy quantum mechanical studies of pi-pi interactions in benzene dimers, J. Phys. Chem. A **110**, 10656 (2006).

[139] I. Cacelli, G. Cinacchi, C. Geloni, G. Prampolini, and A. Tani, Computer simulation of p-phenyls with interaction potentials from ab-initio calculations, Mol. Cry. Liq. Cry. **395**, 171 (2003).

[140] I. Cacelli, G. Prampolini, and A. Tani, Modeling a liquid crystal dynamics by atomistic simulation with an ab initio derived force field, J. Phys. Chem. B **110**, 2847 (2006).

[141] W. Jorgensen, E. Laird, T. Nguyen, and J. Tirado-Rives, Monte-carlo simulations of pure liquid substituted benzenes with opls potential functions, J. Comp. Chem. **14**, 206 (1993).

[142] D. Paschen and A. Geiger, *MOSCITO 3.9*, Department of Physical Chemistry, University of Dortmund, 2000.

[143] J. P. Ryckaert, G. Ciccotti, and H. J. C. Berendsen, Numerical-integration of cartesian equations of motion of a system with constraints - molecular-dynamics of n-alkanes, J. Comput. Phys. **55**, 3336 (1977).

[144] T. A. Darden, D. York, and L. Pedersen, Particle mesh ewald - an n.log(n) method for ewald sums in large systems, J. Chem. Phys. **98**, 10089 (1993).

[145] U. Essmann, L. Perera, M. L. Berkowitz, A. Darden, H. Lee, and L. Pedersen, A smooth particle mesh ewald method, J. Chem. Phys. **103**, 8577 (1995).

[146] H. J. C. Berendsen, J. P. M. Postma, W. F. van Gusteren, A. Di Nola, and J. R. Haak, Molecular-dynamics with coupling to an external bath, J. Chem. Phys. **81**, 3684 (1984).

[147] M. A. Bates and G. R. Luckhurst, Computer simulation studies of anisotropic systems. XXX. The phase behavior and structure of a Gay-Berne mesogen, J. Chem. Phys. **110**, 7087 (1999).

[148] J. P. Hansen and I. R. McDonald, *Theory of Simple liquids*, Academic press, New York, 1986.

[149] M. Cifelli, L. De Gaetani, G. Prampolini, and A. Tani, Atomistic computer simulation and experimental study on the dynamics of the n-cyanobiphenyls mesogenic series , J. Phys. Chem. B **112**, 9777 (2008).

[150] M. Bõckmann, C. Peter, L. Delle Site, N. Doltsinis, K. Kremer, and D. Marx, Atomistic force field for azobenzene compounds adapted for QM/MM simulations with applications to liquids and liquid crystals, J. Chem. Theory Comput. **3**, 1789 (2007).

[151] M. Cifelli, G. Cinacchi, and L. De Gaetani, Smectic order parameters from diffusion data, J. Chem. Phys. **125**, 164912 (2006).

[152] W. Götze and L. Sjögren, Relaxation processes n supercooled liquids, Rep. Prog. Phys. **55**, 241 (1992).

[153] L. De Gaetani, G. Prampolini, and A. Tani, Subdiffusive dynamics of a liquid crystal in the isotropic phase, J. Chem. Phys. **128**, 194501 (2008).

[154] L. D. Gaetani and G. Prampolini, Computational stury through atomistic potentials of a partial bilayer liquid crystal: structure and dynamics, Soft Matter **5**, 3517 (2009).

[155] P. L. Cristinziano and F. Lelj, Atomistic simulation of discotic liquid crystals: Transition from isotropic to columnare phase example, J. Chem. Phys. **127**, 34506 (2007).

[156] S. Nosé, A unified formulation of the constant temperature molecular dynamics methods, J. Chem. Phys. **81**, 511 (1984).

[157] W. G. Hoover, Canonical dynamics: Equilibrium phase-space distributions, Phys. Rev. A **31**, 1695 (1985).

[158] M. Parrinello and A. Rahman, Polymorphic transitions in single crystals: A new molecular dynamics method, J. Appl. Phys. **52**, 7182 (1981).

[159] R. A. Buckingham, The Classical Equation of State of Gaseous Helium, Neon and Argon, Proc. R. Soc. Lond. A **168**, 264 (1938).

[160] F. Ercolessi and J. B. Adams, Interatomic Potentials from First-Principles Calculations: the Force-Matching Method, Europhys. Lett. **26**, 583 (1994).

[161] A. Laio, S. Bernard, G. L. Chiarotti, S. Scandolo, and E. Tosatti, Physics of iron at Earth's core conditions, Science **287**, 1027 (2000).

[162] S. Izvekov, M. Parrinello, C. J. Burnham, and G. A. V. G. A., Effective force fields for condensed phase systems from ab initio molecular dynamics simulation: A new method for force-matching, J. Chem. Phys. **120**, 10896 (2004).

[163] P. Maurer, A. Laio, H. W. Hugosson, M. C. Colombo, and U. Rothlisberger, Automated Parametrization of Biomolecular Force Fields from Quantum Mechanics/Molecular Mechanics (Qm/MM) Simulations through Force Matching, J. Chem. Theory Comput. **3**, 628 (2007).

[164] P. Brommer and F. Gahler, Potfit: effective potentials from ab initio data, Modelling Simul. Mater. Sci. Eng. **15**, 295 (2007).

[165] B. Waldher, J. Kuta, S. Chen, N. Henson, and A. E. Clark, ForceFit: A Code to Fit Classical Force Fields to Quantum Mechanical Potential Energy Surfaces, J. Comp. Chem. **31**, 2307 (2010).

[166] M. Fioroni and D. Vogt, Toluene Model for Molecular Dynamics Simulations in the Ranges 298 ¡ T (K) ¡ 350 and 0.1 ¡ P (MPa) ¡ 10, J. Phys. Chem. B **108**, 11774 (2004).

[167] I. Cacelli, A. Cimoli, and G. Prampolini, Geometry Optimization of Large and Flexible van der Waals Dimers: A Fragmentation-Reconstruction Approach, J. Chem. Theory Comput. **6**, 2536 (2010).

[168] H. Margenau and N. R. Kestner, *Theory of Intermolecular Forces*, Pergamon Press, Branswheig, 1969.

[169] A. J. Stone, *The Theory of Intermolecular Forces*, Oxford University Press, Oxford, 1996.

[170] I. G. Kaplan, *The Interatomic Potential Concept and Classification of Interactions* in Handbook of Molecular Physics and Quantum Chemistry, edited by S. Wilson, P.F. Bernath and R. McWeeny, Wiley, Chichester, West Sussex, England, 2003.

[171] J. Israelachvili, *Intermolecular and Surface Forces. Third Edition*, Academic Press, London, 2010.

[172] V. A. Parsegian, *Van der Waals Forces: A Handbook for Biologists, Chemists, Engineers, and Physicists*, Cambridge University Press, Cambridge, 2005.

[173] M. Kleman and O. Laverntovich, *Soft Matter Physics An Introduction*, Springer, Berlin, 2003.

[174] I. Hamley, *Introduction to Soft Matter: Synthetic and Biological Self-Assembling Materials, Revised Edition*, Wiley, Chichester, West Sussex, England, 2007.

[175] P. J. Collings and M. Hird, *Introduction to Liquid Crystals*, Adam Hilger, Bristol, 1997.

[176] D. Demus, J. Goodby, G. W. Gray, H. W. Spiess, and V. Vill, editors, *Handbook of Liquid Crystals (Vol. 1: Fundamentals)*, Wiley-VCH, Weinheim, 1998.

[177] G. B. McGaughey, M. Gagné, and A. Rappé, pi-stacking interactions - Alive and well in proteins, J. Biol. Chem. **273**, 15458 (1998).

[178] P. Hobza and J. Sponer, Toward true DNA base-stacking energies: MP2, CCSD(T), and complete basis set calculations, J. Am. Chem. Soc. **124**, 11802 (2002).

[179] J. Sponer, K. Riley, and P. Hobza, Nature and magnitude of aromatic stacking of nucleic acid bases, Phys. Chem. Chem. Phys. **10**, 2595 (2008).

[180] E. A. Meyer, R. K. Castellano, and F. Diederich, Interactions with aromatic rings in chemical and biological recognition, Angew. Chem. Int. Ed. **42**, 1210 (2003).

[181] R. Bushby and O. Lozman, Discotic liquid crystals 25 years on, Current Opinion in Colloid & Interface Science **7**, 343 (2002).

[182] S.Laschat, A. Baro, N. Steinke, F. Giesselmann, C. Hagele, G. Scalia, R. Judele, E. Kapatsina, S. Sauer, A. Schreivogel, and M. Tosoni, Discotic liquid crystals: From tailor-made synthesis to plastic electronics, Angew. Chem. Int. Ed. **46**, 4832 (2007).

[183] A. M. van de Craats, J. M. Warman, K. Müllen, Y. Geerts, and J. D. Brand, Rapid charge transport along self-assembling graphitic nanowires, Adv. Mater. **10**, 36 (1998).

[184] P. Ehrenfreund, S. Rasmussen, J. Cleavesand, and L. Chen, Experimentally tracing the key steps in the origin of life: The aromatic world, Astrobiology **6**, 490 (2006).

[185] I. Cacelli and G. Prampolini, Torsional barriers and correlations between dihedrals in p-polyphenyls, J. Phys. Chem. A **107**, 8665 (2003).

[186] H. Valdes, K. Pluháčková, M. Pitoňák, J. Řezáč, and P. Hobza, Benchmark database on isolated small peptides containing an aromatic side chain: comparison between wave function and density functional theory methods and empirical force field, Phys. Chem. Chem. Phys. **10**, 2747 (2008).

[187] C. D. Sherrill, B. Sumpter, M. O. Sinnokrot, M. Marshall, E. Hohenstein, R. Walker, and I. Gould, Assessment of Standard Force Field Models Against High-Quality Ab Initio Potential Curves for Prototypes of pi-pi, CH/pi, and SH/pi Interactions, J. Comp. Chem. **30**, 2187 (2009).

[188] S. Tsuzuki, T. Uchimaru, K. Matsamura, M. Mikami, and K. Tanabe, Effects of the higher electron correlation correction on the calculated intermolecular interaction energies of benzene and naphthalene dimers: comparison between MP2 and CCSD(T) calculations, Chem. Phys. Lett. **319**, 547 (2000).

[189] K. Riley, M. Pitoňák, J. Černý, and P. Hobza, On the Structure and Geometry of Biomolecular Binding Motifs (Hydrogen-Bonding, Stacking, X-H$\cdots\pi$): WFT and DFT Calculations, J. Chem. Theory Comput. **6**, 66 (2010).

[190] M. O. Sinnokrot, E. F. Valeev, and C. D. Sherrill, Estimates of the ab initio limit for pi-pi interactions: The benzene dimer, J. Am. Chem. Soc. **124**, 10887 (2002).

[191] M. O. Sinnokrot and C. D. Sherrill, Highly accurate coupled cluster potential energy curves the benzene dimer: Sandwich, T-shaped, and parallel-displaced configurations, J. Phys. Chem. A **108**, 10200 (2004).

[192] S. Arnstein and C. D. Sherrill, Substituent effects in parallel-displaced pi-pi interactions, Phys. Chem. Chem. Phys. **10**, 2646 (2008).

[193] C. D. Sherrill, T. Takatani, and E. Hohenstein, An Assessment of Theoretical Methods for Nonbonded Interactions: Comparison to Complete Basis Set Limit Coupled-Cluster Potential Energy Curves for the Benzene Dimer, the Methane Dimer, Benzene-Methane, and Benzene-H2S, J. Phys. Chem. A **113**, 10146 (2009).

[194] A. Vasquez-Mayagoitia, C. D. Sherrill, T. Aprà, and B. G. Sumpter, An Assessment of Density Functional Methods for Potential Energy Curves of Nonbonded Interactions: The XYG3 and B97-D Approximations, J. Chem. Theory Comput. **6**, 727 (2010).

[195] E. J. Meijer and M. Sprik, A density-functional study of the intermolecular interactions of benzene, J. Chem. Phys. **105**, 8684 (1996).

[196] S. Tsuzuki and H. P. Lüthi, Interaction energies of van der Waals and hydrogen bonded systems calculated using density functional theory: Assessing the PW91 model, J. Chem. Phys. **114**, 3949 (2001).

[197] Y. Zhao and D. Truhlar, Density functionals for noncovalent interaction energies of biological importance, J. Chem. Theory Comput. **3**, 289 (2007).

[198] Y. Zhao and D. Truhlar, A new local density functional for main-group thermochemistry, transition metal bonding, thermochemical kinetics, and noncovalent interactions, J. Chem. Phys. **125**, 194101 (2006).

[199] Y. Zhao and D. Truhlar, The M06 suite of density functionals for main group thermochemistry, thermochemical kinetics, noncovalent interactions, excited states, and transition elements: two new functionals and systematic testing of four M06-class functionals and 12 other functionals, Theor. Chim. Accounts **120**, 215 (2008).

[200] E. Honenstein, S. Chill, and C. Sherrill, Assessment of the Performance of the M05-2X and M06-2X Exchange-Correlation Functionals for Noncovalent Interactions in Biomolecules, J. Chem. Theory Comput. **4**, 1996 (2008).

[201] S. Grimme, Accurate description of van der Waals complexes by density functional theory including empirical corrections, J. Comp. Chem. **25**, 1463 (2004).

[202] S. Grimme, Semiempirical GGA-type density functional constructed with a long-range dispersion correction, J. Comp. Chem. **27**, 1787 (2006).

[203] A. Hesselmann, G. Jansen, and M. Schutz, Density-functional theory-symmetry-adapted intermolecular perturbation theory with density fitting: A new efficient method to study intermolecular interaction energies, J. Chem. Phys. **122**, 014103 (2005).

[204] R. Podeszwa, R. Bukowski, and K. Szalewicz, Potential energy surface for the benzene dimer and perturbational analysis of pi-pi interactions, J. Phys. Chem. A **110**, 10345 (2006).

[205] R. L. Jaffe and G. D. Smith, A quantum chemistry study of benzene dimer, J. Chem. Phys. **105**, 2780 (1996).

[206] P. Hobza, H. L. Selzle, and E. W. Schlag, Potential energy surface for the benzene dimer. Results of ab initio CCSD(T) calculations show two nearly isoenergetic structures: T-shaped and parallel-displaced, J. Phys. Chem. **100**, 18790 (1996).

[207] M. Pitoňák, P. Neogrády, J. Černý, S. Grimme, and P. Hobza, Scaled MP3 Non-Covalent Interaction Energies Agree Closely with Accurate CCSD(T) Benchmark Data, ChemPhysChem. **10**, 282 (2009).

[208] S. Grimme, Improved second-order Moller-Plesset perturbation theory by separate scaling of parallel- and antiparallel-spin pair correlation energies, J. Chem. Phys. **118**, 9095 (2003).

[209] M. Pitoňák and A. Heßelmann, Accurate Intermolecular Interaction Energies from a Combination of MP2 and TDDFT Response Theory, J. Chem. Theory Comput. **6**, 168 (2010).

[210] J. Špóner, J. Leszczynski, and P. Hobza, Nature of nucleic acid-base stacking: Nonempirical ab initio and empirical potential characterization of 10 stacked base dimers. Comparison of stacked and H-bonded base pairs, J. Phys. Chem. **100**, 5590 (1996).

[211] K. Riley and P. Hobza, Assessment of the MP2 method, along with several basis sets, for the computation of interaction energies of biologically relevant hydrogen bonded and dispersion bound complexes, J. Phys. Chem. A **111**, 8257 (2007).

[212] L. Rutledge, H. Durst, and S. Wetmore, Evidence for Stabilization of DNA/RNA-Protein Complexes Arising from Nucleobase-Amino Acid Stacking and T-Shaped Interactions, J. Chem. Theory Comput. **5**, 1400 (2009).

[213] J. Fuhrmann, A. Rurainski, H.-P. Lenhof, and D. Neumann, A New Method for the Gradient-Based Optimization of Molecular Complexes, J. Comp. Chem. **30**, 1371 (2009).

LIST OF FIGURES

LIST OF TABLES